Influence of the North Atlantic Subtropical High on Summer Precipitation Over the Southeastern United States

by

Laifang Li

Earth and Ocean Sciences
Duke University

Date:_____

Approved:

_____
Wenhong Li, Supervisor

_____
M. Susan Lozier

_____
Paul A. Baker

_____
Ana P. Barros

_____
Yochanan Kushnir

Dissertation submitted in partial fulfillment of
the requirements for the degree of Doctor
of Philosophy in the
Earth and Ocean Sciences in the Graduate School
of Duke University

2014

ABSTRACT

Influence of the North Atlantic Subtropical High on Summer Precipitation Over the Southeastern United States

by

Laifang Li

Earth and Ocean Sciences
Duke University

Date:_____

Approved:

_____
Wenhong Li, Supervisor

_____
M. Susan Lozier

_____
Paul A. Baker

_____
Ana P. Barros

_____
Yochanan Kushnir

An abstract of a dissertation submitted in partial fulfillment of the requirements for the degree of Doctor of Philosophy in the Earth and Ocean Sciences in the Graduate School of Duke University

2014

Abstract

The Southeastern United States (SE US) is one of the fastest developing regions of the nation, where summer precipitation becomes increasingly important to sustain population and economic growth. In recent decades, the variability of SE US summer precipitation has significantly intensified, leading to more frequent and severe climate extremes. However, the processes that have caused such enhanced climate variability have been poorly understood. By analyzing atmospheric hydrological cycle, diagnosing atmospheric circulation dynamics, and performing regional climate simulations, this dissertation investigates the mechanisms responsible for SE US summer precipitation variability.

Analysis of regional moisture budget indicates that the variability of SE US summer precipitation is primarily controlled by moisture transport processes associated with the variation of the North Atlantic Subtropical High (NASH) western ridge, while local water recycling is secondary. As the ridge moves northwestward (NW) into the US continent, moisture transport pathway is away from the SE US and the upward motion is depressed. Thus, rainfall decreases over the SE US, leading to dry summers. In contrast, when the ridge moves southwestward (SW), moisture convergence tends to be enhanced over the SE US, facilitating heavier rainfall and causing wetter summers. However, as the ridge is located relatively eastward, its influence on the summer precipitation is weakened. The intensified precipitation variability in recent decades is

attributed to the more frequent occurrence of NW- and SW-type ridges, according to the "NASH western ridge – SE US summer precipitation" relationship.

In addition, the "NASH western ridge – SE US summer precipitation" relationship acts as a primary mechanism to determine general circulation model (GCM) and regional climate model (RCM) skill in simulating SE US summer precipitation. Generally, the state-of-the-art GCMs that are capable of representing the abovementioned relationship perform better in simulating the variability of SE US summer precipitation. Similarly, the RCM simulated summer precipitation bias over the SE US is largely caused by the errors in the NASH western ridge circulation, with the physical parameterization playing a secondary role.

Furthermore, the relationship between the NASH western ridge and SE US summer precipitation well explains the projected future precipitation changes. According to the projection by the ensemble of phase-5 of Coupled Model Intercomparison Project (CMIP5) models, summer precipitation over the SE US will become more variable in a warming climate. The enhancement of precipitation variability is due mainly to the atmospheric circulation dynamics, resulting from the pattern shift of the NASH western ridge circulation. In a warming climate, the NASH circulation tends to intensify, which forces its western ridge to extend further westward, exerting stronger impact on the SE US summertime climate. As the ridge extends westward, the NW- and SW-type ridges

occur more frequently, resulting in an increased occurrence of extreme summers over the SE US.

In summary, the studies presented in this dissertation identify the NASH western ridge as a primary regulator of SE US summer precipitation at seasonal scale. The "NASH western ridge – SE US summer precipitation" relationship established in this study serves as a first order mechanism for understanding and simulating processes that influence the statistics of extreme events over the SE in the current and future climate.

Table of Contents

List of Tables

List of Figures

Acknowledgements

I would like to extend my deepest gratitude to my advisor, Dr. Wenhong Li, for her excellent guidance on my PhD study. I thank Dr. Li for her time and effort, patience, and for her high expectations of my research. I was motived by Dr. Li's passion for science and inspired by her research methodology. My work with Dr. Li has caused me understand the value of a dream and hard work, as well as the determination to make the impossible possible.

Thanks also to my PhD dissertation committee: Drs. Susan Lozier, Paul Baker, Ana Barros, and Yochanan Kushnir. Their insightful comments and constructive criticism have greatly improved the science and presentation of this dissertation.

Thanks to Dr. Jiming Jin, for providing computational resources and for our active discussions on scientific questions. Without his generous help, the regional climate modeling study presented in this study would have been impossible.

I thank my lab mate, Mr. Patrick Brown, who always offers genius ideas to interpret the fundamentals governing the climate system. Discussions with him inspired my thinking and brought great enjoyment to my research.

Thanks to the EOS faculty, staff, and graduate students, who generously provided assistance with my PhD study. My special thanks extend to Dr. Nicolas Cassar, for offering advice on my career development.

My thanks also go to my master degree advisors in Chinese Academy and Sciences, Drs. Yimin Liu and Guoxiong Wu, for their training during the beginning stages of my research career. Their scientific attitude influenced me deeply. They encouraged me to explore the physical mechanisms behind climate phenomena. From them, I understood the spirit of science: “search and search again, that is why we call it research”.

Thanks to Dr. Ruixin Huang at WHOI, for his selfless help with my research and schoolwork. His profound physical interpretation and mathematical formulation helped me understand the fundamentals of climate sciences, which positively contributed to my research.

I thank my husband and my parents for their unconditional love. I also thank my American mom and dad, Diane and Don Bryson, for teaching me Academic writing and American culture, teaching me the meaning of “the American Dream”, and sharing with me their American love.

This study is supported by the research funding from NSF-AGS-1147608 and NIH-1R21AG044294-01A1.

1. Introduction

The Southeastern United States (SE US), namely 7 states that include North Carolina, South Carolina, Georgia, Florida, Alabama, Tennessee and Mississippi, is one of the fastest-developing regions in the nation. The growing population and economy has placed unprecedented demands and pressure on water resources, making warm-season precipitation increasingly important for this region (Manuel 2008; Martinez *et al.* 2009; Riha *et al.* 1996). However, in recent decades, warm-season precipitation has become extreme, characterized by alternations between long dry spells or intense rainfall and flooding (Douglas and Barros 2002), which devastates the local economy and agriculture. The enhanced precipitation extremes have been tied to the increased seasonal precipitation variability (Katz and Brown 1992; Li *et al.* 2011; Wang *et al.* 2010). Understanding the causes for the intensification of summer precipitation variability is therefore particularly important for this region.

The generation of SE US summer precipitation involves complicated interactions between systems at multiple spatiotemporal scales, which are especially sensitive to climate variability and climate change (Mearns *et al.* 2003). To date, the mechanisms controlling SE US summer precipitation are poorly understood, which hampers climate prediction in this fast developing region. This dissertation fills the gap by advancing the understanding of the mechanisms responsible for SE US summer precipitation variability and projecting future changes at a process-level.

1.1 Summer rainfall generation processes over the SE US

In the summer (June-July-August), precipitation over the Conterminous US shows an "east-west" gradient, with high precipitation occurring mainly over the SE US, especially over the coastal regions where summer precipitation climatology reaches 6 mm day^{-1} (Figure 1.1a). Averaged over the SE US domain, summer precipitation climatology is 4.3 mm day^{-1}. Furthermore, the SE US is also a region where summer precipitation shows the highest variability at interannual scale (standard deviation of summer precipitation ~ 1.0 mm day^{-1}; Figure 1.1b). Thus, the summer precipitation over the SE US significantly governs the rainfall variability of the whole country (Wang *et al.* 2010).

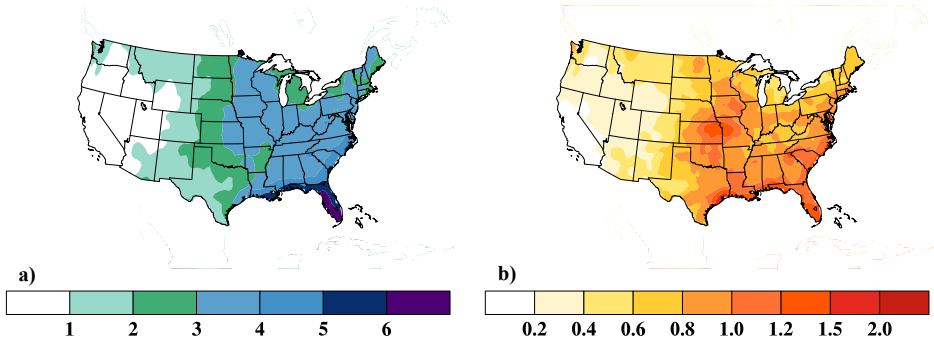

Figure 1.1: summer (June-July-August) precipitation (shaded, unit: mm day^{-1}) over the Conterminous US: a) 1948-2007 climatology and b) standard deviation of precipitation.

During summer months, the dominant air masses that influence the SE US climate are the maritime tropical air masses, originating from the Gulf of Mexico and the tropical Atlantic Ocean (Drumond *et al.* 2011; Soulé 1998). These air masses move toward the SE US, following the anticyclonic flow of the North Atlantic Subtropical High

(NASH). As the warm and humid tropical air masses move inland, they interact with the land surface to generate precipitation in this region. The diversified landscapes within the SE US domain, including complex terrain, vegetation, land use/land cover types, and land-sea distributions, exert differentiated forcing on these humid air masses (Rhee *et al.* 2008; Stooksbury and Michaels 1991). Thus, summer precipitation displays complicated spatial patterns within the SE US domain. According to k-means algorithm (Kalkstein *et al.* 1987), six representative summer rainfall clusters can be identified (Figure 1.2).

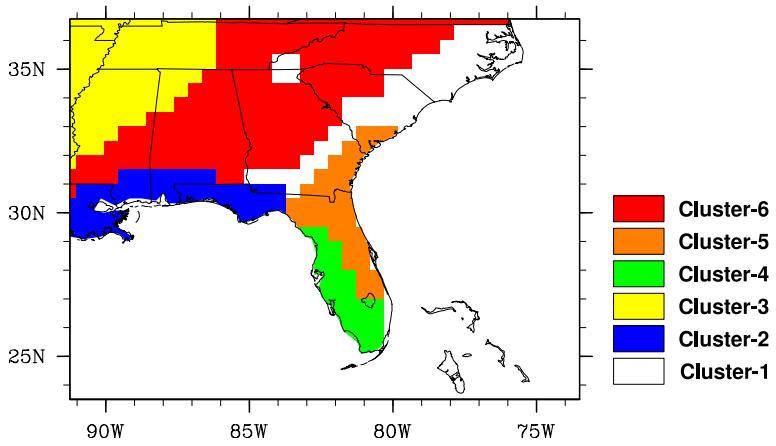

Figure 1.2: SE US summer precipitation clusters as identified using K-means algorithm

These six clusters include coastal clusters (cluster-1, 2, 4, and 5), an Appalachian cluster (cluster-6), and an interior cluster (cluster-3). Summer precipitation in these clusters is governed by different processes. Specifically, coastal precipitation is primarily generated owing to land-sea breeze circulation, which results from the differentiated land-sea heating rate (Miller *et al.* 2003; Simpson 1994). Land-sea breeze induced precipitation typically peaks in the afternoon, when the maximum land surface heating

contrast is achieved. The high pressure over the ocean results in a sea breeze that brings humid oceanic air masses to the land area. The land surface heating creates a conditionally unstable environment to facilitate the onset of thunderstorms and convective precipitation (Case *et al.* 2005; Miller *et al.* 2003). In addition, hurricane landfalls also significantly contribute to summer precipitation over the coastal areas by causing heavy precipitation and extreme events (Knight and Davis 2007).

Along the Appalachian Mountain range (Cluster-6), the mountain terrain provides mechanical forcing for the development of thunderstorms and convective precipitation (Roe 2005). Climatologically, this region experiences southeast upslope-flow precipitation in the summer resulting from the interaction between terrain orientation and large-scale seasonal circulation. Furthermore, the topography can also interact with the frontal systems to cause heavy rainfall events in the warm seasons (Konrad 1997; Lin *et al*. 2001).

In the interior domain (cluster-3), the contributions of tropical air masses to precipitation are relatively weak compared to the other 5 clusters. Thus, the amount of summer rainfall within this domain is relatively lower than that over the remaining regions (Higgins *et al.* 2007; Wang *et al.* 2010). For this domain, the passages of frontal systems contribute to some portion of the summer precipitation. Furthermore, the moisture from local evapotranspiration can also feed the precipitation (Ruane 2010), when unstable conditions for convection are met.

Averaged over the entire SE US domain, convective storms are the major contributors to warm season precipitation, while the contributions from frontal systems are secondary (Baigorria *et al.* 2007; Konrad and Perry 2010; Kunkel *et al.* 2012). The convective precipitation over the coastal regions is primarily modulated by the strength of land-sea breeze circulations (Keim *et al.* 2011; Misra *et al.* 2011). At the same time, convective precipitation induced by hurricane landfalls mainly contributes to heavy precipitation over the coastal regions, especially along the outer banks of North Caroline and coastal regions such as South Florida and South Louisiana (Barlow 2011; Keim *et al.* 2007; Knight and Davis 2007; Knight and Davis 2009). In contrast, over the Appalachian Mountain range, topography provides the mechanical forcing to facilitate the onset of convective precipitation in the summer.

It is noteworthy that the spatial domain influenced by convective precipitation is relatively small and the temporal scale is relatively short (Kunkel *et al.* 2010). Over a larger spatial area and at seasonal time scale, planetary-scale circulation systems predominantly control the summer precipitation over the SE US. These systems include the mid-latitude westerly and the NASH circulation, with the latter playing a more important role (Booth *et al.* 2006; Davis *et al.* 1997; Henderson and Vega 1996; Katz *et al.* 2003; Wang *et al.* 2010). The NASH circulation, especially along the western ridge, influences SE US summer precipitation by modulating large-scale moisture transport into this region, as well as by providing favorable dynamic conditions for the

development of convective systems. Thus, the SE US summer precipitation is particularly sensitive to the spatial and temporal variation of the NASH circulation.

In conclusion, processes and systems contributing to SE US summer precipitation span multiple spatiotemporal scales. Furthermore, these different processes and systems interact with each other, which complicates the diagnoses of rainfall variability over this region.

1.2 SE US summer precipitation and its climate drivers

The amount of summer precipitation falling in the SE US is influenced by a wide range of climate factors, including terrestrial and oceanic forcing, atmospheric internal circulation variability, and anthropogenic activities. These factors influence SE US summer precipitation by modulating rainfall generation systems as described in Section 1.1. As a result, summer precipitation over the SE US is sensitive to climate variability and climate change.

1.2.1 Terrestrial forcing on SE US summer precipitation

The land surface state influences precipitation through its interaction with the atmosphere, i.e. its influences on evaporation/evapotranspiration and large-scale circulation. As the typical time scale of soil memory is 2-3 month (Delworth and Manabe 1989), summer precipitation is usually related to springtime soil moisture and soil temperature. Observations and model simulations have shown that SE US summer

precipitation is closely related to springtime soil moisture in the local area (Wu *et al.* 2007) and subsurface soil temperature over the western US (Xue *et al.* 2012).

The springtime local soil moisture content is negatively correlated with summer precipitation over the SE US; the increase in soil moisture in the spring usually reduces summer precipitation (Wu *et al.* 2007). The changes in soil moisture can influence the partition of energy flux between the land and atmosphere, by which near surface relative humidity and temperature will be changed (Delworth and Manabe 1989). The anti-phase relationship between springtime soil moisture and summer precipitation might be due to the changes in boundary layer stability (Ek and Holtslag 2004; Gentine *et al.* 2013; Miller *et al.* 2005). Specifically, the increase in spring soil moisture tends to increase evaporation in the following months, which cools the land surface due to the release of latent heat. The cooler than normal land surface stabilizes the atmospheric boundary layer and thus depresses the onset of convection (Ek and Holtslag 2004; Miller *et al.* 2005). The decreased convective events reduce the amount of summer precipitation over the SE US.

Besides local soil moisture, springtime subsurface soil temperature over the western US (due to snow cover) also affects SE US summer precipitation (Xue *et al.* 2012). It is noticed that above normal springtime subsurface soil temperature over the western US is followed by excessive precipitation over the SE US during summer seasons (Xue *et al.* 2012). By performing regional climate simulations, Xue *et al.* (2012) found that spring soil

temperature over the Western US can affect the summer precipitation over the SE US by modulating the seasonal evolution of atmospheric circulation. Specifically, the warmer the springtime soil temperature is over the Western US, the stronger the land surface heating is generated over the local area. The enhanced surface heating generates positive potential vorticity in the lower troposphere and forces anomalous cyclonic circulation (Hoskins 1991; Liu *et al.* 2004; Wu and Liu 2000). The cyclonic circulation propagates downstream through Rossby waves in the background westerly wind (Ting and Wang 2006). The cyclone dissipates over the Northeast but enhances over the SE US (Xue *et al.* 2012). Such an anomalous cyclone enhances the convergence of moisture and facilitates stronger upward motion over the SE US, which favors excessive precipitation over the SE US.

1.2.2 Oceanic influences on SE US summer precipitation

SE US summer precipitation is also subject to remote forcing due to oceanic thermal conditions, i.e. sea surface temperature anomalies (SSTAs). The oceanic influence on SE US summer precipitation is mainly through the atmospheric teleconnection. According to previous studies, typical SSTA patterns affecting the SE US summer precipitation include the El Niño Southern Oscillation (ENSO) SSTA at interannual time scales, the variability of the Atlantic warm pool SSTA pattern, and the North Atlantic zonal SSTA. At decadal to inter-dacadal scale, SSTA variations associated with Pacific decadal

oscillation (PDO) and Atlantic multidecadal oscillation (AMO) predominate SE US summer precipitation variability.

a) Interannual scale

At interannual scale, ENSO variability and the associated atmospheric teleconnection patterns influence climate over a wide range of areas across the globe, including the SE US (Barlow *et al.* 2001; Mo and Schemm 2008; Ropelewski and Halpert 1987). The ENSO influence on SE US precipitation is, however, seasonally dependent. During the El Niño (La Niña) years, the SE US tends to have a relatively wet (dry) winter but dry (wet) summer, respectively (Mo and Schemm 2008; Ropelewski and Halpert 1987). Furthermore, the ENSO influence is the strongest during winter seasons and acts mainly through the modulation of jet stream and cyclone genesis (Eichler and Higgins 2006; Quadrelli and Wallace 2002). In contrast, as the jet weakens during summer, the ENSO influence becomes less significant and is confined to South Florida (Barlow *et al.* 2001; Changnon 1999; Mo *et al.* 2009). Over this region, the ENSO's impact is manifested by its regulation of Atlantic hurricane intensity and hurricane landfalls (Klotzbach 2011, 2012).

Compared to ENSO, SSTA over the North Atlantic exerts a stronger impact on SE US summer precipitation (Wang *et al.* 2013; Wang *et al.* 2010). Since the tropical Atlantic and Gulf of Mexico are the primary moisture sources for SE US summer precipitation (Chan and Misra 2010; Gimeno *et al.* 2010; Soulé 1998), SSTA over the tropical oceans, especially over the Atlantic warm pool, significantly influences the precipitation (Wang

et al. 2008). The changes in warm pool SSTA directly alters the land-sea temperature contrast over the coastal SE US, a driving force of land-sea breeze circulation. As a result, sea-breeze induced precipitation along the coasts is subject to change (Misra *et al.* 2011). In addition, warm pool SSTA influences SE US summer precipitation by affecting the hurricane track via the changes in the steering flows (Wang and Lee 2007; Wang *et al.* 2008). More importantly, the SSTA over the warm pool regions actively couples with the NASH circulation and can influence SE US summer precipitation through tropical-extratropical teleconnection. For example, the warmer SSTA tends to destabilize the marine boundary layer and favors the development of convection to release more condensational heating into the atmosphere. The diabatic heating induces Gill-type responses of the atmospheric circulation, with a cyclone generated northwest to the heating region (Gill 1980). The cyclonic circulation disturbs the tropical atmospheric vorticity balance by loading positive vorticity in the lower troposphere. The adjustment of tropical atmospheric circulation to positive vorticity generation excites a meridionally propagating Rossby wave train (Hoskins and Karoly 1981), which results in observed teleconnection patterns in 850hPa circulations between the tropical ocean and the SE US (Ji *et al.* 2014; Kosaka and Nakamura 2010). The teleconnection patterns modulate the circulation along the NASH western ridge, through which SE US summer precipitation is influenced (Li *et al.* 2012a).

Besides the tropical SSTA, a zonally oriented SSTA pattern spanning the mid-latitude North Atlantic is closely related to summer precipitation over the SE US (Wang *et al.* 2010). Specifically, the SSTA center is located in the mid-latitude of the North Atlantic (Gulf stream extension region), with the positive SSTA concurring with below average precipitation over the SE US (Wang *et al.* 2010). The mechanism linking the zonal SSTA mode and SE US summer precipitation might be two-fold. On the one hand, the zonal SSTA pattern is closely related to the distribution of 200hPa zonal wind over the eastern US (Wang *et al.* 2010). The zonal wind distribution in the upper troposphere changes the inertial stability of the atmosphere, which determines an atmospheric vertical motion and thus further changes the spatial distribution of precipitation over the Eastern US. On the other hand, the observed "SSTA-precipitation" relationship might result from the typical air-sea coupling over the mid-latitude, which is initiated in the preceding winter season (Hu and Huang 2006; Kushnir *et al.* 2002). Observations and model simulations suggest that the atmospheric disturbances in the winter generate SSTAs over the mid-latitude North Atlantic (Cayan 1992). The SSTAs, in turn, influence the overlying surface wind and sea level pressure (SLP) by disturbing the marine boundary layer stability and atmospheric heating pattern. The resultant wind and SLP induce anomalous Ekman pumping, which enhances the initial SSTA pattern. Such a coupling between SSTA and surface wind evolves through time and modulates basin-scale atmospheric circulation in the summer seasons (Hu and Huang 2006). It has been

shown that with the zonal SSTA pattern over the North Atlantic, an anomalous anticyclone/cyclone will be generated off the eastern coast during summer. The generated anticyclone/cyclone influences SE US summer precipitation by regulating the pathways of seasonal-scale moisture transport as well as trajectories of the Atlantic hurricanes (Colbert and Soden 2012; Li and Li 2013).

b) Decadal scale

Decadal- and interdecadal-scale SSTA variability associated with the AMO and PDO, also affects SE US summer precipitation, especially its low-frequency variability (Ortegren *et al.* 2011). Extensive studies have shown the role of AMO in controlling the SE US summer precipitation regime at decadal scale (Hu *et al.* 2011; McCabe *et al.* 2004; Ortegren *et al.* 2011). During the AMO positive (negative) phase, summer precipitation tends to decrease (increase) over the SE US (McCabe *et al.* 2004; Ortegren *et al.* 2011). The influence of AMO on decadal variation of SE US summer precipitation is through its forcing on basin-scale SLP: the positive (negative) AMO decreases (increases) SLP over the subtropical North Atlantic (Kushnir *et al.* 2010). The associated wind pattern further modulates moisture transport into the SE US, and thus influences summer precipitation. In addition to its impact on the large-scale circulation, the AMO phase significantly influences the intensity and track of Atlantic hurricanes (Curtis 2008; Maxwell *et al.* 2013). Furthermore, the phase of AMO largely determines to what extent ENSO can influence SE US summer precipitation. Specifically, the negative AMO phase is associated with enhanced ENSO modulation of hurricanes and SE US summer

precipitation. The ENSO's impact, however, weakens in the positive phase of AMO (Hu and Feng 2012; Keim *et al.* 2007; Klotzbach 2011; Mo *et al.* 2009).

By contrast, the influence of PDO on SE US summer precipitation is less well understood (Li *et al.* 2012a; McCabe *et al.* 2004). One possible mechanism might be the PDO's influence on stationary wave propagation and related dynamic forcing on atmospheric circulation along the NASH western ridge. In the positive phase of PDO, an anomalous stationary wave source will be excited off the coast of Western US (Barlow *et al.* 2001). This stationary wave propagates down stream and forms an abnormally high pressure over the Eastern US, with barotropic structures (Li *et al.* 2012a). Thus, the stationary wave induced by positive PDO SSTA favors the formation of high pressure over the SE US, which depresses the onset of convections and causes a deficit in rainfall (Li *et al.* 2012a). More recent studies indicate that the PDO influences on SE US summer precipitation involve the interplay between PDO SSTA and anthropogenic forcing (Li *et al.* In Preparation).

Overall, SE US summer precipitation is influenced by both the Atlantic and Pacific Oceans. However, the former tends to be more important at both interannual and decadal scales (Wang *et al.* 2013; Wang *et al.* 2010). The stronger influence of Atlantic SSTA likely occurs because the air masses contributing to SE US summer precipitation mainly originate from the Tropical Atlantic and the Gulf of Mexico (Gimeno *et al.* 2010; Soulé 1998).

1.2.3 Atmospheric internal mode and SE US summer precipitation

Atmospheric internal modes also influence SE US summer precipitation. Among these well-defined modes, North Atlantic Oscillation (NAO) and Pacific-North America (PNA) patterns are shown to have the most significant impact on SE US summer precipitation.

The influence of NAO is mainly through, but not limited to, the changes in intensity and positions of the Bermuda high (BH) (Anchukaitis *et al.* 2006). During the positive NAO phase, SLP increases over the subtropical North Atlantic, which enhances the BH. The stronger than normal BH results in stronger anticyclonic circulation over the subtropical North Atlantic, and thus favors stronger moisture transport into the SE US (Henderson and Vega 1996; Stahle and Cleaveland 1992). Consequently, wet (dry) summers are more likely to occur in the SE US when the NAO is in its positive (negative) phase (Anchukaitis *et al.* 2006). Compared to the broad area of the SE US domain, the NAO's influence might be different over the coastal regions where hurricane landfalls contribute significantly to summer precipitation (Knight and Davis 2007). The NAO positive (negative) phase is associated with stronger (weaker) westerly in the extratropics. As the weaker westerly is more likely to steer hurricanes towards the SE US to make landfall there (Maxwell *et al.* 2013), the NAO negative phase is more likely to increase the hurricane contribution to precipitation, especially extreme precipitation, over the coastal regions.

Besides NAO, the PNA teleconnection pattern also contributes to summer precipitation over the SE US, including total rainfall amount, rainfall duration, and the number of rainfall events (Henderson and Robinson 1994). The positive PNA phase is characterized by a more meridionally oriented circulation pattern across the Pacific-North America sector, i.e. intensified Aleutian Low, Western US ridge, and eastern US trough in the middle and lower troposphere (Wallace and Gutzler 1981). During summer seasons, the positive PNA pattern enhances the trough over the SE US. The circulation pattern associated with positive PNA dynamically favors more frequent convective activity and the clustering of rainfall events in the SE US (Henderson and Robinson 1994; Leathers *et al.* 1991).

Furthermore, summer precipitation over the SE US can be triggered by the atmospheric internal variability at different temporal scales. Due to the chaotic nature of atmospheric dynamics, stochastic processes also explain a certain amount of rainfall variance over the SE US (Seager *et al.* 2009).

1.2.4 Influences of Human activities on SE US summer precipitation

Another factor that may impact SE US summer precipitation is human activity, including changes in land use land cover (LULC) and emissions of greenhouse gases (GHGs). As one of the fastest developing areas of the country, the SE US has experienced substantial transformation in land cover since the late 20th century due to anthropogenic activities (Loveland *et al.* 2002). For example, over the Florida Peninsula,

the natural landscapes have been converted to agricultural and urban areas. The changes in LULC significantly alter the surface albedo, roughness length, Bowen ratio, and thus the heat and momentum exchange between the land surface and the overlying atmosphere. The resultant changes in land-sea heating contrast modulate the intensity of land-sea breeze circulation, which is a primary forcing for convective precipitation over the Florida regions. Studies show that the observed drying trend in Florida summer precipitation is largely attributable to the LULC changes (Marshall *et al.* 2004).

In addition to LULC change, climate over the SE US is also sensitive to the concentrations of GHGs in the atmosphere. The GHG forcing can drive changes in SE US summer precipitation both thermodynamically and dynamically. Thermodynamically, the increased GHGs warms and thus moistens the troposphere, which provides more moisture available for precipitation (Held and Soden 2006; Seager *et al.* 2010). At the same time, atmospheric circulation also responds to GHGs forcing. Evidence has shown that the NASH circulation, a critical driver of SE US summer precipitation, is expected to intensify and expand in a warming climate (Li *et al.* 2012b; Li *et al.* 2011). Thus, circulation patterns can dynamically alter the precipitation over the SE US. Given the compound thermodynamic and dynamic contributions, the response of SE US summer precipitation is highly uncertain according to the simulations by both regional climate models (RCMs) and general circulation models (GCMs) (Christensen *et al.* 2007; Mearns *et al.* 2012). Overall, the model simulated GHGs forcing on SE US

summer precipitation depends on the dynamic cores, physical parameterizations, as well as climate scenarios (Chen *et al.* 2003; Liang *et al.* 2006; Mearns *et al.* 2003).

1.3 Objectives of this dissertation

The mechanistic study of SE US summer precipitation variability is challenging due to complicated rainfall generation processes. Furthermore, due to the complexity of SE US summer precipitation mechanisms, both GCMs and RCMs have not yet developed the necessary skills to simulate the summer precipitation, which hampers reliable climate predictions over this region. Thus, there remains a pressing need to understand the SE US summer precipitation mechanisms and improve model simulations of summer precipitation over this region.

This dissertation investigates the mechanisms responsible for the variability of SE US summer precipitation in order to: 1) explore the causes of recent intensification of the summer precipitation variability; 2) provide process-based guidance to improve climate simulations and predictions over this region; and 3) project future precipitation change over the SE US and interpret future climate change mechanisms. First, Chapter 2 diagnoses the physical processes in relation with SE US summer precipitation variability by analyzing the regional moisture budget. Based on the results obtained in Chapter 2, Chapter 3 elucidates the climatic role of the NASH circulation on SE US summer precipitation, its contribution to intensified summer precipitation variability over this region, and the atmospheric dynamics constraining the NASH circulation. In Chapter 4,

the simulations of SE US summer precipitation by GCMs in the phase-5 of the Climate Model Intercomparison Project (CMIP5) and RCMs in North American Regional Climate Change Assessment Program (NARCCAP) are assessed at process-level. In Chapter 5, regional climate simulations using the Weather Research and Forecasting (WRF) model are performed in order to explore the potential sources to improve the simulations and predictions of SE US summertime climate. Chapter 6 projects future climate changes over the SE US, whereby we observed a pattern shift of the NASH ridge circulation. Conclusions obtained in this study are presented in Chapter 7.

2. Atmospheric moisture budget and its constrain on SE US summer precipitation variability

At seasonal scales, water vapor flux with a local atmospheric column is balanced between precipitation, evaporation, and the net moisture transport through the lateral boundary (Brubaker *et al.* 1993). Mathematically, the regional moisture balance is formulated as:

$$\rho_w g\left(\bar{P}-\bar{E}\right)=-\overline{\nabla\cdot\int_0^{p_s} q\vec{V}\,dp} \quad (2.1),$$

where P is precipitation, E is evaporation, and $\nabla\cdot\int_0^{p_s} q\vec{V}\,dp$ is the divergence field of moisture flux, which represents the net moisture transport through the lateral boundary of an atmospheric column (hereafter, "moisture transport" (MT) for abbreviation). The bar denotes the temporal average over each individual JJA season. The atmospheric moisture balance constraint implies that the changes in both local evaporation and moisture transport from remote sources can contribute to the variability of summer precipitation (Equation 2.1).

This study focuses on SE US summer precipitation variability at sub-continental-scales (horizontal scale > 1000 km). To characterize this large-scale feature and the moisture budget constrains on the precipitation variability, related hydroclimate variables are implemented from an areal-averaged perspective. We noticed a spatial heterogeneity in summer precipitation within the SE US domain. However, the variation of the summer precipitation is dominated by a spatially uniform feature as suggested by

the first empirical orthogonal function (EOF) mode (38% explained variance, Figure 2.1a). The principle component (PC) corresponding to the first EOF mode highly correlates with the areal-averaged summer precipitation (Figure 2.1b, R^2=0.95). Thus, the areal-averaged summer precipitation can reasonably reflect the sub-continental scale features of SE US summer precipitation variability; and the analysis based on the areal-averaged hydroclimate variables emphasizes the contribution of moisture transport and evaporation to the large-scale precipitation variability.

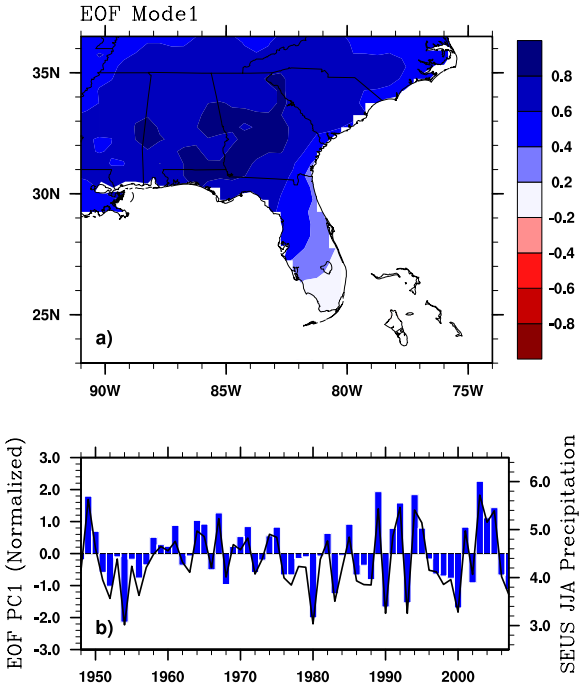

Figure 2. 1: a) Spatial patterns of the first EOF of JJA mean precipitation over SE US (91°W-76°W, 25°N-36.5°N); b) the normalized PC1 time series corresponding to the spatial pattern (bar, values are shown in the left axis), and areal-averaged SE US summer precipitation (black curve, units: mm day^{-1}, values are shown in the right axis).

2.1 Datasets and SE US regional moisture budget

2.1.1 Observed precipitation and atmospheric reanalysis datasets

In this study, the observed precipitation data is obtained from the National Oceanic and Atmospheric Administration (NOAA)'s PRECipitation REConstruction over Land (Prec/L) datasets, whose spatial resolution is 0.5° and the temporal resolution is monthly (Chen *et al.* 2002). The precipitation derived from this dataset has been compared with NOAA Climate Prediction Center (CPC) US Unified Precipitation (Higgins *et al.* 2000). The two datasets show indiscernible differences in quantifying SE US summer precipitation. The Prec/L is used here for its better temporal consistency.

The terms related to moisture transport (MT) in Equation (2.1) are calculated using the meteorological variables including specific humidity (q), horizontal wind ($\vec{V}$), and surface pressure (p_s). These variables are obtained from four independent reanalysis datasets to ensure the robustness of the study (Table 2.1): National Centers for Environmental Prediction (NCEP)/ National Center for Climate Research (NCAR) (Kalnay *et al.* 1996), European Center for Medium-Range Weather Forecasting (ECMWF) 40 Year Reanalysis (ERA-40) (Uppala *et al.* 2005), Japanese 25-year Reanalysis Project (JRA-25) (Onogi *et al.* 2007) and NCEP North American Regional Reanalysis (NARR) (Mesinger *et al.* 2006). As shown in Table 2.1, the spatial resolution of current reanalysis datasets are not fine enough to fully resolve the spatially heterogeneous features of SE US hydroclimate (Konrad 1997; Rhee *et al.* 2008). However, this study focuses on the

large-scale spatially homogenous features, which can be reliably captured by these datasets despite the coarse resolution.

Table 2.1: Reanalysis datasets used in this study

Datasets	Temporal Coverage; Resolution	Horizontal Resolution	Vertical Levels	Top Pressure Level
NCEP/ NCAR	1948-present; 6-hr	2.5°×2.5°	1000hPa-100hPa (17 levels)	300hPa for specific humidity and 100hPa for wind
ERA-40	1958-2002; 6-hr	2.5°×2.5°	1000hPa-10hPa (18 levels)	10hPa
JRA-25	1979-present; 6-hr	T106	995hPa-0.40hPa (40 levels)	0.4hPa
NARR	1979-present; 3-hr	32-km	1000hPa-100hPa (29 levels)	100hPa

The summer season is defined as June-July-August (JJA) and the seasonal mean refers to the average over the JJA. The JJA mean evaporation is derived as the residual of moisture balance between precipitation and MT (Equation 2.1), due to the limited temporal span of current evaporation datasets and the potential inaccuracy of evaporation in reanalysis datasets (Mueller *et al.* 2011; Ruane 2010).

2.1.2 Atmospheric moisture budget over the SE US in the summer

In the analysis, the moisture transport term in Equation 2.1 is further partitioned into three terms: moisture transport caused by JJA mean circulation, by subseasonal-scale eddies, and that associated with surface properties (Seager *et al.* 2010; Trenberth and Guillemot 1995). Thus, Equation (2.1) can be expressed as:

$$\rho_w g\left(\overline{P}-\overline{E}\right)=-\underbrace{\int_0^{p_s}\nabla\cdot\left(\overline{q}\overline{\vec{V}}\right)dp}_{MTM}-\underbrace{\int_0^{p_s}\nabla\cdot\overline{\left(q'\vec{V}'\right)}dp}_{MTE}-\underbrace{\overline{q_s\vec{V}_s\cdot\nabla p_s}}_{MTS} \quad (2.2).$$

In Equation (2.2), the JJA mean component is calculated using the seasonal mean of the variables in each JJA season. The prime denotes the departure from the JJA mean. According to Equation (2.2), regional atmospheric moisture balance is between precipitation (P), evaporation (E), and moisture transport by JJA mean flow (MTM), by subseasonal-scale eddies (MTE) and by surface properties (MTS: surface moisture flux across the gradient of surface pressure).

Analysis of Equations (2.1) and (2.2) enables the quantification of the contribution of local evaporation and moisture transport from remote sources in modulating the interannual variation of SE US summer precipitation. Furthermore, the relative importance of seasonal mean circulation (MTM) and subseasonal-scale eddies (MTE) can be compared according to their role in the moisture budget (Equation 2.2).

To assess the regulation of moisture budget upon the large-scale SE US summer precipitation, each term in Equation (2.2) is averaged over the terrestrial SE US (91°W~76°W, 25°N~36.5°N). The areal-averaged moisture budget can be expressed as:

$$\begin{aligned}\rho_w g\left(\left[\overline{P}\right]-\left[\overline{E}\right]\right)&=-\underbrace{\left[\overline{\nabla\cdot\int_0^{p_s}q\vec{V}dp}\right]}_{MT}\\&=-\underbrace{\left[\int_0^{p_s}\nabla\cdot\left(\overline{q}\overline{\vec{V}}\right)dp\right]}_{MTM}-\underbrace{\left[\int_0^{p_s}\nabla\cdot\overline{\left(q'\vec{V}'\right)}dp\right]}_{MTE}-\underbrace{\left[\overline{q_s\vec{V}_s\cdot\nabla p_s}\right]}_{MTS}\end{aligned} \quad (2.3),$$

where the [ ] denotes areal-averaged properties over the SE US.

Conventionally, the areal-averaged moisture transport can be calculated using two different methods: i) direct calculation of the divergence field of moisture flux over a specific region; ii) calculation of the net moisture flux through the lateral boundaries of an atmospheric column, which is subsequently divided by the area of the region. The two methods should generate the same results mathematically (Ninomiya and Kobayashi 1999). However, due to the irregular land-sea distribution, topography, and the spatial resolution of reanalysis data, discrepancies sometimes occur. Over the SE US, the first method calculates the areal-averaged divergence of moisture flux over the terrestrial area within the domain of 91°W -76°W; 25°N -36.5°N. The second method first integrates the moisture flux along the land-sea boundary from 91°W to 76°W and along 25°N and 36.5°N. The integrated net moisture flux is then divided by the total terrestrial area. The moisture transport term calculated by the two methods highly consistent throughout the analysis period (not shown). In this study, the first method was used.

2.2 Summertime hydroclimate over the SE US

By averaging each term in Equation (2.2) over the 1948-2007, the 60-yr climatology of summertime hydroclimate variables over the SE US are obtained and shown in Figure 2.2. Climatologically, summer precipitation in the SE US is characterized by a spatial gradient along the southeast-northwest direction, with higher precipitation (6 mm day^{-1}) near the coastal regions and lower precipitation (3-4 mm day^{-1}) inland. This precipitation

pattern may result from a thermally driven secondary circulation induced by localized land-sea heating contrast along the subtropical coastal areas (Wu et al. 2009). Such spatial features in precipitation are also reflected in the MTM, which is higher over the coastal regions than inland (Figure 2.2c). This is related with the circulation along the North Atlantic Subtropical High (NASH) western ridge (Minobe et al. 2010; Li et al. 2012). The spatial pattern of MTM (Figure 2.2c) is consistent with results in Nigam and Ruiz-Barradas (2006), Anderson et al. (2009), and Ruane (2010). Furthermore, MTE also contribute to moisture convergence along the coastal regions during summer (Figure 2.2d), but the magnitude is relatively small. In contrast, evaporation does not show clear pattern over the SE US, but local maxima in Florida, western North Carolina, and the northwest of the domain (Figure 2.2b).

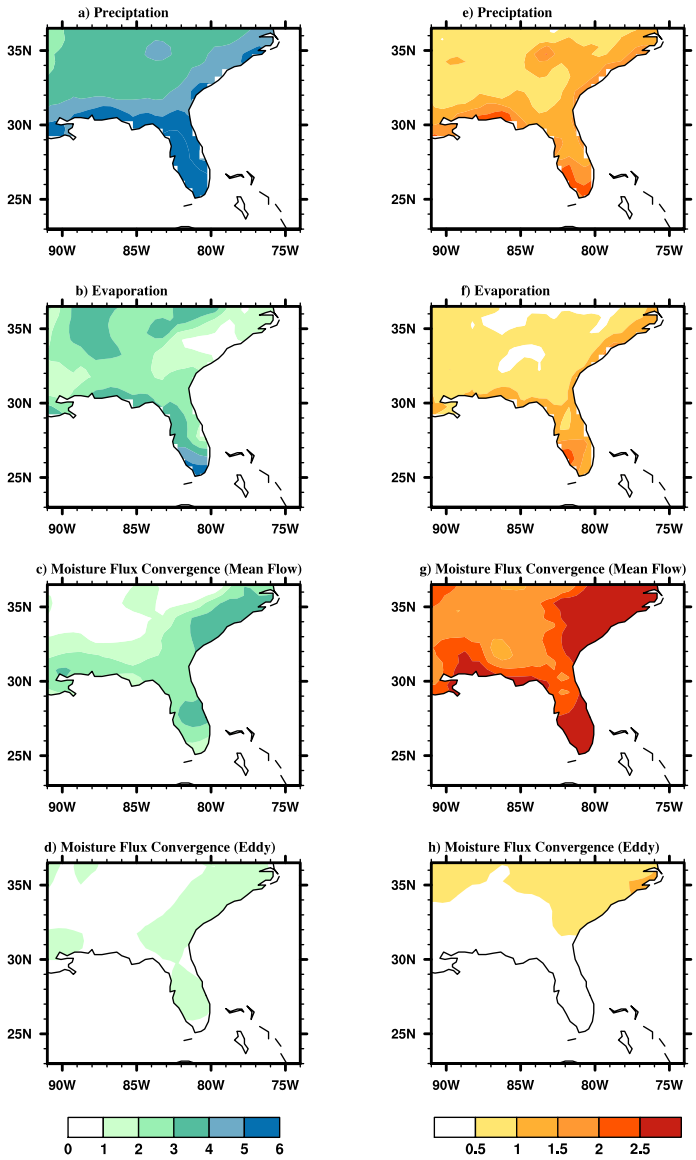

Figure 2. 2: Climatology (left panels) and variance (right panels) of SE US summer: a) and e) precipitation; b) and f) evaporation; and MT associated with c) and g) MTM, and with d) and h) MTE during the 1948-2007. The units of variables in a)-d) have been converted to mm day^{-1}, and those in e)-h) to mm^2 day^{-2}. The precipitation in a) and e) is derived from Prec/L; evaporation in b) and f), and MT components in c)-d) and g)-h) are derived from the ensemble of NCEP/NCAR, ERA-40, JRA-25, and NARR reanalysis datasets.

Over the SE US, the magnitude of evaporation exceeds MTM climatologically (Figure. 2.2b-d). This confirms previous results suggesting the importance of local

evaporation to summer precipitation in the eastern US (Anderson *et al.* 2009). However, evaporation is less important in terms of the variability of the summer precipitation. The reanalysis datasets collectively show larger variance of MTM than that of evaporation over the SE US (Figure 2.1f and g); and evaporation alone cannot fully explain the variance of SE US summer precipitation (Figure 2.2e).

Figure 2.3 shows the interannual variation of SE US summer precipitation (Figure 2.3a), evaporation (Figure 2.3b), and MT (Figure 2.3c) during 1948-2007. The 60-yr climatology has been removed to facilitate the comparison of the variability. Evaporation (Figure 2.3b) and MT (Figure 2.3c) are calculated from the ensemble of the four reanalysis datasets during their overlapping periods[1]. The results suggest that the variability of MT is stronger than that of local evaporation by about 78% (Figure 2.3b and c), since the standard deviation of the MT (evaporation) is 0.73 (0.41) mm day^{-1} for the 60-yr period. It is noteworthy that the in specific summers, the moisture budget quantified by the four reanalysis datasets might differ (Figure 2.3b and c). However, the 60-yr averaged standard error among reanalysis datasets is 0.15 mm day^{-1}, about 20% of the standard deviation of MT (0.73 mm day^{-1}) estimated by the reanalysis ensemble. The signal-to-noise ratio is approximately 5, suggesting the robustness of the moisture budget analysis based on current reanalysis datasets. In summary, the four reanalysis

[1] During 1958-1978, the time series are calculated as the average of NCEP/NCAR and ERA-40; during1979-2002, the time series are calculated as the average of NCEP/NCAR, ERA-40, JRA-25, and NARR; during 2003-2007, the average is among NCEP/NCAR, JRA-25 and NARR. From 1948-1957, the time series are shown as NCEP/NCAR results.

datasets consistently show that the MT (Figure 2.3c) contributes more to the variability of SE US summer precipitation than evaporation (Figure 2.3b), although the latter maintains the precipitation climatology (Figure 2.2b and Anderson *et al.* 2009; Ruane 2010).

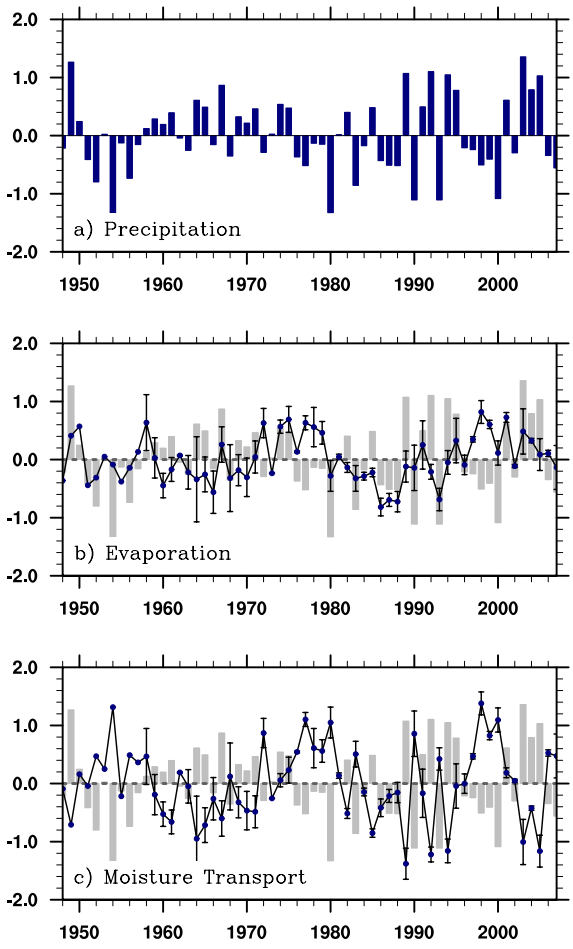

Figure 2. 3: Time series (1948-2007) of JJA seasonal mean a) precipitation anomaly (blue bar), b) evaporation anomaly (solid line) and c) MT anomaly (solid line) over the SE US In b) and c), the light-gray bar is the precipitation anomaly as shown in a); the blue dots denote the ensemble of the four reanalysis data and the error bar denotes the upper and lower bound by one standard error between available datasets. The units of precipitation, evaporation and MT have been converted to mm day^{-1}.

The role of MT is further supported by its close correlation with the interannual variation of SE US summer precipitation. Table 2.2 summarizes the correlation coefficients between precipitation and the remaining terms in Equation (2.3) using each reanalysis dataset and their ensemble. Because the variability of the summer precipitation has significantly intensified in the second 30 years (1978-2007) versus the first 30 years (1948-1977) (Wang *et al.* 2010), the 60 years are subdivided into two periods: 1948-1977 and 1978-2007 for the NCEP/NCAR reanalysis and the ensemble. Considering the relatively short temporal coverage, the ERA-40 time series are separated into two periods as 1958-1977 and 1978-2002. Correlation analysis is applied to both periods accordingly. For the JRA-25 and NARR that begins in 1979, only the period of 1979-2007 is considered.

Table 2.2 shows a strong correlation between SE US summer precipitation and MT ($\rho = -0.80$ according to the reanalysis ensemble) throughout the 1948-2007. In comparison, the correlation between precipitation and evaporation is relatively weak ($\rho = 0.30$). This general feature of SE US summertime moisture budget is consistent using the four different reanalysis datasets and between the two separate periods, albert the exact correlation coefficients slightly vary (Table 2.2).

Table 2.2: Correlation coefficients between SE US summer precipitation and the remaining terms in Equation (2.3) as derived from the NCEP/NCAR, ERA-40, JRA-25 and NARR and their ensemble. The correlation coefficients exceed 0.01 (0.05) significant levels are in bold italic (italic and underlined).

		MT	MTM	MTE	E
Ensemble	48-07	***-0.80***	***-0.72***	-0.01	*0.30*
	48-77	***-0.75***	***-0.71***	-0.07	0.29
	78-07	***-0.84***	***-0.73***	0.04	0.32
NCEP/ NCAR	48-07	***-0.71***	***-0.62***	0.07	***0.44***
	48-77	***-0.77***	***-0.60***	-0.08	*0.44*
	78-07	***-0.70***	***-0.67***	0.23	***0.45***
ERA -40	58-02	***-0.63***	***-0.65***	-0.01	0.25
	58-77	***-0.53***	***-0.61***	-0.05	0.05
	78-02	***-0.70***	***-0.66***	0.16	0.32
JRA-25	79-07	***-0.88***	***-0.71***	-0.14	0.16
NARR	79-07	***-0.69***	***-0.68***	0.18	*0.35*

Furthermore, the contribution of MT to SE US summer precipitation is mainly through the MTM component as shown by all four reanalysis datasets (Table 2.2). In addition, the MTM shows an approximately one-to-one relationship with the total MT and explains more than 90% of the variance (Figure 2.4a), far larger than that can be explained by the MTE (Figure 2.4b) and the MTS (Figure 2.4c). Meanwhile, the standard deviation of the MTE and MTS are about 75% and 87% smaller than that of the MTM, respectively. The results highlight the importance of MTM in controlling the variability of the MT from the areal-averaged perspective (Figure 2.4).

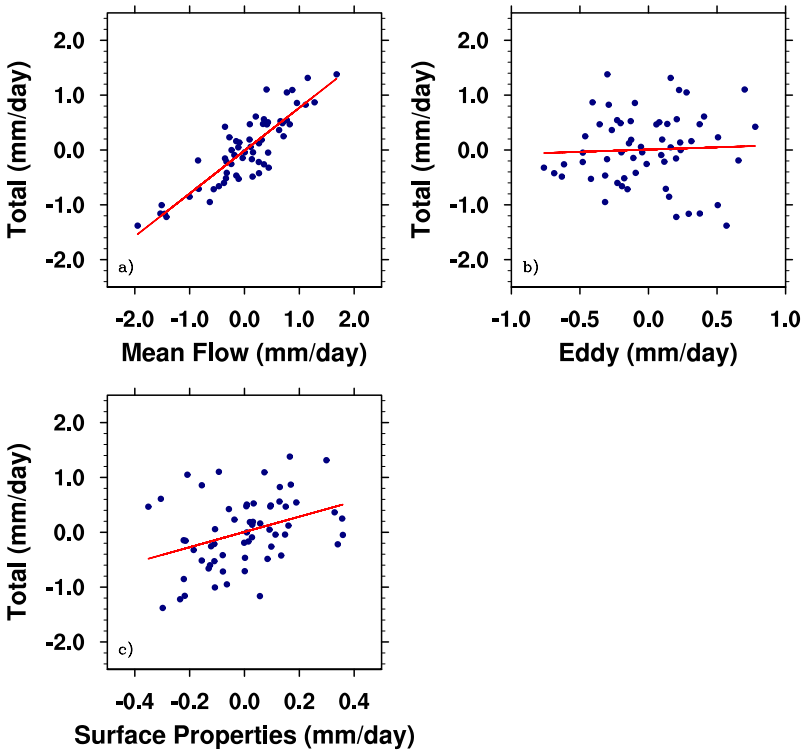

Figure 2. 4: SE US JJA mean MT versus its a) MTM; b) MTE; and c) MTS. The red lines in a), b) and c) are the best least squares fitting lines.

Previous studies have emphasized the importance of synoptic-scale systems, in particular hurricanes, in drought recovery along the storm paths and their contribution to the extreme precipitation over the coastal SE US (Douglas and Barros 2002; Knight and Davis 2009; Shepherd *et al.* 2007). However, from an areal-averaged perspective, our analysis suggests that these subseasonal-scale systems appear to be less important in precipitation variability over the SE US in summer (JJA). We noticed that the statistical peak of the Atlantic hurricane season is around September 10th, and JJA stops before the peak of tropical cyclone activity in the North Atlantic. Furthermore, hurricanes influence a relatively narrow domain after land falling (Barlow 2011; Sun and Barros 2012).

The above analysis focuses on the large-scale areal-averaged SE US summertime hydroclimate. According to previous studies, the interannual varation of SE US summer precipitation show certain spatial heterogeneity (Figure 1.2), in addition to the dominance of the large-scale domain-wide signal (EOF mode 1, Figure 2.1). We further analyzed the precipitation and moisture transport within each of the six rainfall clusters as shown in Figure 1.2. Generally, two major features concerning the temporal variation of SE US summer precipitation are in agreement among clusters. First, the summer precipitation experiences increased variability during the recent 30 years among all six clusters. Averaged over the six clusters, the standard deviation of the summer precipitation variability increases by 0.15 mm day^{-1} in recent 30 years (Figure 2.5), although the magnitude of increase is relatively small in cluster 5 (northern Florida and the coastal regions of Georgia, Figure 2.5). Second, moisture divergence largely explains the interannual variation of summer precipitation in each of the six clusters. Summer precipitation shows close linear relationship with the MT term (Figure 2.6), and the correlation coefficient passes the $\alpha = 0.01$ significance level.

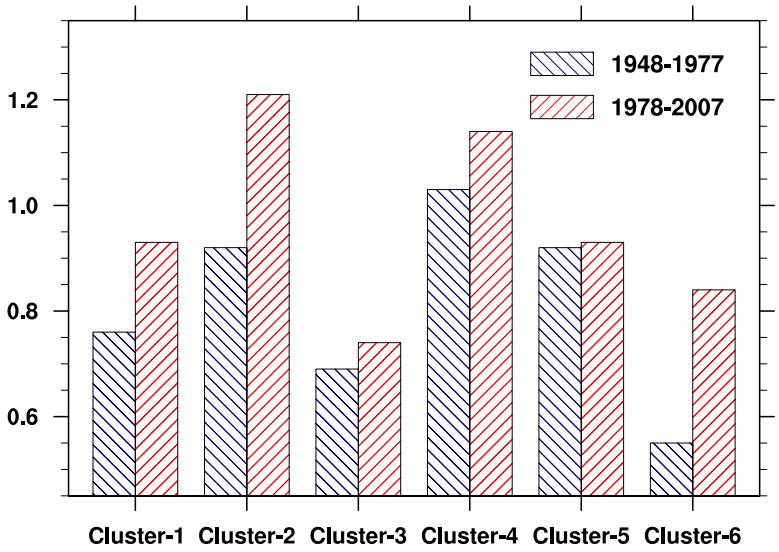

Figure 2. 5: Standard deviation of summer precipitation within each cluster as shown in Figure 1.2. The blue slashed bars represent the 1948-1977 period, and the red slashed bars represent the 1978-2007 period.

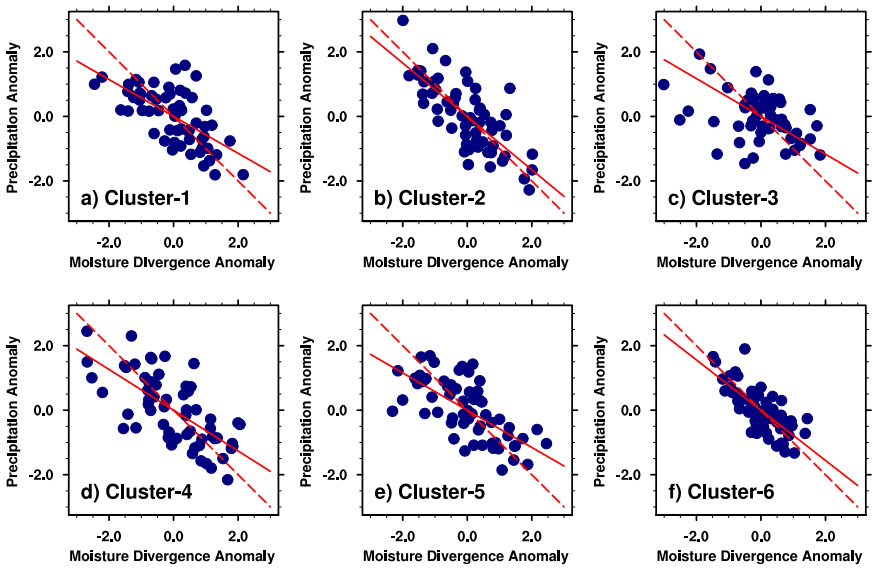

Figure 2. 6: The JJA mean MT anomaly versus precipitation anomaly within each SE US clusters (blue dots): a)-f). The red solid lines are the best least squares fitting lines and the red dashed lines are the $y = -x$ line.

The cluster analysis suggests that interannual variation of summer precipitation over the six SE US clusters shares similar characteristics in terms of the recent precipitation variability change and the dominant moisture budget processes. That is: 1) the summer precipitation variability has increased domain wide in recent 30 years (Figure 2.5); 2) MT is the predominant process for the interannual variation of SE US summer precipitation (Figure 2.6).

2.3 Summer precipitation variability and moisture transport processes

The analysis of SE US regional moisture budget suggests that MT, especially the MTM, primarily regulates the interannual variation of precipitation, while evaporation plays a secondary role. In contrast, the variability of SE US summer precipitation is almost independent of subseasonal-scale systems and surface properties. Thus, they are ruled out in the following discussion of precipitation variability change.

The causes of precipitation variability change are assessed using wavelet analysis. In the frequency domain, the intensified variability in SE US summer precipitation (Wang *et al.* 2010) can be interpreted as an increase of power spectrum energy towards higher frequency variability in recent decades. The wavelet analysis identifies not only the characteristic periodicity of a time series but also the non-stationary behavior of periodicity throughout the study period (Barros and Bowden 2008; Torrence and Compo 1998). Thus, it is particularly suitable to analyze the temporal evolution of precipitation

variability. In this study, the "Morlet" wavelet is used as the mother wavelet function because it well captures the oscillatory behaviors (Torrence and Compo 1998).

The wavelet analysis of the SE US summer precipitation identifies a significant 2-4 year power spectrum in the more recent 30 years (1978-2007), which is absent in the first 30 years (1948-1977) (Figure 2.7a). The evolution of the periodicity towards a stronger interannual variability indicates that the year-to-year fluctuations in SE US summer precipitation have intensified, and that the shift between extremely dry and wet summers is more frequent in the 2nd 30 years interval. The results obtained from the wavelet analysis are consistent with previous studies (Douglas and Barros 2002; Li *et al.* 2011; Wang *et al.* 2010).

To investigate the processes responsible for the intensified interannual precipitation variability, wavelet analysis was applied to evaporation (Figure 2.7b), MT (Figure 2.7c), and the MTM (Figure 2.7d), respectively. According to Figure 2.7b, the distribution of evaporation power spectrum differs from that of precipitation (Figure 2.7a) throughout the 60-yr period. No apparent increase in the 2-4 year periodicity is identified during the 1978-2007 compared to the 1948-1977 (Figure 2.7b). Instead, the power spectrum shows a multi-decadal signal (Figure 2.7b). However, because of the statistical "cone of influence", it is hard to ascertain whether this multi-decadal variation is physical or is artificially caused by the edge effects of the wavelet transform.

By contrast, the MT shows similar periodicity behavior to that of precipitation (Figure 2.7a and c). The significant power spectrum emerges in the 2nd 30 years within the 2-4 year band (Figure 2.7c). The 2-4 year power spectrum attains its maximum in the 1990s, which matches the occurrence of maximum power spectrum in the precipitation time series (Figure 2.7a). Furthermore, periodicity characteristics of the MT are largely determined by the MTM, as the evolution of power spectrum and the related periodicity are almost reproduced by the MTM time series (Figure 2.7d).

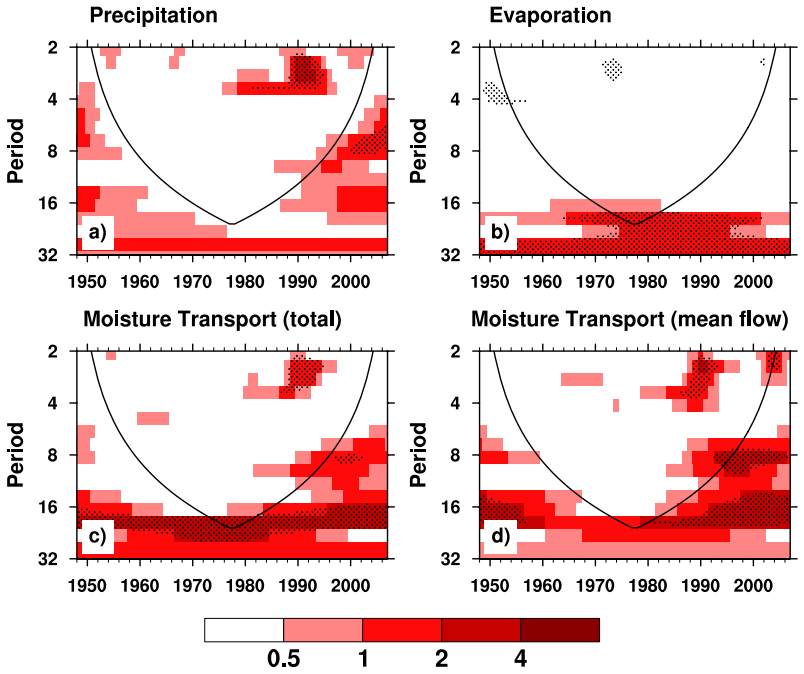

Figure 2. 7: Local wavelet power spectrum (shaded, units: $mm^2\ day^{-2}$) of SE US summer a) precipitation, b) evaporation, c) moisture transport, and d) the seasonal mean component of moisture transport in the 1948-2007. The time series used in b), c) and d) are from the ensemble of four reanalysis datasets. The left axis is the Fourier period (yr). The regions below the bold black curve indicate the "cone of influence", where edge effects become important. The stippled regions are significant at 0.05 significance level of red-noise process test.

To ensure that these diagnosed periodicity behaviors are robust and independent of the choice of reanalysis datasets, similar analysis using NCEP/NCAR and ERA-40 are shown separately in Figure 2.8. The two datasets span relatively longer periods, and are thus chosen to compare the moisture budget pattern in the 1st and 2nd 30 years.

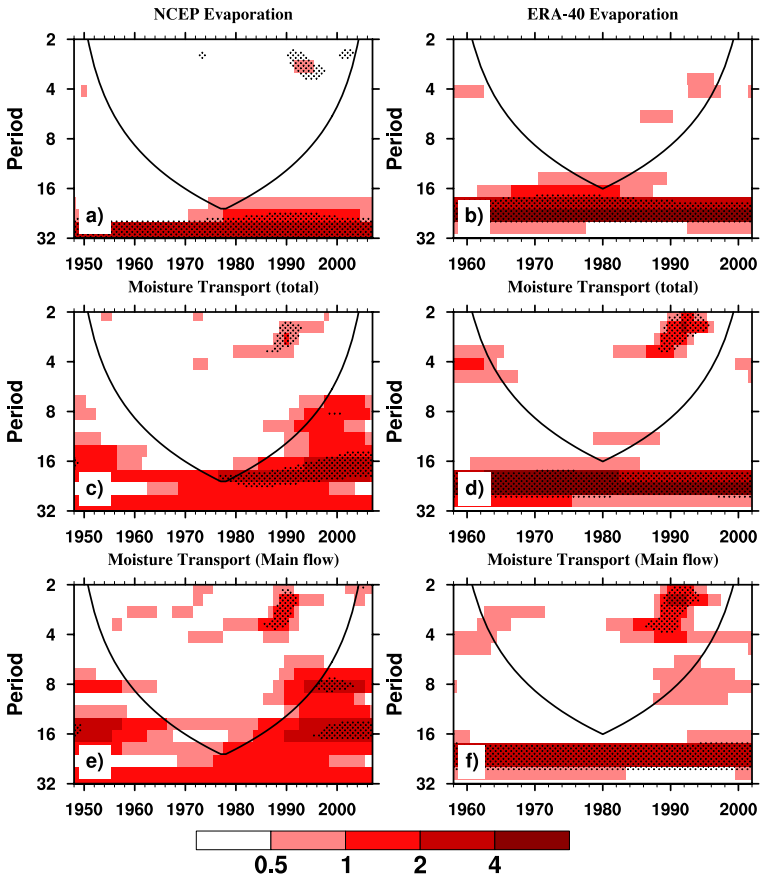

Figure 2. 8: The local wavelet power spectrum (shaded, units: $mm^2\ day^{-2}$) of SE US summer evaporation (a and b), MT (c and d), and the MTM (e and f) during the 1948-2007 (1958-2002) period using NCEP/NCAR (ERA-40). The left column (a, c, and e) shows the NCEP/NCAR results and the right column shows the ERA-40 results.

Similar to Figure 2.7, both datasets suggest that MT (especially MTM; Figure 2.8c-f) rather than local evaporation is more likely to cause the intensified interannual variation

in SE US summer precipitation in the 2nd 30 years, since the 2-4 year power spectrum peak is not reflected in evaporation (Figure 2.8a and b). The periodicity behavior depicted by both NCEP/NCAR and ERA-40 closely resembles that of the ensemble datasets (Figure 2.7), and the discrepancies between these two individual datasets are minor (Figure 2.8). Thus, the conclusion regarding summertime moisture budget over the SE US is robust.

Overall, the wavelet analysis identifies a significant 2-4 year power spectrum of precipitation in the 2nd 30 years, consistent with the enhanced interannual variability in SE US summer precipitation (Figure 2.7a). The reanalysis datasets and their ensemble consistently show that such increased 2-4 year power spectrum energy in the 2nd period is mainly caused by an intensified interannual variation in MT (Figure 2.7c), especially the MTM component (Figure. 2.7d).

2.4 Thermodynamic and dynamic contributions to SE US summer precipitation variability

The analysis above emphasizes the importance of MTM in enhancing SE US summer precipitation variability in recent decades. Mathematically, the variation of MTM is associated with both specific humidity (q) and wind velocity ($\vec{V}$). The two variables are associated with the thermodynamic and dynamic structures of the atmosphere, respectively (Seager *et al.* 2010). Both the thermodynamics and dynamics can modify regional moisture budget, however, their relative importance varies among

different scales and regions (Dairaku and Emori 2006; Kawase *et al.* 2010; Skific *et al.* 2009).

Whether the variation of MTM over the SE US is caused by thermodynamic or dynamic processes is investigated by separating the anomalies due to specific humidity and wind velocity (Seager *et al.* 2010). The specific humidity and wind velocity for each summer are expressed as $\overline{q} = \overline{q}_c + \overline{q}_a$ and $\vec{\overline{V}} = \vec{\overline{V}}_c + \vec{\overline{V}}_a$, where $\overline{q}_c$ and $\vec{\overline{V}}_c$ are the 60-yr (1948-2007) climatology of JJA mean specific humidity and wind velocity, respectively; and $\overline{q}_a$ and $\vec{\overline{V}}_a$ are the deviations from the 60-year climatology of each summer. The moisture transport can thus be expressed as:

$$\begin{aligned}\left[\int_0^{p_s} \nabla\cdot\left(\overline{q}\vec{\overline{V}}\right)dp\right] &= \left[\int_0^{p_s} \nabla\cdot\left(\overline{q}_c+\overline{q}_a\right)\left(\vec{\overline{V}}_c+\vec{\overline{V}}_a\right)dp\right] \\ &= \left[\int_0^{p_s} \nabla\cdot\left(\overline{q}_c\vec{\overline{V}}_c\right)dp\right]+\left[\int_0^{p_s} \nabla\cdot\left(\overline{q}_a\vec{\overline{V}}_c\right)dp\right]+\left[\int_0^{p_s} \nabla\cdot\left(\overline{q}_c\vec{\overline{V}}_a\right)dp\right]+\left[\int_0^{p_s} \nabla\cdot\left(\overline{q}_a\vec{\overline{V}}_a\right)dp\right]\end{aligned} \quad (2.4).$$

According to Equation (2.4), the variation of moisture transport can be decomposed into four terms quantified by $\left[\int_0^{p_s} \nabla\cdot\left(\overline{q}_c\vec{\overline{V}}_c\right)dp\right]$, $\left[\int_0^{p_s} \nabla\cdot\left(\overline{q}_a\vec{\overline{V}}_c\right)dp\right]$, $\left[\int_0^{p_s} \nabla\cdot\left(\overline{q}_c\vec{\overline{V}}_a\right)dp\right]$ and $\left[\int_0^{p_s} \nabla\cdot\left(\overline{q}_a\vec{\overline{V}}_a\right)dp\right]$. Since $\left[\int_0^{p_s} \nabla\cdot\left(\overline{q}_c\vec{\overline{V}}_c\right)dp\right]$ is stationary within the entire 60-year period, and $\left[\int_0^{p_s} \nabla\cdot\left(\overline{q}_a\vec{\overline{V}}_a\right)dp\right]$ can be neglected because both $\overline{q}_a$ and $\vec{\overline{V}}_a$ are usually small deviations from their climatologies (Seager *et al.* 2010), $\left[\int_0^{p_s} \nabla\cdot\left(\overline{q}_a\vec{\overline{V}}_c\right)dp\right]$ and $\left[\int_0^{p_s} \nabla\cdot\left(\overline{q}_c\vec{\overline{V}}_a\right)dp\right]$ are the major contributors to the interannual variation of large-scale moisture transport.

The temporal variation of $\left[\int_0^{p_s}\nabla\cdot\left(\overline{q}_a\vec{\overline{V}}_c\right)dp\right]$ ($\left[\int_0^{p_s}\nabla\cdot\left(\overline{q}_c\vec{\overline{V}}_a\right)dp\right]$) is solely determined by the changes in specific humidity (wind velocity) as the wind velocity $\vec{\overline{V}}_c$ (specific humidity $\overline{q}_c$) is set to its climatology, i.e. a constant, and thus represents the thermodynamic (dynamic) contribution. These two terms together largely determine the year-to-year deviation of MTM from the 60-year climatology, and are quantified by Equation (2.5) as follows:

$$\underbrace{\delta\left[\int_0^{p_s}\nabla\cdot\left(\overline{q}\vec{\overline{V}}\right)dp\right]}_{MTM}\approx\underbrace{\left[\int_0^{p_s}\nabla\cdot\left(\overline{q}_a\vec{\overline{V}}_c\right)dp\right]}_{Thermo}+\underbrace{\left[\int_0^{p_s}\nabla\cdot\left(\overline{q}_c\vec{\overline{V}}_a\right)dp\right]}_{Dyn} \quad (2.5).$$

Figure 2.9a shows the temporal evolution of the thermodynamic and dynamic components of MTM over the SE US[2]. Comparatively, the standard deviation of the dynamic component (0.74 mm day^{-1}) is 4 times larger than that of the thermodynamic component (0.17 mm day^{-1}). Furthermore, the R^2 between moisture transport and its dynamic component exceeds 0.90, indicating that the large majority of the MTM variance can be explained by the atmospheric circulation (wind) patterns.

Wavelet analysis of the thermodynamic and dynamic components confirms the predominance of dynamic components in causing the intensified variability of MTM

[2] NCEP/NCAR reanalysis instead of ensemble time series is used hereafter for the following reasons. First, The NCEP/NCAR is the only one of the four reanalysis datasets covering the whole 60-yr period. Second, the credibility of using NCEP/NCAR is ensured because the results derived from NCEP/NCAR shows qualitatively similar characteristics of the summertime hydroclimate over the SE US as the other reanalysis datasets over their overlapping period based on our comparison analysis.

and thus the summer precipitation. The wavelet power spectrum of the dynamic components (Figure 2.9c) demonstrates a similar periodic evolution to that of moisture transport (Figure 2.7c) and precipitation (Figure 2.7a) with an increased 2-4 year power spectrum in the last three decades. The thermodynamic component, on the other hand, shows less change during the 60-year period (Figure 2.9b). Thus, the summertime general circulation patterns are likely the leading drivers of the variability in moisture transport and thus precipitation over the SE US (Figure 2.9a).

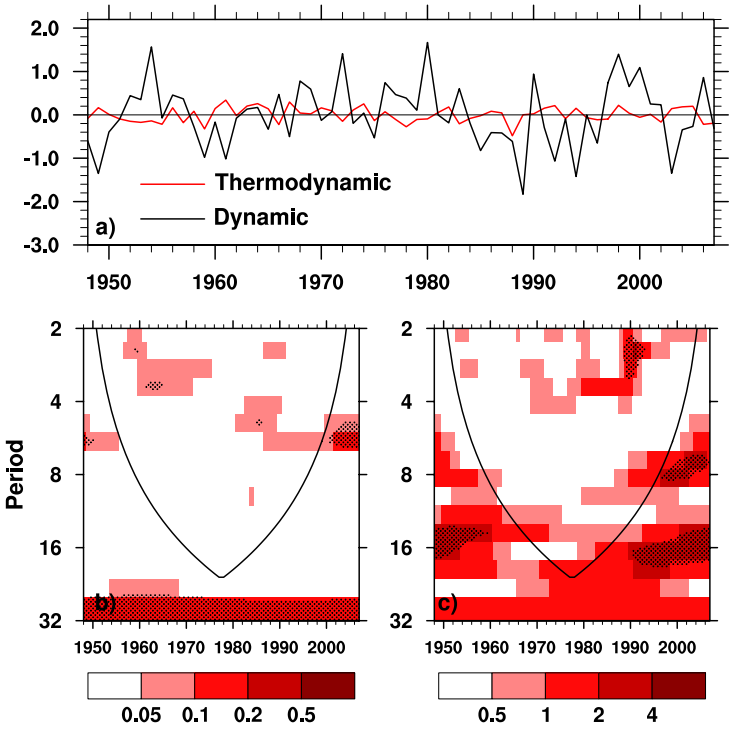

Figure 2. 9: a) MTM anomalies (unit: mm day^{-1}) over the SE US associated with the thermodynamic (red curve) and dynamic (black curve) components in the 1948-2007; and the local wavelet power spectrum (shaded, units: mm^2 day^{-2}) of the thermodynamic b) and dynamic c) component time series using "Morlet" wavelet.

2.5 Summary and conclusions

In recent decades, SE US summer precipitation variability has intensified with more frequent occurrence of anomalously dry and wet summers (Wang *et al.* 2010). The causes of the increased precipitation variability are studied by analyzing the regional moisture budget processes (i.e., precipitation, evaporation, and moisture transport in Equations 2.1-2.3).

Using multiple reanalysis datasets, the analysis of regional moisture budget shows that evaporation contributes to summer precipitation climatology over the SE US but plays a secondary role on precipitation variability over the region. In contrast, moisture transport (MT), especially the MTM, is the primary driver of summer precipitation variability over the SE US (Figures 2.2-2.3). Furthermore, the MTE contributes a relatively small portion to the observed variability of summer precipitation, although synoptic-scale systems (e.g. hurricanes and tropical cyclones) generally make an important contribution to the local water cycle and especially drought recovery (Atallah *et al.* 2007; Konrad and Perry 2010).

Wavelet analysis shows an increase in precipitation power spectrum at the 2-4 year periodicity band during the 1978-2007 compared to the 1948-1977, confirming the recent intensification of interannual precipitation variability over this region. The wavelet power spectrum of each moisture budget component indicates that this 2-4 year power spectrum peak mainly results from the MT, especially the MTM, due to their similar

power spectrum patterns to that of the precipitation. In contrast, the periodicity evolution of evaporation differs from that of the precipitation and contributes less to the intensified precipitation variability in recent decades (Figure 2.7).

The MTM is further partitioned into thermodynamic and dynamic components to assess the contribution of specific humidity and atmospheric circulation (wind pattern) to the variability of SE US summer precipitation (Equation 2.5). The results show that more than 90% of the variance of MTM can be explained by the dynamic component. Furthermore, the dynamic component in the 1948-2007 period exhibits a periodic behavior similar to that of the MTM and precipitation throughout the same 60-yr period (Figure 2.9). Thus, the year-to-year fluctuation in summertime atmospheric circulation is most likely to regulate MTM and enhance precipitation variability in recent decades.

3. Dynamic contributions of the NASH to SE US summer precipitation

The moisture budget analysis presented in Chapter 2 points at the large-scale seasonal mean circulation as a primary regulator of the interannal variation of SE US summer precipitation. Among the rain-bearing circulation systems, the North Atlantic Subtropical High (NASH) is probably of the highest importance for SE US summer precipitation (Henderson and Vega 1996; Katz *et al.* 2003; Li *et al.* 2011). This study investigates the relationship between the NASH and SE US summer precipitation and elucidates its contributions to the intensified summer precipitation variability in recent decades.

3.1 Introduction and Background

The NASH is a semi-permanent high-pressure system occupying the lower troposphere over the subtropical North Atlantic Ocean. In the summer, the NASH intensifies and its center is located near Bermuda (Davis *et al.* 1997; Nigam and Chan 2009; Seager *et al.* 2003). Its western ridge, extending into the SE US, supplies warm and humid air masses from the tropical oceans to feed large-scale summer precipitation over the SE US (Davis *et al.* 1997; Diem 2006; Gamble *et al.* 2008; Soulé 1998; Stahle and Cleaveland 1992). In other words, the NASH western circulation is directly related to moisture conditions over the SE US, which makes the summer precipitation there sensitive to the circulation dynamics along the western ridge.

Climatologically, summertime circulation along the NASH western ridge is primarily constrained by the conservation of atmospheric potential vorticity (PV). The western ridge located over a region where $u \approx 0$. According to the scale analysis, the conservation of PV along the western ridge is the balance between the advection of planetary vorticity and the generation/consumption of PV by mass convergence/divergence, i.e. $\beta v \propto -f\frac{\partial \omega}{\partial p}$ (Wu and Liu 2003; Wu *et al.* 1999; Wu *et al.* 2009). With the prevalence of southerly wind, upward motion is expected along the western ridge in order to balance the advection of planetary vorticity by the southerly wind (Liu and Wu 2004; Wu and Liu 2003; Wu *et al.* 2009). Furthermore, in the upper troposphere, a high-pressure system presents over the North American monsoon region (Adams and Comrie 1997). The northerly wind along the eastern portion of the monsoon ridge together with the southerly wind along the NASH western ridge results in a vertical shear of meridional wind. The shear of the wind generates secondary circulation, which enhances upward motion northward of the NASH ridge-line. Since the upward motion is one of the determinants for rainfall generation, high precipitation rates likely occur along the northwestern flank of the NASH western ridge. Thus, the circulation along the NASH western ridge largely determines the spatial distribution of summer precipitation over the North Atlantic and North America (Gamble *et al.* 2008; Li *et al.* 2011; Minobe *et al.* 2010; Thibeault and Seth 2014).

As shown in Figure 3.1, a rain-belt, characterized by precipitation rate greater than 4 mm day^{-1}, is aligned along the northwestern edge of the NASH, especially the 850hPa 1560-geopotential meter (gpm) isoline. The SE US is located right within the rain-belt as defined by the northwestern flank of the NASH, where high precipitation rates and strong vertical motion are observed in the summer (Figure 3.1). It thus indicates that SE US summer precipitation is sensitive to the changes of the NASH western ridge circulation (Katz *et al.* 2003; Li *et al.* 2011). However, the exact relationship between the location and motion of the NASH western ridge and the variability of SE US summer precipitation has not yet been systematically investigated.

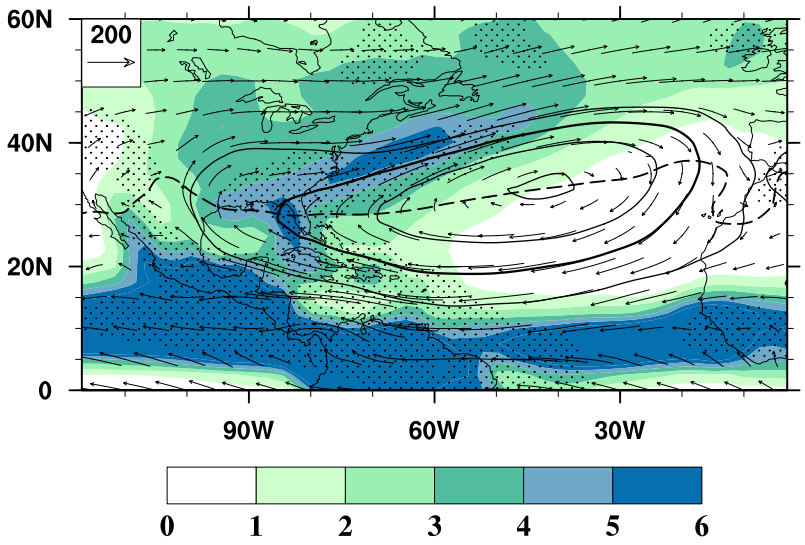

Figure 3. 1: JJA mean precipitation rate (shaded, unit: mm day^{-1}), 850hPa geopotential height (solid contour, unit: gpm), 850hPa subtropical high ridge line (dashed line) and moisture flux (vector, unit: kg m s^{-1}). The contour interval of 850hPa geopotential height is 20-gpm, and the bold curve is the 1560-gpm isoline. The area with 500hPa vertical velocity less than -0.01Pa s^{-1} is stippled.

In this study, we analyze the relationship between SE US summer precipitation and the spatial displacement of the NASH western ridge during the years 1948-2007. The study aims to 1) explore the physical mechanisms by which NASH western ridge influences SE US summer precipitation; and 2) investigate the factors and processes that are responsible for the spatial and temporal variation of the NASH western ridge. The results obtained in the study aid in our understanding SE US summer precipitation mechanism, which provides a process-level guidance to improve the simulations of SE US summer precipitation by numerical models and their reliability in projecting future precipitation over the region.

3.2 Displacement of the NASH western ridge and its relationship with SE US summer precipitation

In this study, 850hPa geopotential height instead of sea level pressure is used to represent the NASH circulation, in order to avoid the complications due to possible topographic effects on the western edge of the NASH. The ridge-line of the subtropical highs is where tropical trade winds reverse to midlatitude westerlies. Thus, it mathematically fulfills that $u = 0$ and $\frac{\partial u}{\partial y} > 0$, where u is the zonal wind component (Liu and Wu 2004). Following the previous studies, the 1560-gpm isoline[1] is chosen to

[1] As convention, the 850hPa geopotential height is usually plotted at 60-meter intervals with the reference level 1500 meters. For the North Atlantic subtropical high, the 1500-gpm line is far into the continent while 1620-gpm isoline is still over the North Atlantic; The 1560-gpm line is also

represent the boundary of the NASH. The western ridge is defined as the intersection point between the 1560-gpm isoline and the defined ridge line (Li *et al.* 2011).

According to the locations of the ridge relative to its 60-yr (1948-2007) climatology (86°W, 27°N), we categorize four ridge types by dividing its area of influence into four quadrants. In the 60-yr period, summers with the NASH western ridge in the first, second, third, and forth quadrant were identified as Northeast (NE), Northwest (NW), Southwest (SW), Southeast (SE) years, respectively (Figure 3.2).

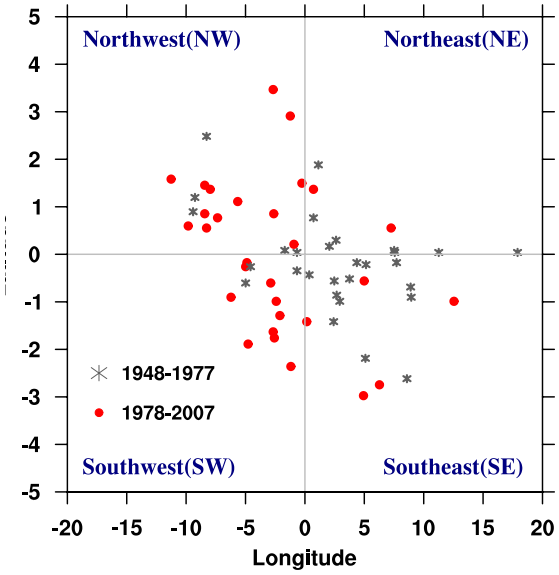

Figure 3. 2: Locations of the NASH western ridge relative to its climatological mean position (86°W, 27°N) during the 1948-2007, as derived from NCEP/NCAR reanalysis dataset.

Figure 3.2 demonstrates the interannual variations of the NASH western ridge relative to its climatological mean location (86°W, 27°N) in the boreal summer during the

---

closely related to the distribution of precipitation and vertical motion over the eastern coast of US (Figure 3.1).

60-yr period (1948-2007). Previous studies, as well as those presented in Chapter 2, have shown that the variability of summer precipitation in the SE US has intensified during the last three decades (1978-2007) compared to the earlier three decades (1948-1977) (Wang *et al.* 2010). Thus, the 60 locations of the NASH western ridge are plotted in Figure 3.2 using two different shapes to highlight the difference between the two periods. In the first 30-yr period, the distribution of western ridges was concentrated in the NE and SE quadrants; whereas in the second 30-yr period, about 80% of ridges were located in the SW and NW quadrants. This indicates a westward extension of the ridge similar to that described in Li *et al.* (2011). In the most recent 30 years (1978-2007), 40% more ridges were located in the NW quadrant (Figure 3.2).

In order to analyze the relationship between zonal and meridional movement of the NASH western ridge and summer precipitation over the SE US, composite analysis is then applied to determine the precipitation, atmospheric circulation, and sea surface temperature (SST) features corresponding to the four different types of the NASH western ridges (Figure 3.2). Monte-Carlo method is applied to test the statistical significance and robustness of the composite results (Livezey and Chen 1983; Wilks 1995). Monte Carlo simulations are repeated 1000 times for each composite analysis.

3.2.1 "NASH western ridge – SE US summer precipitation" relationship

Using observed precipitation, NCEP/NCAR, and ERA-40 reanalysis datasets, Figure 3.3 depicts the relationship between the NASH western ridge types (Figure 3.2) and SE

US summer precipitation. Corresponding to the different types of the NASH western ridge, precipitation exhibits different patterns over the Conterminous US.

In summers when the NASH western ridge shows NW-type, above-normal precipitation anomalies are observed over the Northwestern US, and especially over the Great Lakes (Figure 3.3a and e). In contrast, negative anomalies of precipitation are observed mainly in the SE US (Figure 3.3a and e). The rainfall deficit exceeds 0.8mm day^{-1} over the SE US, equivalent to 1.2 standard deviation of summer precipitation in this region (Wang *et al.* 2010), and is statistically significant ($\alpha = 0.05$ level) according to the Monte-Carlo simulations. Such a reduction in summer precipitation would place great stresses on water availability in the SE US during the years when ridge present a NW-type. Overall, the spatial distribution of precipitation anomalies shows a North-South oriented dipole pattern (Figure 3.3a and e).

Precipitation anomalies corresponding to the SW-type ridge cases exhibit an opposite pattern to those during NW years (Figure 3.3b and f). Negative rainfall anomalies are located over the Northern US, whereas positive anomalies prevail over the SE US, except the southern Florida. Precipitation anomalies are usually above one standard deviation in Alabama, Georgia, Tennessee, and the western Carolinas. The US precipitation anomalies in response to SW-type ridge are consistent between the NCEP/NCAR and ERA-40 reanalysis datasets (Figure 3.3b and f).

Generally, SE US summer precipitation shows a stronger response to the meridional migration of the NASH western ridge when the ridge extends westward (Figure 3.3a, b, e and f). However, precipitation anomalies over the SE US are not as significant and less uniform when the ridge is located relatively east (Figure 3.3c, d, g, and h). Specifically, the precipitation corresponding with the NE ridges is characterized by negative anomalies over the Northern United States and the Ohio Valley (Figure 3.3c and g). The average precipitation anomaly is less uniform and insignificant in the Southern US. Significant positive anomalies in precipitation are confined to a narrow region extending from the Northeastern US to Texas. Furthermore, SE US summer precipitation anomalies in NE-yr differ between the two reanalysis datasets. Specifically, the NCEP/NCAR (ERA-40) composite shows a slightly above (below) normal precipitation (Figure 3.3c and g). This discrepancy suggests a larger uncertainty in the response of SE US summer precipitation to the western ridge position when the ridge is located relatively eastward. Overall, both positive and negative precipitation anomalies are 50% weaker in the southern states compared with those in the Midwest (Figure 3.3c and g). The precipitation anomalies are weakest when the NASH western ridge is located in the SE quadrant (Figure 3.3d and h). Significant anomalies occur only in the south of Texas (dry), as well as Oklahoma and Arkansas (wet).

In conclusion, summer precipitation over the SE US is sensitive to the spatial displacement of the NASH western ridge, both its zonal and meridional movement.

Specifically, as the zonal extent of the western ridge moves more westward toward the Conterminous US, the influence of the ridge on SE US summer precipitation becomes more significant. When the ridge is in a NW location, the SE US tends to experience rainfall deficit and thus dry summers. However, wet summers are more likely occur when the ridge presents a SW type. In contrast, as the western ridge retreats eastward its impact on SE US summer precipitation weakens, as both NE and SE-type ridges correspond to precipitation anomalies that are insignificant over this region. It is noteworthy, that the influence of the NASH western ridge movement is not limited to the SE US. For example, wet summers over the Great Plains and Northeastern US are associated with a NW and SW-type ridge, respectively (Figure 3.3 a, b, e, and f). However, the how NASH circulation influences the precipitation over these regions are beyond the scope of this study.

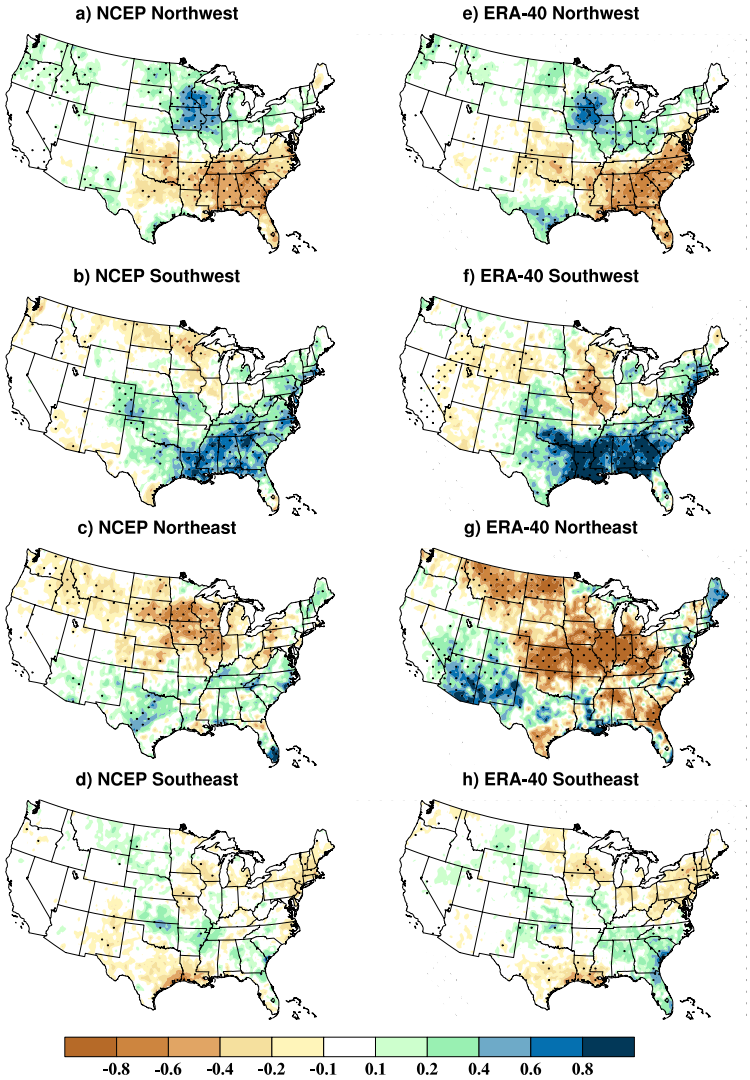

Figure 3. 3: US summer precipitation anomalies (shaded; mm day^{-1}) composite upon the NASH western ridge locations derived from the NCEP/NCAR (left column) and ERA-40 (right column) reanalysis datasets. Stippled areas show where precipitation anomaly is statistically significant at the 95% level.

3.2.2 Dynamic contributions of the NASH western ridge circulation to SE US summertime moisture budget

The relationship between the NASH western ridge circulation and SE US summer precipitation as described in the previous section is likely established through the

dynamic alteration of moisture transport by the ridge location. The NASH western ridge circulation associated with the dynamic component of moisture transport (Equation 2.5) is shown in Figure 3.4a-b. Generally, anomalous convergence of moisture likely occurs when the ridge is located in a relatively southwestward position (26°N, 87°W) compared to its climatology (Figure 3.4a). The SW-type ridge thus favors excessive precipitation over the SE US by supplying more moisture into this region. In contrast, anomalous moisture divergence is to be observed when the western ridge is located in a northwestward position (32°N, 94°W) relative to its climatology (Figure 3.4b), a typical northwest (NW)-type ridge pattern (Figure 3.2).

The regulative effects of the NASH western ridge in the dynamic component of moisture transport (Equation 2.5) are further quantified by examining its two subcomponents A and B as follows:

$$\int_0^{p_s} \nabla \cdot \left(\overline{q}_c \vec{\overline{V}}_a \right) dp = \underbrace{\int_0^{p_s} q_c \nabla \cdot \vec{\overline{V}}_a \, dp}_{A} + \underbrace{\int_0^{p_s} \vec{\overline{V}}_a \cdot \nabla \overline{q}_c \, dp}_{B} \quad (3.1),$$

where term A quantifies the contribution from the anomalous mass divergence acting upon the climatological moisture field; and term B is the contribution from the anomalous wind field acting upon the gradient in the climatological moisture field.

The contributions of term A and term B to $\int_0^{p_s} \nabla \cdot \left(\overline{q}_c \vec{\overline{V}}_a \right) dp$ and the corresponding NASH western ridge locations are shown in Figure 3.4c-f. The position change of the NASH western ridge regulates JJA moisture transport mainly by altering mass

convergence/divergence over the SE US (term A). When the ridge is in SW position, the anomalous mass converge causes 0.8 mm day^{-1} excessive moisture convergence over the SE US (Figure 3.4c). In contrast, when the ridge is in NW position, anomalous mass divergence is observed, which weakens the moisture convergence and tends to cause drought over the SE US (Figure 3.4d). The anomalous mass convergence (divergence) over the SE US during SW (NW) years might be results of atmospheric potential vorticity (PV) balance along the subtropical high western ridge[2] (Liu and Wu 2004). Compared with term A, the contribution of term B is relatively small over the SE US, except over the northern part of the domain (Figure 3.4e and f).

[2] From PV balance, strong mass convergence is expected north of the western ridge-line to balance the advection of planetary vorticity by southerly wind (Wu and Liu 2003; Liu *et al.* 2004; Wu *et al.* 2009). Thus, when the ridge moves southwestward, the SE US is located north of the ridge-line, strong mass convergence facilitates moisture convergence and thus excessive rainfall there (Figuew 3.4a and c). In contrast, when the ridge moves northwestward into the US continent, mass convergence is weakened over the SE US, which depresses summer precipitation (Figure 3.4b and d).

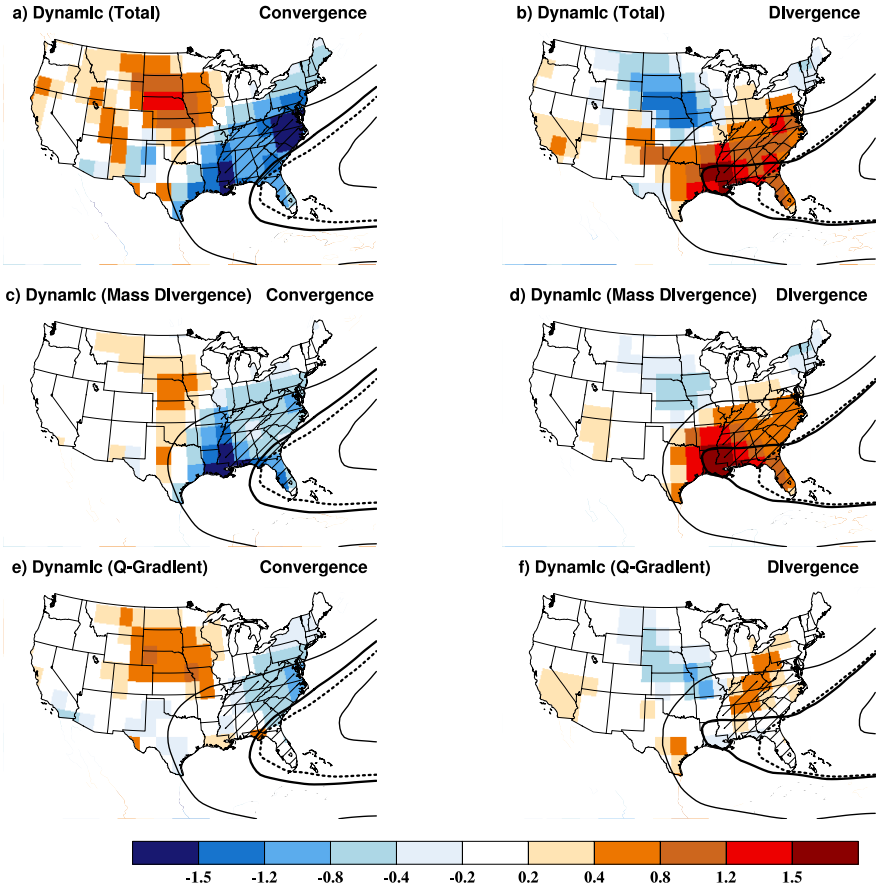

Figure 3. 4: Atmospheric moisture transport anomaly and the NASH western ridge composited upon the anomalous convergence (left panels) and divergence (right panels) of the dynamic component of MTM over the SE US ($\left[\nabla\cdot\int_0^{p_s}\left(\overline{q}_c\vec{\overline{V}}_a\right)dp\right]$): a) and b) are the dynamic component ($\nabla\cdot\int_0^{p_s}\left(\overline{q}_c\vec{\overline{V}}_a\right)dp$); c) and d) are mass divergence subcomponent (term A in Eq. (3.1)); e) and f) are moisture gradient subcomponent (term B in Eq. (3.1)). The solid black contours represent the composited 850hPa geopotential height (contour interval is 20-gpm, and the bold lines are the 1560-gpm isoline). The dashed contours are the climatology of 850hPa 1560-gpm isoline. The slashed region is the SE US domain. The anomalous convergence (divergence) is defined as $\left[\nabla\cdot\int_0^{p_s}\left(\overline{q}_c\vec{\overline{V}}_a\right)dp\right]<-1std\left(>1std\right)$.

In summary, the analysis of Equation (3.1) further emphasizes the importance of the NASH western ridge circulation in SE US summer precipitation. The observed "NASH western ridge-SE US summer precipitation" relationship is established through the

dynamic modulation of mass convergence/divergence and thus moisture transport over the SE US (Figure 3.4c-d). In recent decades, the frequency of both NW and SW type ridges has increased (Figure 3.2). Changes in the NASH circulation cause increased variability in moisture transport, an important factor governing SE US moisture budget and thus summer precipitation variability. This result supports Li *et al.* (2011)'s conclusion that the westward extension of the NASH western ridge combined with its intensified north-south movement collectively contribute to the intensified summer precipitation variability during 1978-2007.

3.3 Mechanism of the NASH western ridge movement

Atmospheric circulation fields were analyzed in order to identify the processes that contribute to the movement of the NASH western ridge. Figure 3.5 illustrates the composite results of 850hPa geopotential height and anomalies that correspond to each of the four ridge types. When the NASH western ridge extends westward, positive geopotential height anomalies are observed over the Atlantic Ocean (Figure 3.5a and b). In contrast, negative anomalies are observed when the ridge retreats eastward (Figure. 3.5c and d). Specifically, when the ridge is located in the NW quadrant, the NASH's center is around 35°N, 40°W. Significant geopotential height anomalies extend from Northern Africa to the SE US along the southern flank of the NASH. The maximum

response of positive geopotential height anomalies is over the SE US, whereas no significant signals are observed near the NASH's center (Figure 3.5a).

In summers dominated by SW quadrant positions, the NASH's center is located at (30°N 45°W), with an increase of intensity by 5 gpm (Figure 3.5b). The center of the subtropical high, as represented by the area enclosed by the 1600-gpm isoline, is the largest among the 4-ridge composites (Figure 3.5). Positive geopotential height anomalies are more uniform over the North Atlantic in summers with a SW ridge position than when it is in a NW position (Figure 3.5a). The maximum positive anomalies fall close and around the mean location of the NASH center (Figure 3.5b). This indicates that SW ridging might be mainly caused by the intensification and expansion of the NASH system.

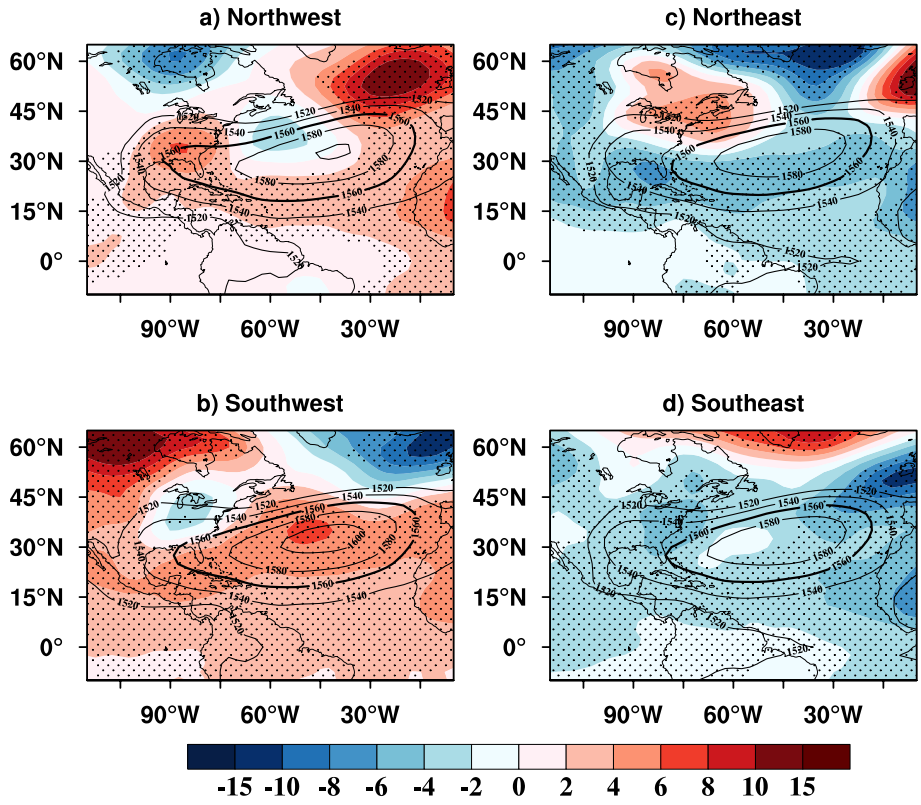

Figure 3. 5: 850hPa geopotential height (contour, unit: gpm), and geopotential height anomaly (shaded, unit: gpm) composite upon the NASH western ridge position. The bold contours are the 1560-gpm isoline. Stippled are where the geopotential height anomaly is statistically significant at the 95% level.

For both NE and SE ridge types (Figure 3.5c and d), the intensities of the NASH center are ~1590 gpm, about 10 gpm weaker than when NW and SW ridge types are present (Figure 3.5a and b). This suggests that a weakened NASH leads to an eastward retreat of the NASH western ridge (Figure 3.5c and d).

Overall, an intensified (weakened) NASH is related to the westward extension (eastward retreat) of the NASH western ridge and thus an enhanced (weakened) impact

on the SE US summer rainfall. Of the two westward ridges, the SW type is more likely linked with the intensification and expansion of the NASH, whereas the NW type shows less apparent relationship with the NASH center's intensity. Instead, the maximum geopotential height anomalies are located over the SE US, suggesting influences other than the NASH center contribute to NW ridging. Here we are more interested in the two western ridges because of the more important role they play in influencing SE US precipitation. Hereafter, we will focus on the possible mechanism responsible for these SW and NW ridge locations.

3.3.1 Contribution of the NASH center intensity to the SW-type ridge

The atmospheric circulation in summers with SW ridging is characterized by the intensification and a uniform expansion of the NASH (Figure 3.5b). The intensification of the NASH enhances the subtropical circulation over the North Atlantic (Figure 3.6a): the easterly winds south of the NASH ridge are observed to strengthen near the surface and in the lower troposphere (Figure 3.6a and b). Augmentation of the easterly winds (Figure 3.6b), accelerates the heat loss from the ocean's surface, mainly in the form of surface evaporation. Such heat loss would lower SST and thus cause negative SSTAs over the tropical Atlantic region (Figure 3.6b). Cold SSTs can, in turn, reinforce the anticyclone (Kushnir *et al.* 2010; Seager *et al.* 2003).

The lowered SSTs, caused by the enhanced surface evaporation, stabilizes the atmospheric boundary layer. This can be seen by an increase of static stability at the

lower atmospheric layer in Figure 3.6d. In SW ridge years, the static stability increases below 800hPa, indicating that more energy is required to overcome the atmospheric stratification for upward motion and convection to take place. Thus, tropical convective activity tends to be depressed and precipitation decreases.

Using the Global Precipitation Climatology Project (GPCP) data (Huffman *et al.* 1997), we found that precipitation over the Caribbean is significantly below normal with decreased SST in the SW summers (Figure 3.6c). Consequently, condensational heating associated with precipitation would decrease in the middle troposphere. The decreased Caribbean precipitation during SW years is consistent with previous studies that link the severity of Caribbean mid-summer drought to the intensity of NASH (Gamble *et al.* 2008; Kelly and Mapes 2011). Such a reduction in condensational heating would induce a Gill-type atmospheric response (Gill 1980), with an anomalous anticyclone to the northwest of the heating center. Co-located with the southern portion of the NASH western ridge, this anticyclonic circulation facilitates the southwestward extension of the NASH ridge (Kushnir *et al.* 2010).

To verify that NASH center's intensification favors SW ridging, a linear regression analysis of 850hPa geopotential height upon the NASH center's intensity was performed (Figure 3.6e). Figure 3.6e shows that when the NASH center's intensity increases by one standard deviation, the NASH tends to expand southwestward and the 1560-gpm

isoline extends by three degrees westward relative to its average climatological position. This is similar to the composite results based on analysis of the SW ridges (Figure 3.5b).

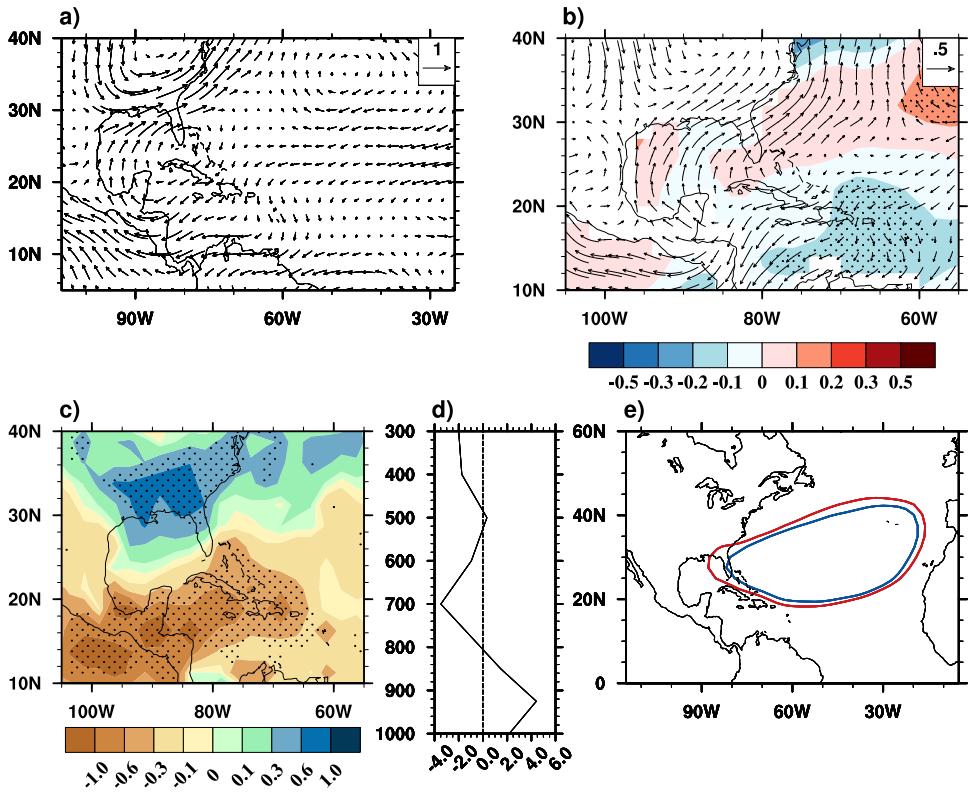

Figure 3. 6: Composite of a) 850hPa wind anomaly (vector, unit: m s^{-1}); b) Surface wind anomaly (vector, unit: m s^{-1}) and SSTA (shaded, unit: K), stippled areas show where SSTA is statistically significant at the 95% level; c) Precipitation anomalies measured by GPCP data (unit: mm day^{-1}); d) Vertical profile of Brunt-Vaisala frequency anomaly (unit:10^{-6} s^{-2}) averaged over tropical North Atlantic oceans (80°W-60°W, 12.5°N-20°N) in the SW summers. e) 1560-isoline of 850hPa geopotential height regressed upon NASH center's intensity: red (blue) contour marks the regression result when the NASH center intensity increased (decreased) by one standard deviation.

3.3.2 Relationship between the Pacific Decadal Oscillation (PDO) and the NW-type ridge

In contrast to the SW-type ridges, the NASH center's intensity shows no significant deviation from its climatology when the NASH western ridge is located in the NW

quadrant. The maximum 850hPa geopotential height anomaly is observed over the SE US (Figure 3.5a). Furthermore, the atmospheric circulation associated with the NW ridging demonstrates an equivalent barotropic structure with both lower and upper atmospheric layers dominated by positive geopotential height anomalies, as seen from the vertical profile of the geopotential height anomalies averaged over the SE US (30^{o}N-37.5^{o}N) in NW-position years (Figure 3.7a). Positive anomalies of geopotential height are significant throughout the whole troposphere. The center of the positive geopotential height anomaly in the upper troposphere is located over the Mid-west (Figure 3.7a), and shifts to the SE US near the surface (Figures 3.5a and 3.7a). The barotropic structure is spatially uniform along all latitudes in the SE US (not shown).

The barotropic structure shown in Figure 3.7a indicates that the local thermal forcing, especially the condensational heating associated with precipitation anomalies, is not a forcing factor for the NW ridging because local diabatic heating in the summertime subtropics tends to cause a baroclinic response of the atmospheric circulation (Liu *et al.* 2004; Wu and Liu 2003; Wu *et al.* 2009). Thus, the NW ridging is more likely caused by dynamic forcing (Figure 3.7a).

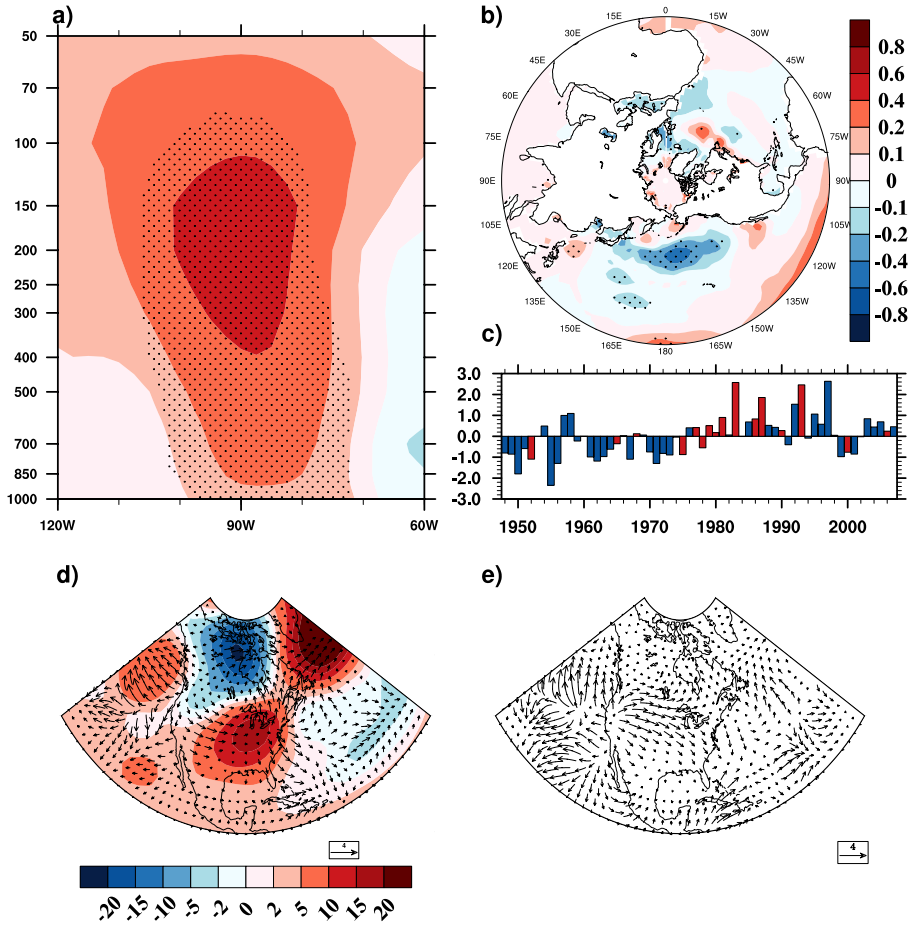

Figure 3. 7: Composite of a) Vertical profile of geopotential height (shaded, unit: gpm) along the 30°N-35°N latitudinal band; and b) SSTA (shaded, unit: K) in the NW summers. c) Time series of the PDO index during 1948-2007 where the red bar denotes NW summers. d) Composite 200hPa geopotential height anomaly (shaded, unit: gpm) and Plumb flux anomaly (vector, unit: $m^2 s^{-2}$), and e) Composite plumb flux anomalies (vector; $m^2 s^{-2}$) for positive PDO index. Stippling in a) and b) denotes areas where geopotential height and SSTA are statistically significant at the 95% level. The color scale in a) is the same as that in d).

Figure 3.7b shows the composite SSTAs when the NASH western ridges are located in the NW quadrant. As seen from Figure 3.7b, significant SSTAs are mainly located in the North Pacific. In contrast, the North Atlantic SSTAs are relatively weak and insignificant (Figure 3.7b). Figure 3.7b indicates that the NW ridging is more likely

associated with Pacific rather than with Atlantic SSTAs. In the North Pacific, positive SSTAs are observed in the tropics and negative SSTAs in the mid-latitudes. Such a pattern is similar to the SSTA associated with the PDO (Mantua and Hare 2002; Mantua *et al.* 1997; Zhang *et al.* 1997). Although SSTA during the NW years exhibit positive anomalies over the tropical eastern Pacific, their magnitudes are too weak to be statistically significant. We conclude that the SST anomalies are mainly forced by the PDO instead of the ENSO.

To further verify the possible influence of the PDO on NW ridging, Figure 3.7c lists the times series of the PDO index and NW years during the years 1948-2007. The PDO index is negative during 1947-1976 and becomes positive during 1977-2007, with a regime shift in 1976/1977 (Mantua and Hare 2002, Figure 3.7c). In the 60-yr interval, 13 NW summers occur within a positive and 6 summers within a negative PDO phase. The fact that the number of NW-position years during the positive PDO phase is more than double the number during the negative PDO phase, suggests that the decadal variation of Pacific SSTA impacts the NASH western ridge position by modulating the stationary wave source over the eastern Pacific/ US western coast (see Figure 3.7d-e).

The Plumb flux (Plumb 1985), an extended form of Eliassen-Palm flux, is calculated to diagnose the wave activities associated with PDO SSTA and NW-type ridge. The Plumb flux has previously been applied to diagnose the source regions and propagation path of stationary waves (Black 1997), atmospheric teleconnection (Franzke *et al.* 2001;

Honda *et al.* 2005), and the impact of external forcing on US climate (Barlow *et al.* 2001; Chen and Newman 1998). The horizontal component of Plumb flux is expressed as follows:

$$F_\lambda = \frac{p}{2a^2\cos\phi}\left[\left(\frac{\partial\psi'}{\partial\lambda}\right)^2 - \psi'\frac{\partial^2\psi'}{\partial\lambda^2}\right] \quad (3.2)$$

$$F_\phi = -\frac{p}{2a^2}\left(\frac{\partial\psi'}{\partial\lambda}\frac{\partial\psi'}{\partial\phi} - \psi'\frac{\partial^2\psi'}{\partial\lambda\partial\phi}\right) \quad (3.3),$$

where p is the pressure level, $a = 6.37\times10^6 m$ is the Earth's radius, λ and ϕ are longitude and latitude, respectively, and ψ' represents the deviation of stream function from its zonal mean. For steady flows over reasonably long periods, such as the seasonal mean, Plumb flux is parallel to the group velocity of the stationary waves and its divergence (convergence) is associated with their source (sink) (Plumb 1985).

Figure 3.7d shows composite results of 200hPa geopotential height and Plumb flux anomalies during the NW years. The positive anomalies in geopotential height over North America appear to be part of the stationary wave train in the Northern hemisphere. Stationary wave flux diverges from the midlatitudes of the eastern Pacific/US western coast and moves towards the positive geopotential height anomaly center over the eastern US This indicates that the observed stationary wave activity over the US is forced from the eastern Pacific/US western coastal region. The composite Plumb flux anomaly at 200hPa, based on the PDO positive index during the years 1948-2007, is illustrated in Figure 3.7e. The pattern of the Plumb flux in the NW years (Figure

3.7d) resembles that of the Plumb flux composite of the positive PDO phase (Figure 3.7e), suggesting that NW-type ridges are favored to occur in the warm phase of the PDO.

The quasi-barotropic character of stationary wave activity of the eastern Pacific/western US coastal region explains the observed vertical structure of the geopotential height anomalies in Figure 3.7a and the anomalous geopotential height at 850hPa level over the SE US (Figure 3.5a). The latter favors the northwestward extension of the NASH western ridge.

3.4 Summary and Conclusions

Using NCEP/NCAR and ERA40 reanalysis datasets, US Unified Precipitation data, and the real-time US Daily Precipitation Analysis, variations in the NASH western ridge and its potential influence on the SE US summer precipitation were studied. Our results show that the circulation dynamics along the NASH western ridge is constrained by the conservation of PV, specifically the balance between the advection of planetary vorticity and mass convergence along the western ridge. Such a dynamic constrain makes SE US summer precipitation particularly sensitive to the spatial displacement of the NASH western ridge. Consistent with Li *et al.* (2011), Our results confirm that the western ridge of the NASH has moved westward in the last three decades. By dynamically modulating

moisture transport, these changes in the NASH have impacted the patterns of SE US summer precipitation.

Our composite results, based on the two-dimensional displacement of the NASH western ridge relative to its climatological mean position, indicate that the westward relocation of the NASH western ridge causes more uniform and enhanced precipitation anomalies over the SE US. When the NASH western ridge is located in the SW (NW) quadrant, the SE US experiences severe pluvial conditions (drought). In contrast, the precipitation anomalies weaken when the NASH western ridge is located relatively eastward. Such a "NASH western ridge – SE US summer precipitation" relationship provides a first-order dynamic controls on SE US summer precipitation, and serves as a process-based metric to evaluate GCMs and RCMs in simulating summertime hydroclimate over this region (Wuebbles *et al.* 2013).

The significance of the NASH western ridge locations to SE US summer precipitation is manifested in its regulative effects on the dynamic component of moisture transport. A NW (SW)-type ridge corresponds to anomalous divergence (convergence) of moisture over the SE US, resulting in deficit (excessive) regional precipitation. Furthermore, the dynamic influence of the NASH on SE US summertime moisture budget is mainly through the changes in lower tropospheric mass convergence.

These ridge patterns are connected with conspicuously different atmospheric circulation patterns controlled by distinct physical mechanisms. The SW type is likely

the results of the intensification and systematic expansion of the NASH system. This enhancement of the North Atlantic subtropical circulation is viewed to increase surface winds and evaporation resulting in decreased SSTs over the Gulf of Mexico. The cooling of the surface ocean would depress tropical convection, resulting in decreased condensational heating. Accompanying this diabatic-heating anomaly, the atmospheric circulation shows a typical Gill-type response with an anticyclone developing northwest of the diabatic heating anomalies. Such circulation would favor the southwestward extension of the NASH western ridge. Thus, our results suggest that the SW ridge type involves the interaction of the NASH system with the tropical ocean, which may stem from the NASH center intensification.

The atmospheric circulation in the NW years exhibits a weaker link to the NASH center change. Instead, the maximum increase of geopotential height is over the SE US with an equivalent-barotropic pattern. This suggests that influence from local diabatic heating is less important. Analysis of Plumb flux indicates that the anomalous geopotential height over the SE US might be dynamically forced by a stationary wave train emanating from the western coast of the US, a situation that is associated with the positive phase of the PDO.

Our analysis of the NASH western ridge patterns and SE US summer precipitation suggests that enhanced precipitation variability in recent decades is a combined result of the PDO and NASH center intensifications that are associated with global warming (Li

et al. 2011). In the future, as warming continues, the frequency of SW-type ridge positions are predicted to increase significantly, resulting in increasingly wet summers in the SE US. However, this wetting trend will occasionally be opposed by drying summers when NW-ridge types occur during the positive PDO phases.

4. GCM and RCM simulations of SE US summer precipitation and the role of the NASH

Numerical models, including general circulation models (GCMs) and regional climate models (RCMs), have been widely applied to simulate global and regional climate as well as to project future climate change. However, the skill of GCMs and RCMs in simulating precipitation diverges among different regions and seasons (Flato *et al.* 2013; Mearns *et al.* 2012). It remains unclear how reliable GCMs and RCMs can simulate SE US summer precipitation, and what processes contribute to their skill in simulating the summer precipitation.

Previous studies suggest that the NASH and its western ridge movement largely regulated SE US summer precipitation (Davis *et al.* 1997; Henderson and Vega 1996; Katz *et al.* 2003; Li *et al.* 2012a; Li *et al.* 2011). More importantly, the study presented in Chapter 3 has established a relationship between the NASH western ridge locations and SE US summer precipitation. Specifically, when the ridge is located relatively northwestward (southwestward), dry (wet) summers tend to occur over the SE US. This relationship provides a first-order dynamic control on SE US summer precipitation from the perspective of regional moisture balance (Wuebbles *et al.* 2013). Furthermore, it has been noticed that the impact of many climate factors on SE US summer precipitation is likely through modulating the NASH western ridge circulation (Hu *et al.* 2011; Li *et al.* 2012a; Wang *et al.* 2008). It implies that a reasonable simulation of the relationship

between the NASH western ridge and summer precipitation over the SE US might be a key factor.

This study aims to assess the skill of the "state-of-the-art" GCMs and RCMs in simulating SE US summer precipitation, and to elucidate the physical mechanisms responsible for such skill. Specifically, the scientific questions are: 1) how well can the "state-of-the-art" GCMs and RCMs simulate SE US summer precipitation?; 2) what role does NASH play in determining the GCM and RCM skills in SE US summer precipitation simulations.

4.1 Data, models, and analysis methods

The research approach is through the evaluation of SE US summer precipitation simulated by the Phase 5 of the Coupled Model Intercomparison Project (CMIP5) models and the RCMs participated in the North American Regional Climate Change Assessment Program (NARCCAP). Furthermore, the CMIP5 models simulated NASH western ridge circulation are analyzed, and sensitivity experiments using Weather Research and Forecasting (WRF) model are performed to study the physical processes responsible for GCM and RCM skill, respectively.

4.1.1 Observational datasets

Observational precipitation used to evaluate CMIP5 models consists of three data sources covering the 1950-1999 period: NOAA's Prec/L (Chen *et al.* 2002), NOAA CPC

US unified precipitation (Higgins *et al.* 2000), and Global Precipitation Climatology Centre (GPCC) monthly precipitation dataset (Rudolf *et al.* 2010). The three observational datasets highly consistent in terms of the climatology and the interannual variation of SE US summer precipitation (not shown), ensuring the reliability of precipitation reference metric for model evaluation.

We use atmospheric reanalysis to represent the observed large-scale circulation. This approximation is valid in this research domain, since current reanalysis datasets show considerable consistency in depicting summertime hydroclimate over the SE US (see Chapter 2) and the NASH circulation (Li *et al.* 2011). 850hPa geopotential height is used to characterize the NASH western ridge circulation (see Chapter 3). The 850hPa geopotential height is from seven reanalysis datasets (Table 4.1). Among them, the NCEP/NCAR and ERA-40 span relatively longer temporal period than those more up-to-date reanalysis products (Table 4.1). They are adopted to evaluate the performance of CMIP5 models in representing the observed "NASH western ridge – SE US summer precipitation" relationship in the past 60 years.

Table 4. 1: Reanalysis datasets used in this study

Datasets	Temporal Coverage	Horizontal Resolution	References
NCEP/NCAR	1948-present	2.5°×2.5°	Kalnay *et al.* 1996
ERA-40	1958-2002	2.5°×2.5°	Uppala *et al.* 2005
NCEP-R2	1979-present	2.5°×2.5°	Kanamitsu *et al.* 2002
JRA-25	1979-present	T106 Gaussian	Onogi *et al.* 2007
NARR	1979-present	32-km	Mesinger *et al.* 2006
ERI	1979-present	1.0°×1.0°	Dee *et al.* 2011
CFSR	1979-present	0.5°×0.5°	Saha *et al.* 2010

4.1.2 CMIP5 GCMs

In order to assess the capability of the "state-of-the-art" GCMs to simulate SE US summer precipitation and its observed relationship with the NASH western ridge circulation, JJA precipitation and 850hPa geopotential height simulated by 24 CMIP5 GCMs (Table 4.2) in Historical run (1950-1999) are analyzed. The Historical run represents the current climate and is driven by observed atmospheric composition changes and other forcing agents. Time-evolving land cover changes are considered for the first time in CMIP5 models (Taylor *et al.* 2012). Among CMIP5 long-term experiment, the Historical run is the core and is given higher priority by each modeling center (Taylor *et al.* 2012). Thus, larger output sample size will be available to ensure the robustness of the analysis results.

Table 4. 2: CMIP5 GCMs used in this study

Model	Resolution (Lat. × Lon., Level)	Ensemble Members	
		Historical	RCP4.5
ACCESS1-0	144 ×192L38	1	1
BCC-CSM1-1	T42L26	3	1
CanESM2	T63L35	5	5
CCSM4	192 × 228L26	6	5
CNRM-CM5	T127L32	10	1
CSIRO-Mk3.6.0	T63L18	10	10
FGOALS-g2	128 × 60L26	5	1
FGOALS-s2	128 × 108L26	3	3
GFDL-CM3	90 × 144L48	3	1
GFDL-ESM2G	90 × 144L24	3	1
GFDL-ESM2M	90 × 144L24	3	1
GISS-E2-R	89 × 144L40	6	5
HadCM3	73 × 96L19	10	2050-2099 N/A
HadGEM2-CC	144 × 192L60	3	1
HadGEM2-ES	144 × 192L38	4	4
INM-CM4	120 × 180L21	1	1
IPSL-CM5A-LR	95 × 96L39	5	4
IPSL-CM5A-MR	143 × 144L39	1	1
MIROC4h	T213L56	3	2050-2099 N/A
MIROC5	T85L40	4	3
MIROC-ESM	T42L80	3	1
MPI-ESM-LR	T63L47	3	3
MRI-CGCM3	T159L48	5	1
NorESM1-M	96 × 144L26	2	1

Usually, different GCMs have different base state circulations. Thus, the absolute value of 850hPa geopotential height spread among models. To avoid such a spread in the simulated NASH western ridge circulation, we adjust the western boundary of

NASH to the geopotential height isoline straddling 86°W, where the climatological 1560-gpm isoline is located in NCEP/NCAR and ERA-40 (Li *et al.* 2011). The intersecting point of the modeled western boundary with the identified ridge-line (Chapter 3) is calculated to study the movement of the NASH western ridge as simulated by each CMIP5 model.

Multi-model ensemble (MME) and multiple-run ensemble methods are applied in this study. The MME emphasizes precipitation changes due to climate forcing and deemphasizes differences in models' dynamic cores and parameterization schemes (Gleckler *et al.* 2008). Of the 24 CMIP5 models, 21 provide multiple runs for Historical experiments (Table 4.2). For these 21 models, multiple-run ensemble is applied by drawing 50-yr subsamples from the original multiple-run sample sets. The subsampling avoids artificial weight added to any single model. The multiple-run sample set is sub-divided into 50 quantiles with cumulative probability monotonously increasing by 2% for each quantile from low to high quantiles. From this multiple run sample set, a 50-year sample is drawn and sub-divided into the same quantiles as the original sample set. This sub-sampling process was repeated 1000 times. The subsample with smallest quantile distance[1] from the original sample was chosen to represent this specific model's simulation of SE US summer precipitation. Compared with the variance of the original

[1] The quantile distance is defined as the Eulerian distance between the precipitation quantile vectors from subsample and the original sample: $D = \sqrt{\sum_{i=1}^{50} \left| q_{ai} - q_{bi} \right|^2}$, where q_{ai} is the i-th quantile precipitation rate in subsample, and q_{bi} is the i-th quantile precipitation rate from original sample.

sample, this subsampled precipitation shows high confidence in representing the precipitation variability as simulated by specific models.

4.1.3 NARCCAP RCMs and the WRF model

SE US summer precipitation simulated by the six RCMs participating in the NARCCAP (Mearns *et al.* 2009) are analyzed. We focus on the simulations driven by lateral boundary conditions from the NCEP-R2 (Kanamitsu *et al.* 2002), which are designed for the purpose of model evaluation (Mearns *et al.* 2012). The six RCMs are: the Canadian Regional Climate Model version 4 (CRCM), the Experimental Climate Prediction Center's Regional Spectral Model (ECP), the Hadley Centre Regional Model version 3 (HRM3), the fifth-generation Pennsylvania State University–NCAR Mesoscale Model (MM5), the Regional Climate Model version 3 (RCM3), and the Weather Research and Forecasting Model (WRF). The model domain covers the whole CONtiguous United States (CONUS) and Canada, and the horizontal resolution is 50 km (Mearns *et al.* 2009; Mearns *et al.* 2012).

The results obtained from the NARCCAP RCMs are verified by simulations using WRF model version 3.3 (Skamarock *et al.* 2008). Furthermore, sensitivity experiments are performed to study the processes and physical mechanisms responsible for RCM skills in simulating SE US summer precipitation. The WRF is a non-hydrostatic, terrain following eta-coordinate mesoscale modeling system, which has been widely used for regional weather and climate forecasting and research. The experiment domain is

configured over the CONUS, with a 36-km horizontal resolution. The lateral boundary is composed of a 1-point specified zone and a 4-point relaxation zone to smooth potential pseudo-disturbances caused by numerical calculation (Figure 4.1). The horizontal coordinates use the Lambert conformal conic projection with the standard parallels at 30°N and 60°N. The model consists of 38 vertical layers, and the top level is set to 50 hPa.

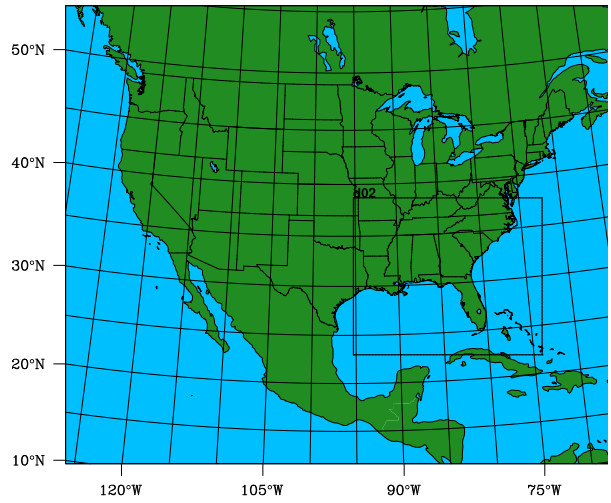

Figure 4. 1: Domain configuration for WRF experiments

The physical parameterization schemes used in this study include the Dudhia shortwave radiation (Dudhia 1989), Rapid Radiative Transfer Model (RRTM) longwave radiation (Mlawer *et al.* 1997), Thompson microphysics (Thompson *et al.* 2008), Yonsei Universtiy (YSU) planetary boundary layer physics (Noh *et al.* 2003), and Noah land surface model (Chen and Dudhia 2001). Four different cumulus schemes are compared in this study, because cumulus schemes are likely to introduce large uncertainties to the simulations of SE US summer precipitation (Bukovsky and Karoly 2009; Jankov *et al.*

2005; Li *et al.* 2014). The four cumulus schemes are Kain-Fritsch [K-F (Kain 2004)], Betts-Miller-Janjic [BMJ (Janjic 1994, 2000)], Grell-3 (Grell and Dévényi 2002) and Zhang-McFarlane (Zhang and McFarlane 1995) schemes, respectively.

NCEP-R2 is adopted to provide initial and boundary conditions for the simulations. In our analysis, simulations driven by NCEP-R2 data are compared with those driven by ERA-Interim (Dee *et al.* 2011). We find that the choice of driving reanalysis does not influence the summer rainfall simulation results in a discernible way (not shown). The 2001 summer is selected as the simulation period, according to a pattern recognition algorithm which synthesizes three score metrics to identify a summer precipitation case representative of the rainfall climatology over the SE US (Appendix A). The WRF simulation is initialized on May 1, 2001 and run through August 31, 2001. The first month is discarded as spin-up.

4.2 GCM simulations of SE US summer precipitation

4.2.1 SE US summer precipitation as simulated by CMIP5 models in current climate (1950-1999)

SE US summer precipitation as simulated by CMIP5 models in Historical runs is compared with observations (Figure 4.2). Generally, the spatial pattern of simulated summertime precipitation climatology shows considerable discrepancy from observations (Figure 4.2). Three observation datasets consistently show a higher precipitation along the coastal regions associated with localized land-sea diabatic heating contrast (Wu *et al.* 2009). The precipitation rate decreases inland with a gradient

in the northwest-southeast orientation (Figure 4.2a). Compared with observations, the MME of 24 CMIP5 models show a higher precipitation rate in the interior domain rather than along the coastal regions (Figure 4.2b). In other words, CMIP5 models generally overestimate precipitation inland, but underestimate precipitation over the coastal regions (Figure 4.2c).

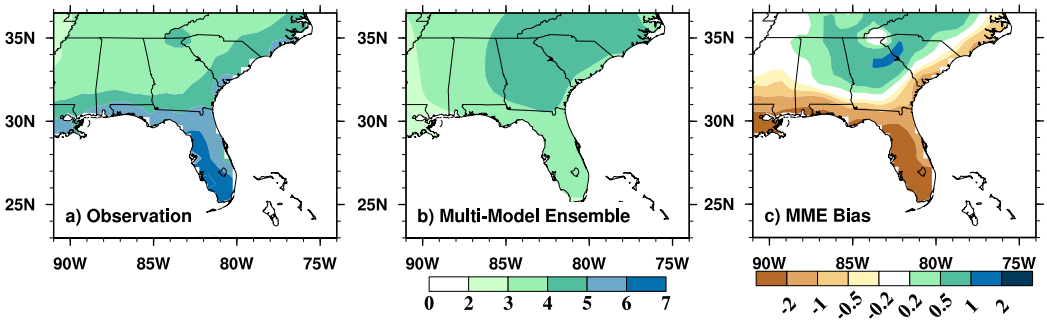

Figure 4. 2: Summer precipitation climatology (shaded, mm day^{-1}) over the SE US calculated as a) the ensemble of Prec/L, NOAA CPC unified US precipitation, and GPCC data; b) multi-model ensemble (MME) of Historical run; and c) MME bias of summer precipitation.

Furthermore, the bias pattern in MME is also noticed in about 85% of the CMIP5 models analyzed in this study (Figure 4.3). The mismatch between CMIP5 model simulated precipitation pattern and the observations probably result from the relatively coarse resolution of CMIP5 GCMs (~100km horizontal resolution on average), who cannot fully resolve the complicated rainfall generation processes over the SE US, including the topographic forcing of Appalachian Mountains and the land-sea breeze. Thus, the representation of the spatially heterogeneous features of SE US summer precipitation by CMIP5 models is problematic and unreliable.

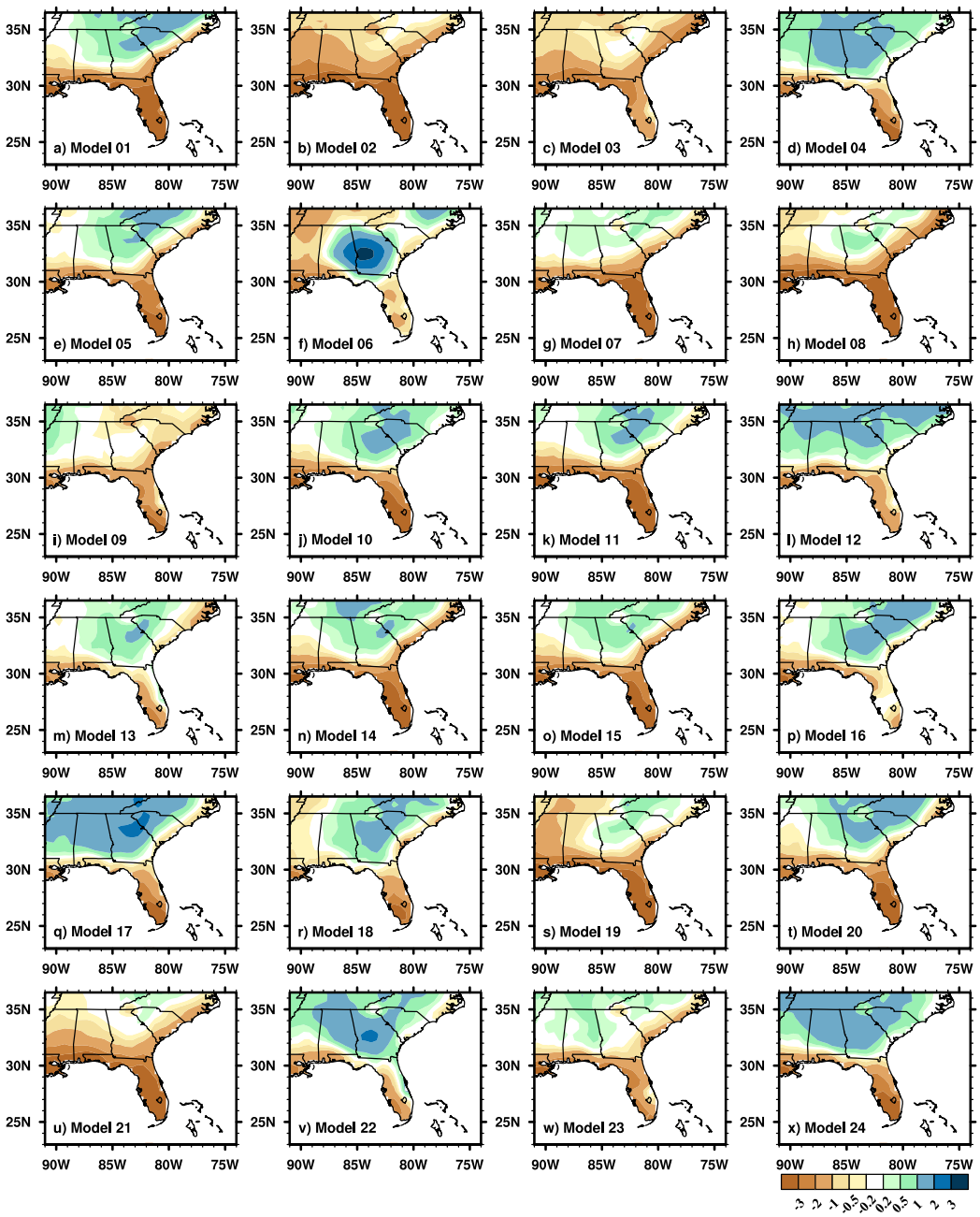

Figure 4. 3: Bias of summer precipitation (shaded, unit: mm day^{-1}) as simulated by each individual CMIP5 models (Historical run, 1950-1999).

Despite their coarse resolution to reliably capture the spatial distribution of summer precipitation over the SE US (Figure 4.3), the CMIP5 models reasonably simulated the

leading mode of SE US summer precipitation at interannual scale. According to the Empirical Orthogonal Function (EOF) analysis applied to observational data, the leading mode of SE US summer precipitation is characterized by a spatially uniform pattern. This first EOF explains 38% of summer precipitation variance over the SE US (Figure 4.4a). This dominant mode of precipitation is reasonably simulated by CMIP5 models (Figure 4.4b). The ensemble of first EOF mode in CMIP5 model simulations shows remarkable similarity with observations, in terms of both the magnitude of mode variability and the locations of local maxima (Figure 4.4b). Furthermore, each individual model is skillful in simulating this leading EOF mode (Figure 4.4c-z), despite the differences in model resolution, configuration and complexity, etc.

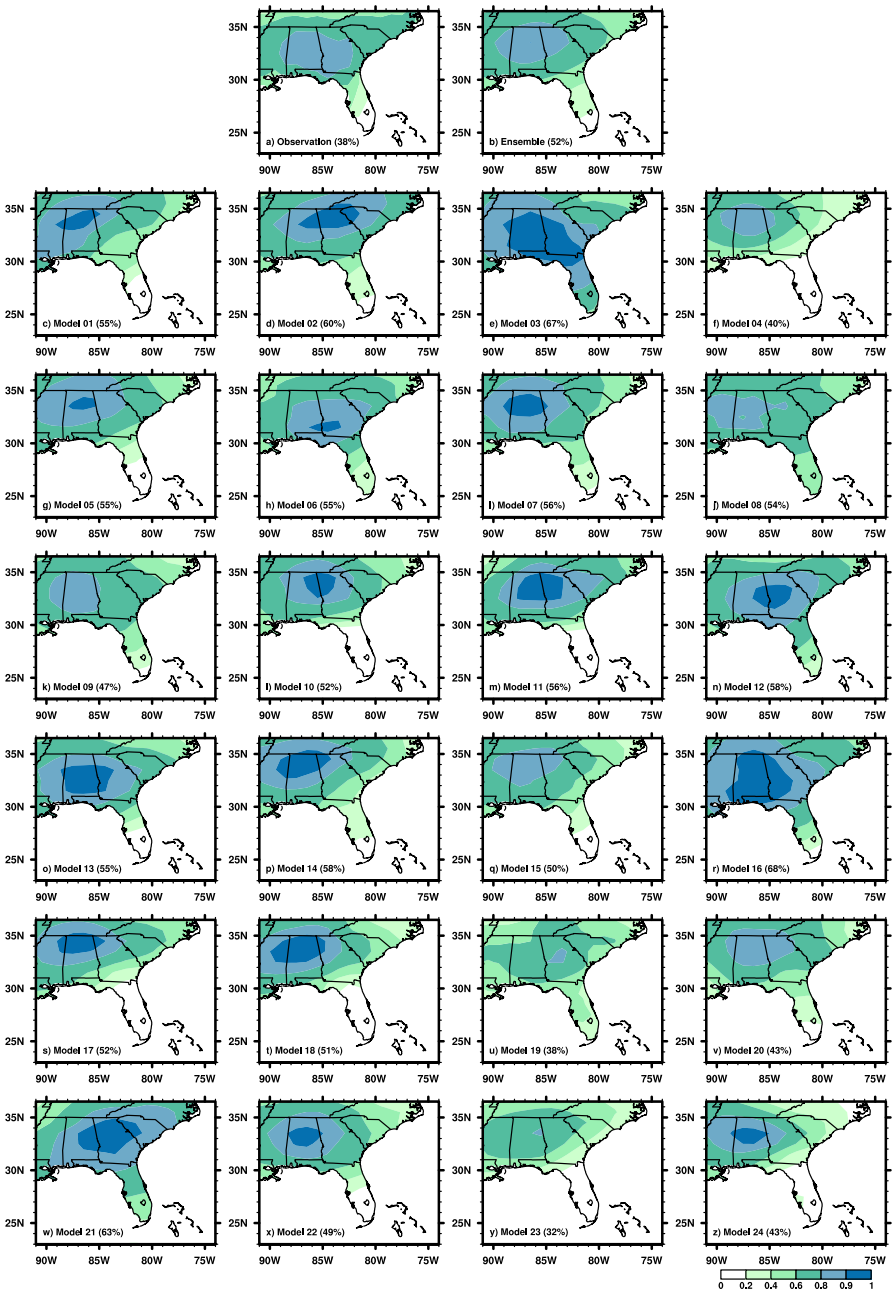

Figure 4. 4: First EOF mode of SE US (25°N-36.5°N, 91°W-76°W) summer precipitation derived from a) observations; b) the ensemble of CMIP5 model Historical run; and c) – z) individual models. Total variance explained by the first EOF in each model is listed. The spatial patterns are shown as the correlation between precipitation at each grid point and the corresponding PC1 time series.

Corresponding to this homogenous spatial mode (Figure 4.4), the temporal variation of the first EOF mode (as represented by the first Principle Component (PC1)) covaries with the areal-averaged precipitation. The R^2 between PC1 and areal-averaged precipitation reaches 0.95 (0.96) in observations (CMIP5 models on average), indicating that areal-averaged precipitation can reasonably characterize the interannual variation of SE US summer precipitation in both observations and CMIP5 models (Figure 4.5). Most importantly, the areal average methods de-emphasize the spatial heterogeneity of SE US summer precipitation which is not well simulated by CMIP5 models (Figures. 4.2 and 4.3) and thus makes the simulated temporal variation of summer precipitation comparable with that observed.

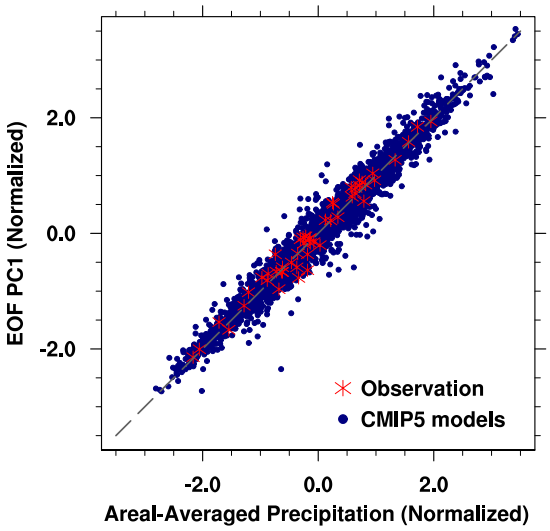

Figure 4. 5: Area-averaged SE US summer precipitation versus EOF PC1 according to observation (red asterisks) and CMIP5 model simulation (blue dots). The gray dash line denotes $y:x=1:1$. Both the precipitation and PC1 time series have been normalized.

Due to the limitations of CMIP5 models in simulating the spatial distributions of SE US summer precipitation (Figures 4.2 and 4.3), this study focuses on the variability of areal-averaged SE US summer precipitation. The gauge data suggests that the maximum likelihood estimator (MLE) of the precipitation standard deviation is 0.65 mm day^{-1} for the period of 1950-1999, with the 95% confidence interval (CI) [0.55 0.73]. These statistics provide an evaluation metric to assess the model simulation of SE US summer precipitation variability.

Figure 4.6 shows SE US summer precipitation variability simulated by CMIP5 models (Historical run) and the comparison of model results with observations. Among 24 CMIP5 models, 50% of the models simulate the standard deviation of summer precipitation within the 95% CI, suggesting that half of the models (Group 1 (G1) models) reasonably capture the precipitation variability in the 1950-1999. On the other hand, 37.5% (12.5%) of the models underestimate (overestimate) the summer precipitation variability compared to observations; these models are categorized as Group 2 (G2) models which need certain improvement (Figure 4.6a).

On average, the ensemble of CMIP5 model simulated SE US summer precipitation variability is within the 95% CI of the observed variability, although the exact value is about 10% below the MLE of observations. In addition, we compared the precipitation variability in Earth System Models (ESMs) to that in coupled Atmosphere-Ocean GCMs (AOGCMs) (Hibbard *et al.* 2007; Meehl and Hibbard 2007). The ESM ensemble shows

summer precipitation variability closer to observations than the AOGCM ensemble (Figure 4.6b). This improvement may be attributed to a more realistic representation of ecosystem and its interaction with atmosphere, indicating an important role of biosphere dynamics in SE US regional hydrology (Peters *et al.* 2003; Stoy *et al.* 2006). However, since the sample size of ESMs is relatively small and certain inter-model spread exists, it is still hard to ascertain that ESMs outperform AOGCMs in simulating SE US summer precipitation variability at current stage.

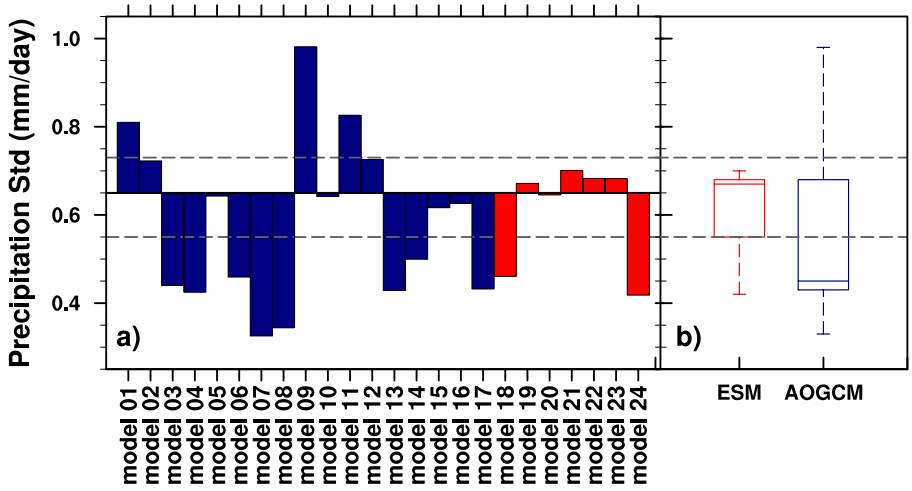

Figure 4. 6: Standard deviation of SE US summer precipitation simulated by the 24 CMIP5 models under Historical scenarios and their comparison with observations: a) the red (blue) bar denote the simulation by ESMs (AOGCMs); b) the boxplot summarizing the simulation of summer precipitation variability by ESMs (red box) and AOGCMs (blue box). In the boxplot, the lower and upper bar represents the minimum and maximum value of the standard deviation from model simulation; the lower and upper bound of the box is the 25% and 75% quatile of the standard deviation; and the bar in the middle of the box is the median of the modeled standard deviation. In a) and b), the solid line is the MLE of SE US summer precipitation standard deviation derived from observations and the dashed lines are the upper and lower bounds of the 95% confidence interval of the MLE standard deviation.

4.2.2 NASH circulation and GCM simulation skill of SE US summer precipitation

CMIP5 models diverge in their simulation skill of SE US summer precipitation variability. Understanding the factors critical to the simulation skills of SE US summer precipitation variability is thus important to improve the GCM performance in representing SE US summer climate. In this study, we assess the capability of CMIP5 models in simulation the "NASH western ridge – SE US summer precipitation" relationship, a first order dynamic control on SE US summer precipitation (Wuebbles *et al.* 2013).

As shown in Figure 4.7 a-d, G1 models reasonably capture the relationship between SE US summer precipitation and the NASH western ridge. On average, G1 models simulate a drier (wetter) summer in the SE US during NW (SW) years (Figure 4.7a-b); whereas summer precipitation shows no significant anomalies during NE and SE summers (Figure 4.7c-d). Although the decrease in summer precipitation during NW years is about 0.2 mm day^{-1} less than observations, the key features of the observed relationship (Figure 3.3) are well simulated by G1 models. The magnitude of deficit and excessive precipitation during NW and SW years far exceeds inter-model rainfall spread, indicating a high agreement of signal among G1 models (Figure 4.7a-d).

In contrast, G2 model simulation of the "NASH western ridge – SE US summer precipitation" relationship differs substaintially from observations (Figure 4.7e~h). Generally, G2 models fail to simulate wetter summers when the ridge is in SW position

(Figure 4.7f). During SW years, summer precipitation remains close to its climatology; the weak wet anomalies along the North and South Carolina border are not statistically significant (Figure 4.6f). In a SE year, however, G2 models tend to simulate wet summers over the SE US, especially in Florida, Southern Georgia and Alabama (Figure 4.6h). Although G2 models generally suggest a below normal summer precipitation during NW years, the dry anomalies concentrate in the southern part of SE US, instead of the entire region as suggested by observations (Figure 3.3a and e); and the magnitude is weaker than that of observations.

Overall, the "NASH western ridge – SE US summer precipitation" relationship is not well captured by G2 models (Figure 4.7e-h). Specifically, in G2 models, the westward extension of the western ridge does not show enhanced impact on SE US summer precipitation, especially in SW years. The inability of G2 models to simulate this circulation control on SE US summer precipitation might cause their biases in the summer precipitation variability. However, why G2 models cannot simulate the "NASH western ridge – SE US summer precipitation" relationship needs further investigation.

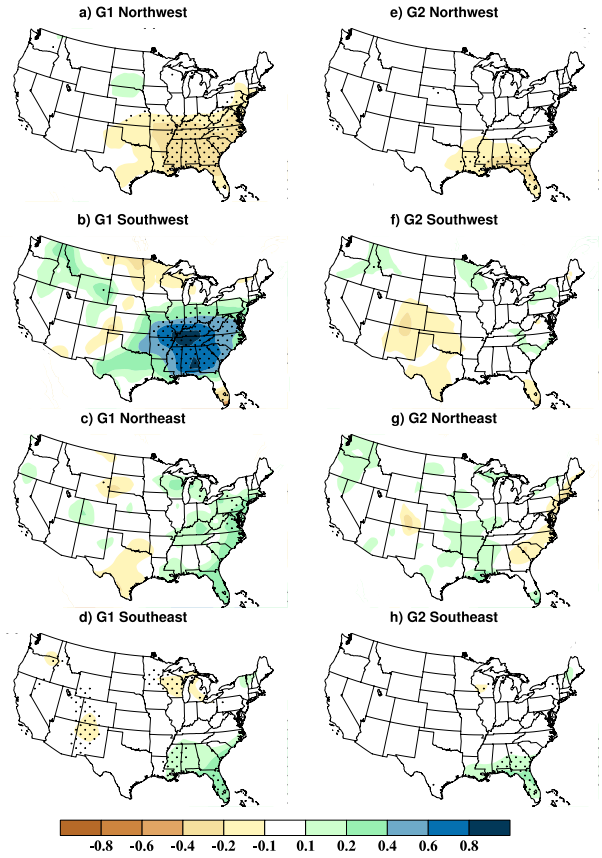

Figure 4. 7: Composite of US summer precipitation anomalies (shaded; mm day^{-1}) based upon 850hPa NASH western ridge position: a) and e) Northwest; b) and f) Southwest; c) and g) Northeast; and d) and h) Southeast ridging. The a) – d) are the composite results using the western ridge position derived from G1 models; and the e) – h) are those derived form G2 models. The stippled areas mark the simulated summer precipitation anomalies exceeding one inter-model standard deviation among each group models. Here, G1 (G2) models are those showing relatively high (low) skill in simulating SE US summer precipitation variability.

To ensure that the ensemble results in Figure 4.7 are not dominated by any single model, the consistency of precipitation signal among models in the two groups is assessed, respectively. Generally, G1 models show higher consistency in the simulated precipitation anomaly pattern than G2 models. Almost all G1 models simulate the increase (decrease) in SE US summer precipitation with ridge in SW (NW) position,

suggesting such simulation skills are common features among G1 models (Fig. 4.6a-d), although the magnitude of precipitation anomalies differ slightly among G1 models. In contrast, G2 models largely spread in simulating the "NASH western ridge – SE US summer precipitation" relationship. For example, about 50% of G2 models indicate a decrease in SE US summer precipitation when the western ridge is in SW position, while the other 50% suggest the opposite (not shown).

We further compared the differences in the simulated SE US summer precipitation variability between models that can capture the "NASH western ridge – SE US summer precipitation" and models that cannot. Models capable of representing this ridge-rainfall relationship simulate SE US summer precipitation variability within the 95% CI of the observed precipitation variability. The averaged precipitation standard deviation obtained from these models is 0.67 mm day^{-1} close to the MLE of observations (0.65 mm day^{-1}). In contrast, models misrepresenting the ridge-rainfall relationship generally underestimate the summer precipitation variability, which results in the simulated precipitation variability outside the 95% CI of observations (not shown).

Thus, the results suggest that the simulation skills of SE US summer precipitation variability could be attributed to the representation of the "NASH western ridge – SE US summer precipitation" relationship. Such a relationship is well simulated by G1 models (Figure 4.7a-d), but is not captured by G2 models (Figure. 4.7e-h). The lack of such a relationship in G2 models' simulation largely contributes to their bias in simulating SE

US summer precipitation variability. Our results thus suggest that improving the simulation of the "NASH western ridge – SE US summer precipitation" relationship in G2 models might help to correct their simulation bias.

4.3 RCM simulations of SE US summer precipitation

Evaluation of CMIP5 model simulated SE US summer precipitation indicates that the "state-of-the-art" GCMs are able to simulate the large-scale mode of SE US summer precipitation (Figure 4.4). However, due to their coarse horizontal resolutions (~100 km), the GCMs fail to capture the spatial distribution of SE US summer precipitation (Figures 4.2 and 4.3). Thus, dynamical downscaling with RCMs that have sophisticated structure and physics could be an effective way to better represent SE US summer precipitation (Boberg *et al.* 2010; Rauscher *et al.* 2010).

4.3.1 SE US summer precipitation as simulated by NARCCAP RCMs

The skills of current RCMs in simulating the SE US summer precipitation are evaluated by analyzing the output of all six RCMs participating in the NARCCAP. Figure 4.8a shows the uncertainty range of the RCMs in simulating summer precipitation climatology (1980-2004) over the CONUS domain. Here, the uncertainty range is defined as the difference between the highest and lowest precipitation rate among the six RCMs. Larger difference at each grid point indicates higher uncertainties of RCM skills in simulating the summer precipitation.

Simulated summer precipitation by the NARCCAP RCMs show a much larger spread over the SE US compared to other regions in the CONUS (Figure 4.8a). The uncertainty exceeds 3 mm day^{-1} for the majority of the grid cells (>60%) in the Southeast, with more than 5 mm day^{-1} over Florida (Figure 4.8a). The uncertainty range is about 2 mm day^{-1} higher than that over the Northeastern US and the Pacific Northwest (Figure 4.8a).

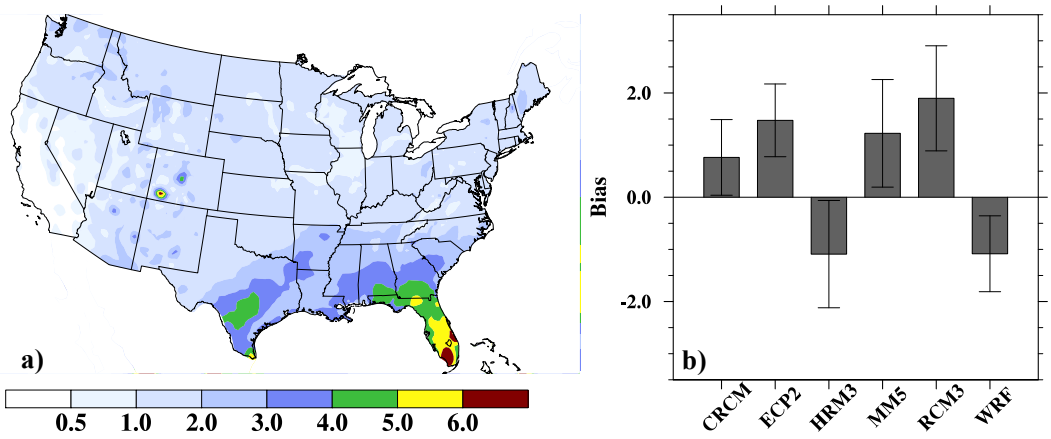

Figure 4. 8: a) The spread of RCM simulated US summer (JJA) precipitation climatology (1980-2004) as simulated by 6 NARCCAP RCMs driven by NCEP-2 reanalysis; b) bias (bars) in SE US areal-averaged precipitation in each of the 6 RCMs. The error bar represents the upper and lower bound of the bias as defined by one standard deviation of interannual variation of precipitation.

The high uncertainty (spread) in the RCM skills in simulating SE US summer precipitation is also reflected in domain averaged summer precipitation. Among the six RCMs, four models (CRCM, ECP, MM5, and RCM3) produce wet biases while the other two generate dry biases (HRM3 and WRF; Figure 4.8b). Both the dry and wet biases exceed one standard deviation of the observed summer precipitation over the SE US, which are statistically significant at $\alpha = 0.01$ level (student t-test).

The above analysis suggests that the RCMs generate a large spread and a large bias in SE US summer precipitation simulations, consistent with individual RCM studies such as Chen *et al.* (2003), Liang *et al.* (2006), and Mearns *et al.* (2012). The high uncertainty and large bias in RCM simulated SE US summer precipitation hampers its application in climate prediction and water management for this fast developing region. Thus, understanding what causes the RCM spread in SE US summer precipitation simulation and exploring potential solutions to reducing the bias could help improve the reliability of climate prediction skills over this region.

4.3.2 Causes of SE US summer precipitation bias in RCMs: case study using WRF model

Simulations of precipitation usually depend on two categories of factors: large-scale circulation pattern and the subgrid scale parameterizations [e.g. Arakawa et al. 2004]. In terms of the simulations of SE US summer precipitation, on the one hand, the large-scale NASH circulation primarily controls SE US summer precipitation at the seasonal scale (Li *et al.* 2012a; Li *et al.* 2011; Wuebbles *et al.* 2013). Furthermore, the analysis of CMIP5 GCMs shows that GCM skills in simulating SE US summer precipitation is directly related to their ability in representing the NASH circulation (Section 4.2). On the other hand, summer rainfall simulations over the SE US are sensitive to the choices of physical parameterization schemes, especially the cumulus schemes (Bukovsky and Karoly 2009; Jankov *et al.* 2005; Li *et al.* 2014).

Here, we will use the WRF simulations of CONUS 2001 summer precipitation to explore 1) whether the biases in SE US summer precipitation is first related to the errors in large-scale circulation patterns and thus a selection of the cumulus schemes cannot effectively improve the simulations; 2) or on the contrary, the choice of cumulus schemes does meaningfully improve the simulations of SE US summer precipitation.

The WRF simulated 2001 summer precipitation over the CONUS are shown in Figure 4.9. The precipitation simulated with the four different cumulus schemes is ensembled so that the uncertainties due to cumulus schemes are minimized. According to Figure 4.9, the WRF model reasonably captures the spatial pattern of summer rainfall over the SE US (Figure 4.9a and b), with a high pattern correlation coefficient (0.60) with observation. Specifically, the observed summer precipitation shows a Southeast-Northwest oriented gradient across the SE US, with the highest precipitation rate occurring over the coastal regions (Higgins *et al.* 2007; Wang *et al.* 2010). Compared to the CMIP5 GCMs, the WRF model substantially improves the representation of the spatial pattern of SE US summer precipitation (Figure 4.2).

In contrast to the reasonable simulation of rainfall spatial pattern, the WRF substantially underestimates the intensity of summer precipitation over the SE US. On average, the WRF simulations result in a net dry bias of 1.3 mm day^{-1} over the terrestrial areas within the SE US domain (25°N~36.5°N, 91°W~76°W).

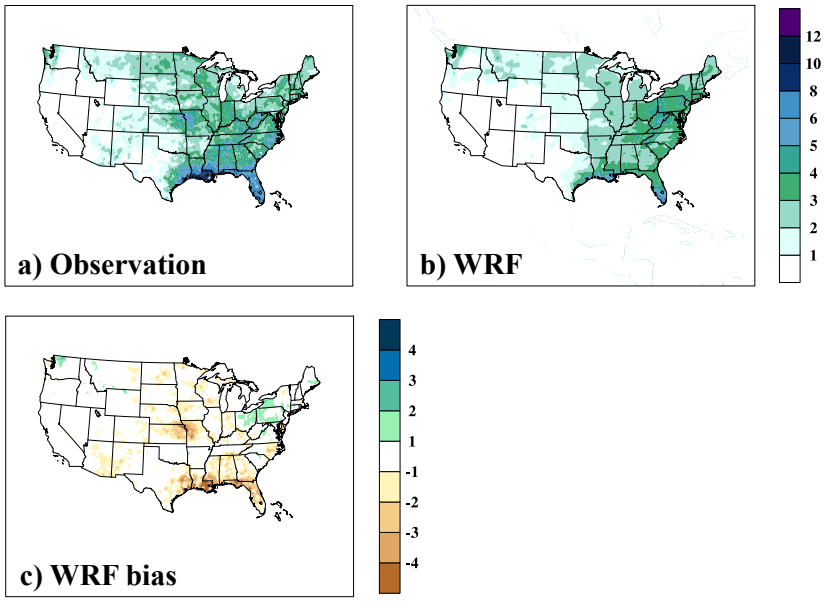

Figure 4. 9: 2001 US summer (JJA) precipitation (shaded, unit: mm day^{-1}): a) observations; and b) WRF; c) bias of summer precipitation (shaded, unit: mm day^{-1}) in WRF simulations.

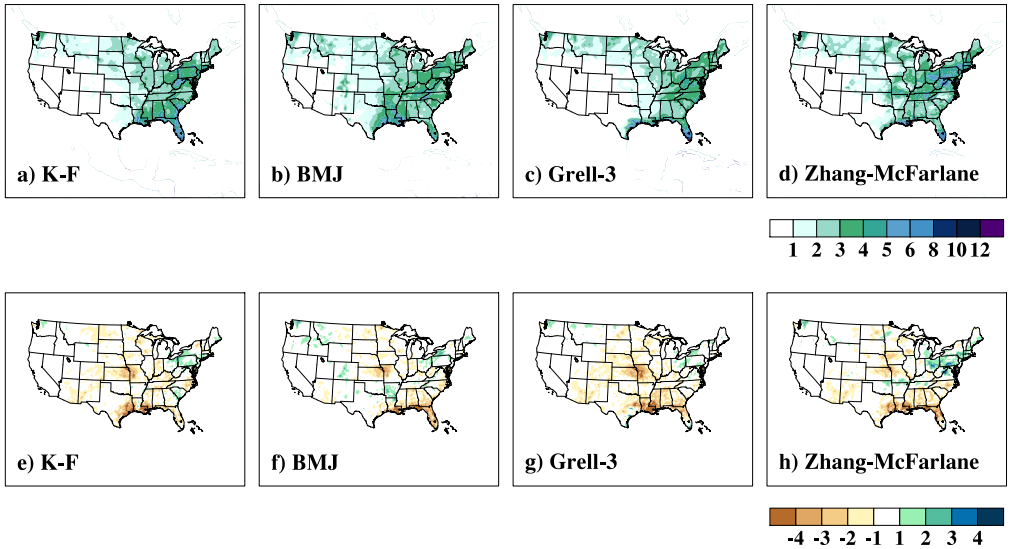

Figure 4. 10: 2001 US summer (JJA) precipitation (shaded, unit: mm day^{-1}) as simulated by WRF with different cumulus schemes: a) K-F; b) BMJ; c) Grell-3; and d) Zhang-McFarlane; e)-h) are the precipitation bias simulated by each cumulus schemes compared with observations.

We further compare the precipitation simulated with the different cumulus schemes. The dry bias over the SE US exists among these four schemes (Figure 4.10e~h), although the spatial distributions of precipitation differ slightly (Figure 4.10). Averaged over the SE US, the net biases in precipitation range from -0.92 mm day^{-1} (K-F scheme; Figure 4.10e) to -1.52 mm day^{-1} (Zhang-McFarlane scheme; Figure 4.10h), which are all statistically significant at $\alpha = 0.01$ level (student *t*-test).

The above analysis suggests that the WRF simulated dry bias is less likely caused by the choice of the cumulus schemes. Furthermore, such a dry bias has also been noticed in individual WRF simulations performed in previous studies, where different physical parameterization schemes are implemented (Bowden *et al.* 2013; Mearns *et al.* 2012; Sobolowski and Pavelsky 2012). Thus, it indicates that the WRF simulated SE US dry biases may not be caused only by the physical parameterization schemes.

According to the analysis of WRF simulated large-scale circulation, the dry bias is more likely caused by the errors in the simulated NASH circulation. The "NASH western ridge – SE US summer precipitation" relationship indicates that the northwestward positioning of the NASH western ridge tends to cause dry summers over the SE US (Figure 3.3a and e). Consistent with this relationship, the WRF dry bias in SE US summer precipitation concurs with an erroneously northwestward positioning of the NASH western ridge. The ensemble of the seven reanalysis datasets (Table 4.1) indicates that the NASH western ridge is located over the Gulf of Mexico, about 87°W

and 27°N in the summer of 2001 (Figure 4.11a). However, the modeled ridge extends northwestward into Texas (around 93°W and 32°N, Figure 4.11b), more than 7 degrees northwest compared to the observed ridge location (Figure 4.11a).

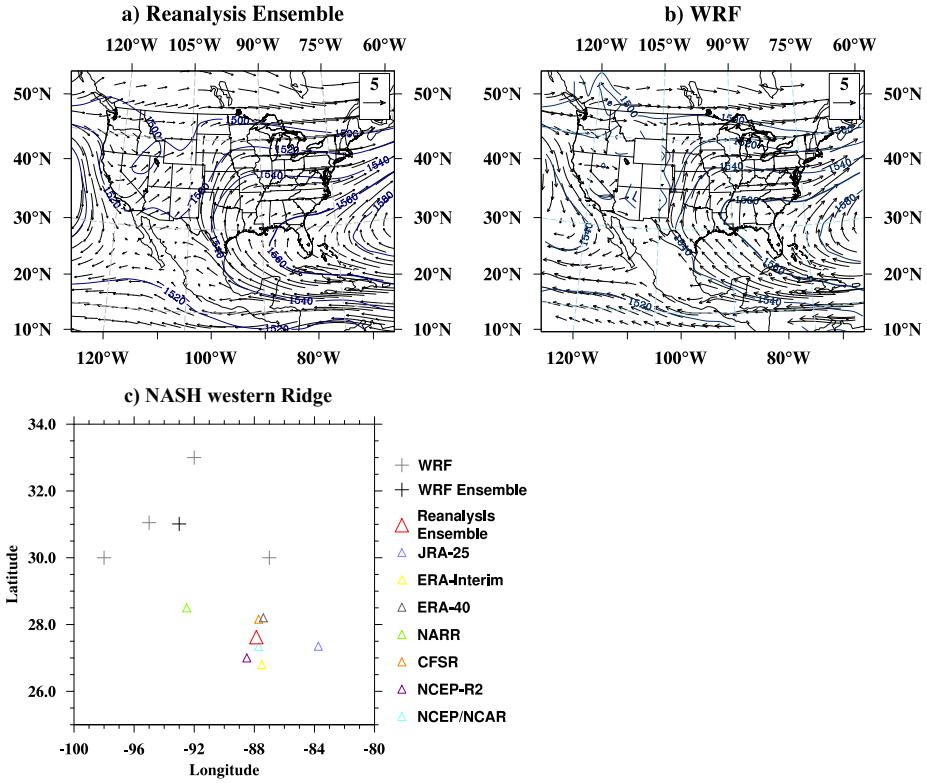

Figure 4. 11: 2001 JJA 850hPa geopotential height (contour, unit: gpm) and wind (vector, unit: m s^{-1}) in a) the ensemble of seven reanalysis datasets, and b) the WRF simulation. The contour interval is 20-gpm, and the bold curves are 1560-gpm isolines, which are used to represent the NASH western ridge. The location of the NASH western ridge in 2001 summer as calculated from each of the seven reanalysis datasets (upper triangles) and the four WRF simulations (gray crosses) is shown in c). The red upper triangle represents the ensemble of 7 reanalysis datasets; while the black cross represents the average of 4 WRF simulations.

Compared with that calculated using each of the seven reanalysis datasets, the WRF simulated ridge is outside the uncertainty range of the reanalysis datasets (Figure 4.11c). The ridge locations simulated by each individual cumulus scheme differ to some extent.

However, all of them are located northwest to the reanalysis ensemble (Figure 4.11c). The multivariate-paired Hotelling's t-square test[2] (Hoetlling 1931) suggests that the erroneously northwestward extension of the NASH western ridge in the WRF simulation is statistically significant at $\alpha = 0.0001$ level.

Corresponding to the biased northwestward location of the NASH western ridge, anticyclonic circulation along the ridge extends further into the US continent (Figure 4.11b). Consequently, the simulated southerly wind over the SE US weakens due to the erroneous northerly wind in the east portion of the anticyclone (Figure 4.11b). The weakened southerly wind over the SE US transports less moisture from the tropical Atlantic into the SE US, resulting in the dry bias in the simulated summer rainfall (Chapter 2).

4.3.3 NASH circulation dynamics and its contribution to SE US summer precipitation bias in WRF

The WRF simulations of 2001 summer climate over the CONUS indicates that the dry bias in SE US summer precipitation is most likely caused by the inaccurately simulated NASH western ridge and associated circulation due to the erroneous distribution of zonal winds in the tropical oceans, i.e., errors in circulation dynamics.

[2] The null hypothesis for the Hotelling's t-square test is that the WRF simulated NASH western ridge does not differ significantly from that in reanalysis datasets. According to the test, the null hypothesis can be rejected with a 99.99% confidence level, suggesting that the erroneous northwestward extension of the ridge is significant.

Thus, an improved simulation of large-scale circulation (especially the NASH western ridge) could potentially reduce the RCM bias in SE US summer precipitation.

To verify the importance of circulation dynamics in generating the SE US summer precipitation bias and to assess the potential improvement in precipitation simulation from an improved large-scale circulation, two sets of WRF experiments utilizing the FDDA are performed. The FDDA, i.e. interior grid nudging technique, continuously nudges the WRF simulated thermodynamic and dynamic variables towards the driving reanalysis datasets during the simulation (Stauffer and Seaman 1990). The FDDA has been widely applied in regional climate downscaling and has significantly improved climate downscaling skills over the US (Bowden *et al.* 2013; Lo *et al.* 2008; Otte *et al.* 2012). In this analysis, however, the application of the FDDA is not for the purpose of improving precipitation simulation skills but rather for identifying the potential sources of RCM skills in SE US summer precipitation.

The two sets of FDDA experiments are designed as follows: thermodynamic FDDA and dynamic FDDA. In the thermodynamic FDDA experiment, the temperature and specific humidity are nudged towards NCEP-R2 at each 6-hr interval during the simulation, while the wind fields are generated by WRF. In the dynamic FDDA experiment, the WRF simulated three-dimensional wind fields are nudged while the temperature and specific humidity are not. The previous experiment without an FDDA is defined as the control experiment. We run both thermodynamic and dynamic FDDA

with the four different cumulus schemes as in the control experiment. The improvement of the simulated precipitation in thermodynamic (dynamic) FDDA is attributed to the correction of atmospheric thermodynamic (dynamic) structures. Thus, by comparing the simulated precipitation in thermodynamic and dynamic FDDA with that from the control experiment, the relative importance of thermodynamic and dynamic contribution to SE US dry bias can be compared (Li *et al.* 2013b; Seager *et al.* 2010).

Figure 4.12 shows the CONUS JJA precipitation in the FDDA experiment. By correcting the WRF simulated circulation fields, the dynamic FDDA experiment substantially reduces the bias in SE US summer precipitation. In the dynamic FDDA experiment, summer precipitation increases to about 5 mm/day over the SE US domain. The domain-averaged bias is reduced to -0.3 mm day^{-1}, indicating that about 80% of the original dry bias in control experiment has been corrected (Figure 4.12a and c). Furthermore, the spatial distribution of precipitation, especially the southeast-northwest oriented gradient, is also reasonably simulated in the dynamic FDDA (Figure 4.12a). Thus, the dynamic FDDA experiment further verifies that the errors in wind fields generated during the WRF simulations are responsible for the SE US dry bias in the control experiment.

To confirm that the improved simulation of precipitation in the dynamic FDDA experiment results more from circulation dynamics, the effects of the thermodynamic FDDA are also compared. Generally, the thermodynamic FDDA does not improve the

simulation of SE US summer precipitation as significant as the dynamic FDDA when compared to the control experiment and observations. Specifically, in the thermodynamic FDDA experiment, the SE US dry bias is not meaningfully reduced (Figure 4.12b and d). The areal-averaged rainfall bias reaches -2.0 mm day^{-1} in the thermodynamic FDDA experiment, compared to the bias of -1.3 mm day^{-1} in the control experiment. In addition, the rainfall amount decreases over the coastal regions, and the spatial gradient of rainfall further weakens (Figure 4.12b). Thus, unlike the atmospheric dynamical fields, correcting the atmospheric thermodynamic fields is insufficient to generate a satisfactory skill in SE US summer precipitation simulations. More importantly, the comparison between the thermodynamic and dynamic FDDA experiments indicates that the improvements of the simulations due to the dynamic FDDA are most likely from direct dynamic contributions instead of indirect thermally driven circulation dynamics. In other words, if the thermally driven circulation (i.e. circulation component determined by atmospheric thermal structure) contributes significantly to rainfall simulation, the thermodynamic FDDA should generate similar corrective effects that the dynamic FDDA. However, since the thermodynamic FDDA fails to improve the precipitation simulations, it is the direct dynamic contributions in dynamic FDDA that provides the ultimate sources of simulation skills for SE US summer precipitation.

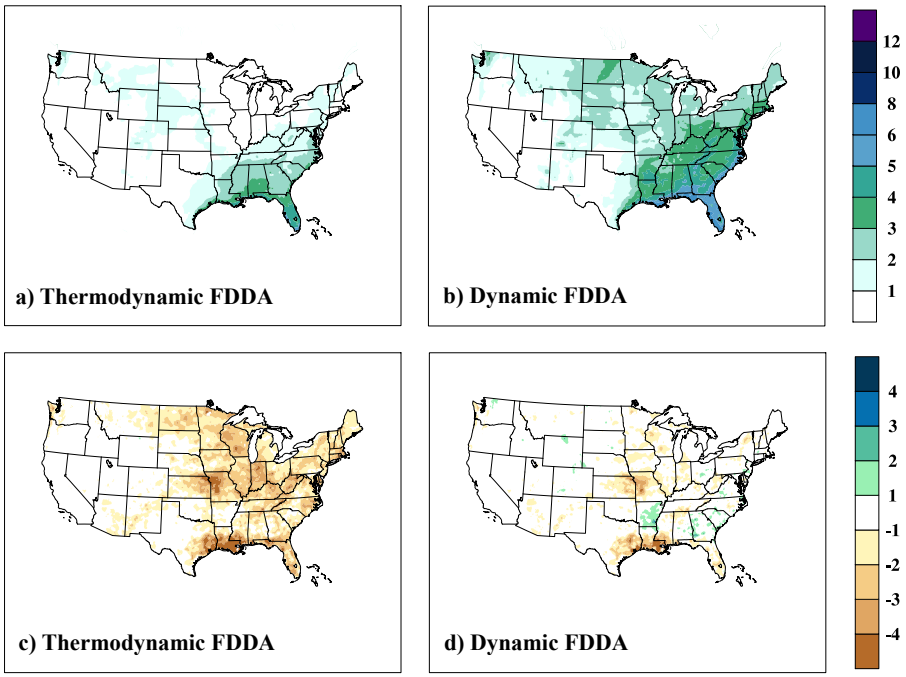

Figure 4. 12: 2001 JJA summer precipitation (shaded, unit: mm day^{-1}) as simulated in a) Thermodynamic FDDA, and b) Dynamic FDDA experiment; and the precipitation bias in c) Thermodynamic and d) dynamic FDDA. The results are shown as the average of the four cumulus schemes.

The experiments utilizing FDDA collectively suggest that the atmospheric dynamics plays a direct and predominant role in regulating SE US summer precipitation at seasonal scales. The results from FDDA experiment are consistent with the results of SE US summer precipitation based on the regional moisture budget (Chapter 2). Over the SE US, large-scale circulation contributes to more than 90% of the variance in moisture transport for SE US summer precipitation, whereas thermodynamic (temperature and specific humidity) contribution accounts for the less than 10% (Chapter 2). The observed characteristics of SE US hydrological cycle indicate that errors in large-scale circulation could easily translate into summer precipitation bias due to its active role in atmospheric

moisture balance. Thus, the distortion of the large-scale circulation along the NASH western ridge during the WRF simulation could result in the dry bias over the SE US (Figures. 4.9 and 4.10).

Overall, the FDDA experiments as well as the diagnostic analysis suggest that the WRF simulated dry bias in SE US summer precipitation probably originates from errors in modeled large-scale circulation. Thus, a better representation of large-scale dynamics, especially that associated with the NASH western ridge circulation, likely improve the WRF performance in simulation summertime climate over the SE US.

4.4 Summary and Conclusions

In this study, the skill of the state-of-the-art GCMs and RCMs in simulating the variability of SE US summer precipitation in current climate is evaluated. Furthermore, the role of the NASH circulation in determining such a skill is investigated.

Compared with observations, most CMIP5 GCMs cannot simulate the spatially heterogeneous features of SE US summer precipitation (Figures 4.2 and 4.3), due to their relatively coarse horizontal resolution (~100km). However, CMIP5 models reasonably capture the leading EOF mode of the variation of SE US summer precipitation (Figure 4.4). This leading EOF mode is characterized by a spatially uniform rainfall pattern and its variance can largely be explained by the areal averaged precipitation (Figure 4.5).

Thus, the simulated regional mean precipitation and its interannual variation pattern are comparable to observations.

Among 24 CMIP5 models analyzed in this study, 50% simulate a magnitude of SE US summer precipitation variability comparable to observations. In contrast, the other 50% fail to simulate summer precipitation variability well (Figure 4.6). According to model performance in SE US summer precipitation variability, CMIP5 models can be categorized into two groups: G1 models which reasonably simulate summer precipitation variability, and G2 models which need certain improvement.

The relatively high simulation skills of G1 models are attributable to their capability in representing the dynamical linkage between precipitation and NASH western ridge (Figure 4.7). When the western ridge is in NW (SW) position, the SE US tends to undergo abnormally dry (wet) summers; conversely, when the ridge is located in NE or SE position, SE US summer precipitation deviates little from its climatology. However, G2 models fail to capture this relationship and thus exhibit lower simulation skills (Figure 4.7). Thus, in order to achieve satisfactory skill in simulating SE US summer precipitation variability, the dynamical linkage between the NASH western ridge and SE US summer precipitation should be accurately represented by GCMs.

In addition to GCMs, RCMs are also evaluated in terms of their skills in SE US summer precipitation. RCMs generate values for predicting warm season climate over the SE US due to their relatively higher resolution and more sophisticated model physics.

However, the performance of RCMs in SE US summer precipitation has not yet been systematically evaluated, especially at process levels.

The simulations by RCMs participating in the NARCCAP are analyzed, and WRF simulations are performed for mechanistic study. The analysis of the NARCCAP output shows that the current RCMs simulate large bias and spreads in SE US summer precipitation (Figure 4.8a). Among them, the simulations by WRF model substantially underestimate the summer precipitation (Figure 4.8b).

By performing WRF simulations of CONUS 2001 summer climate, we find that the dry bias in WRF simulations may not be caused by the choice of cumulus schemes (Figures 4.9 and 4.10). Instead, the distortion of large-scale NASH western ridge circulation is likely the cause of the systematic dry bias in the WRF simulations, where the NASH western ridge is located erroneously northwestward (about 7 degrees) of the observed location as defined by the ensemble of seven reanalysis datasets (Figure 4.11). Such a ridge pattern deviates moisture transport away from the SE US in WRF simulations, resulting in the underestimated SE US summer precipitation.

The importance of NASH western ridge circulation in causing the WRF dry bias is further supported by two FDDA experiments: dynamic and thermodynamic FDDA. In the dynamic (thermodynamic) FDDA experiment, the WRF simulated 3-dimensional wind (temperature and specific humidity) is nudged toward NCEP R2 at each 6-hr interval. The differences in the simulated precipitation between dynamic

(thermodynamic) FDDA experiment and control experiment reflect the direct contribution of atmospheric dynamics (thermodynamics), respectively. According to the FDDA experiments, the correction of circulation dynamics can substantially reduce the bias in SE US summer precipitation while the correction of thermodynamics cannot significantly improve the rainfall simulation (Figure 4.12). Thus, the FDDA experiments further emphasize the importance to improve the representation of large-scale dynamics, especially the NASH western ridge, in RCM simulations.

Our analysis identifies the NASH western ridge circulation as an important factor in causing the RCM biases in simulating SE US summer precipitation. Furthermore, the correction of the NASH circulation dynamics through the FDDA does improve the simulation of SE US summer precipitation. Thus, the improvement in the simulation of the NASH circulation could potentially narrow the spread in RCM simulated SE US summer precipitation, and thus increase the reliability in the projection of SE US summer climate.

5. Improvements in WRF simulations of SE US summer precipitation: Physical parameterization and horizontal resolution

Evaluation of CMIP models shows that current generation of GCMs cannot well capture the spatial pattern of SE US summer precipitation (Chapter 4), attributable to their relatively low horizontal resolution (Taylor *et al.* 2012), which cannot fully resolve the highly heterogeneous rainfall generation processes within the domain (Baigorria *et al.* 2007; Li *et al.* 2013b; Stooksbury and Michaels 1991). Such a limitation can be largely overcome by the application of RCMs that have higher resolution and sophisticated structure and physics (Castro *et al.* 2005; Giorgi and Mearns 1999; Leung *et al.* 2003; Mearns *et al.* 2012).

Yet, satisfactory RCM simulation skill has not been achieved for the SE US (Bowden *et al.* 2013; Lo *et al.* 2008; Mearns *et al.* 2012; Walker and Diffenbaugh 2009). Warm-season precipitation as simulated by NARCCAP RCMs shows large uncertainties and biases over the SE US (Chapter 4), which limits the application of RCMs in simulating and predicting summer climate in the SE US. Thus, exploring the processes that constrain RCM simulation skills of SE US summer precipitation and understanding the underlying physical mechanisms are important to fulfilling the community's increasing need for reliable regional climate information.

The RCM simulation skills in regional climate usually depend on the initial conditions (ICs), lateral boundary conditions (LBCs), level of constraint toward driving

data, physical parameterizations, and model resolutions (Christensen *et al.* 2007; Feser *et al.* 2011; Foley 2010; Lo *et al.* 2008; Rummukainen 2010). The sensitivity of SE US summer rainfall to the configuration of LBCs has been emphasized in previous studies (Seth and Giorgi 1998; Xue *et al.* 2007). Configurations of LBCs can influence the simulations of the upper tropospheric jet, large-scale moisture transport pattern, and relative humidity field (Xue *et al.* 2007), which dynamically and thermodynamically affect SE US summer rainfall (Li *et al.* 2013b; Wang *et al.* 2010). Most importantly, configurations of LBC impact the RCM simulation of large-scale NASH western ridge circulation, which is a first-order controller of SE US summer precipitation (Chapter 4). Generally, previous RCM experiments have suggested that bias in SE US rainfall simulation caused by LBCs could be largely reduced by configuring the southern boundary of the domain north of the tropics (Liang *et al.* 2001; Xue *et al.* 2007). In this study, we configured the LBC to the geographical boundary of the SE US domain, so that the uncertainties introduced by the representation of the NASH western ridge is minimized.

This study aims to understand the RCM simulation skills of SE US summer rainfall associated with the other two factors: physical parameterization scheme and model resolution. Analyzed from the climate perspective, the specific scientific questions addressed in this study are: 1) How sensitive are SE US summer rainfall simulations to different physical parameterization schemes, and what combination of physical parameterization schemes can optimize simulations of SE US summer rainfall? 2)

Through what physical mechanisms do the physical parameterization schemes influence SE US summer rainfall simulation skills? 3) Since the subgrid-scale parameterization schemes usually cause uncertainties in rainfall simulations, could an increase in model spatial resolution help reduce such uncertainties and improve simulations of SE US summer rainfall? The answers to these questions are sought by performing sensitivity tests and using a process-based evaluation technique.

5.1 Data, methods, and experiments

5.1.1 Observation data and driving reanalysis

In this study, rainfall observations are obtained from the Climate Prediction Center (CPC) unified daily precipitation archive (Higgins *et al.* 2000). The CPC is gridded observation data with a spatial resolution of 0.25 degree (approximately 25-km). The SE US is defined as the terrestrial domain over 23.5°N-36.5°N; 91°W-76°W (Li *et al.* 2011; Wang *et al.* 2010). The reliability of CPC precipitation data over the SE US has been verified by Li *et al.* (2013b). The summer season is defined as June-July-August (JJA); the seasonal mean thus refers to the daily precipitation averaged over JJA.

Climate Forecast System Reanalysis (CFSR) data (Saha *et al.* 2006) is adopted in this study to provide initial and boundary conditions for the simulations. The CFSR is a global reanalysis dataset, with a horizontal resolution of 0.5°×0.5° and 38 pressure levels. The dataset is available with a 6-hr increment. In our analysis, simulations driven by

CFSR data are compared with those driven by the NARR (Mesinger *et al.* 2006), the NCEP-R2 (Kanamitsu *et al.* 2002) and the ERA-Interim (Dee *et al.* 2011). We find that the choice of reanalysis forcing data does not influence summer rainfall simulations over the SE US in a discernible way (not shown).

5.1.2 Model descriptions and experiment setups

The RCM used in this study is the WRF model with the Advanced Research WRF (ARW) dynamic core version 3.4 (Skamarock *et al.* 2008), which has been widely used for operational forecasting and regional climate applications.

To study the SE US summer rainfall, the model domain is centered at 30°N, 88°W. The lateral boundary is composed of a 1-point specified zone and a 4-point relaxation zone to smooth potential pseudo-disturbances caused by numerical calculation[1] (Figure 5.1). The horizontal coordinates use the Lambert conformal conic projection with standard parallels at 30°N and 60°N. The model consists of 38 vertical layers, and the top level is set to 50 hPa.

[1] When computing the skill scores of rainfall simulations, we only consider the rainfall over the terrestrial SE US.

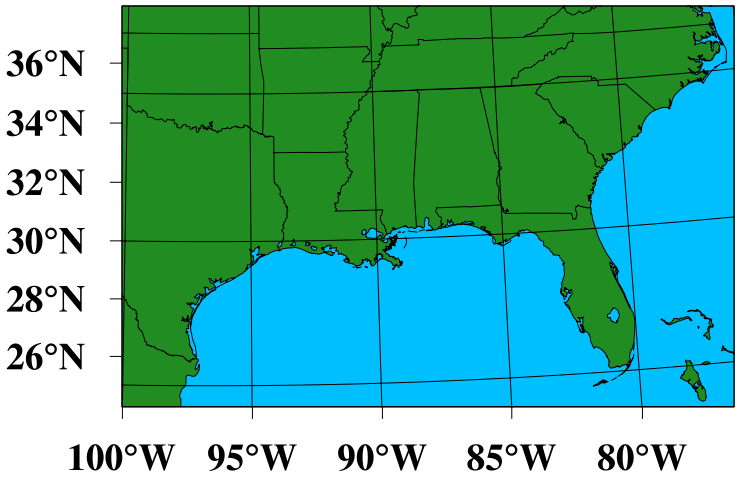

Figure 5. 1: Southeastern US domain used in WRF simulations.

The physical parameterization schemes used in this study include the Dudhia shortwave radiation (Dudhia 1989), Rapid Radiative Transfer Model (RRTM) longwave radiation (Mlawer *et al.* 1997), and Noah land surface model (Chen and Dudhia 2001). In our experiment, the microphysics, planetary boundary layer physics, and cumulus schemes vary between different simulations to test the sensitivity of SE US rainfall to the choice of these parameterization schemes. For the control experiment, the Thompson microphysics scheme (Thompson *et al.* 2008), the Betts-Miller-Janjic (BMJ) cumulus scheme (Janjic 1994, 2000), and the Bougeault-Lacarrère (BouLac) planetary boundary layer physics scheme (Bougeault and LaCarrere 1989) are first selected and additional justification is given in Section 5.2.

For the sensitivity experiments, the simulation period is Aug. 01 ~ Aug. 15, 2009 according to a pattern recognition algorithm (Appendix A). The simulation is initialized

on Jul. 27, 2009, and run through Aug. 15, 2009. The first five days are discarded as spin-up[2]. During the simulations, SST is updated every 6 hours.

5.1.3 Determination of WRF resolution for SE US experiments

In our analysis, the model resolution is determined by performing a 2-dimensional discrete cosine transform (DCT) on the summer rainfall climatology over the SE US. The DCT algorithm decomposes the rainfall data into several harmonic waves (Duhamel and Vetterli 1990). Power spectrum distribution versus wave number (wavelength) can provide information about the characteristic spatial scales of rainfall systems over the SE US (Bielli and Roca 2010; Denis *et al.* 2002). This information is utilized in this study to configure the spatial resolution of the WRF simulation.

Figure 5.2 shows the spatial power spectrum of SE US summer rainfall corresponding to the meridional and zonal wave numbers[3] as calculated using the DCT algorithm (Denis *et al.* 2002). Over the SE US, a large portion of the power spectrum energy for summer precipitation is concentrated within wave numbers less than 40 (i.e., spatial scales greater than 100 km, or approximately mesoscale). As the spatial scale

[2] The 5-day spin-up time is determined based on our 15-day test simulation with various spin-up periods ranging from 0 day to 10 days. The rainfall bias over the SE US domain is calculated and it is found that rainfall bias sharply decreases when spin-up time increases to 3 days and is stabilized afterward. Thus, spin-up period longer than 3 days is needed to ensure the numerical stability of the simulation results. We choose a 5-day period to further ensure the adequacy of the spin-up time.

[3] The wave number in the DCT algorithm can be converted to wavelength by the relationship, where $k = \sqrt{m^2 + n^2}$ is the spatial wave number (m and n are the zonal and meridional wave numbers, respectively), and L is the length of the analysis domain (Denis *et al.* 2002).

decreases, the power spectrum energy decreases as well (Figure 5.2a). Over the entire domain, rainfall systems with a spatial scale of 60 km have less than 1% of the power spectrum energy of 1000-km systems (Figure 5.2b). At the same time, the rainfall power spectrum approximates a white spectrum, indicating that rainfall systems with spatial scales less than 60 km are relatively stochastic (Figure 5.2b).

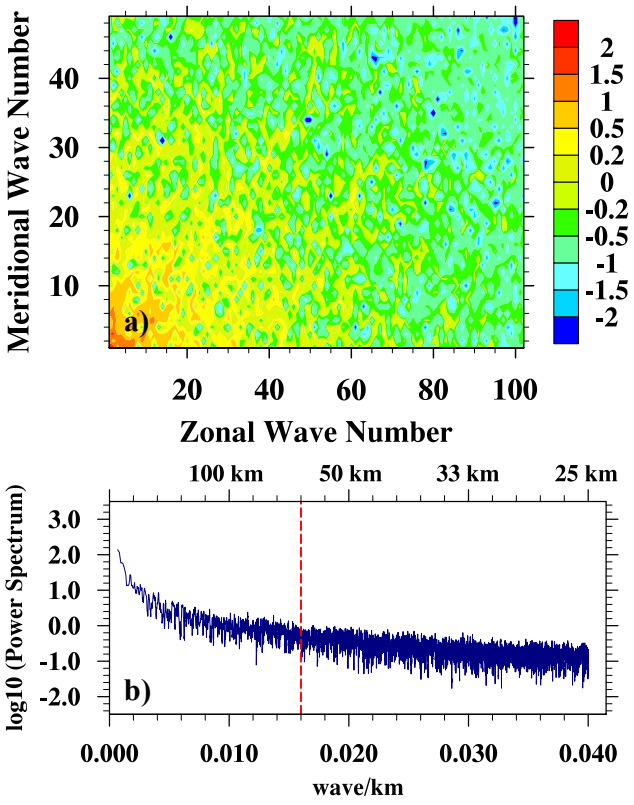

Figure 5. 2: a) Spatial power spectrum (shaded, unit: $mm^2\ day^{-2}$) of SE US summer precipitation climatology as calculated from discrete cosine transform (DCT); the color scale has been log-scaled; b) power spectrum versus spatial wavelength: the x-axis in the bottom (top) is the number of wave per kilometer (wavelength). The red dashed line denote wavelength = 60km, where power spectrum decreases to 1% of that with the largest wavelength.

According to the power spectrum of SE US summer rainfall, 60 km is characterized as a cut-off wavelength. Usually, resolving a rainfall system with a 60-km spatial scale requires a model horizontal resolution of about 15 km (Feser *et al.* 2011; Pielke 2002). Thus, in this study, the WRF simulation is configured at a 15-km horizontal resolution.

5.2 Influence of physical parameterization on SE US summer precipitation simulations

In this study, we focus on three categories of physical parameterization schemes, that is, microphysics, planetary boundary layer, and cumulus schemes, which are directly related to rainfall processes (Kunkel *et al.* 2002; Morrison *et al.* 2009; Wisse and Vilà-Guerau de Arellano 2004). The eleven microphysics, eight planetary boundary layer, and five cumulus schemes available in WRF ARW 3.4 are investigated. The first set of experiment is to test the sensitivity of WRF simulations to different microphysics schemes, where the planetary boundary layer physics uses the BouLac scheme, and the cumulus scheme uses the BMJ scheme throughout our whole experiments.

5.2.1 Sensitivity experiments

To assess the sensitivity of the WRF simulation to physical parameterizations, the Taylor diagram is used (Figure 5.3). The Taylor diagram combines the pattern correlation coefficient (PCC) and the ratio of the simulated rainfall standard deviations over those observed (Taylor 2001) and has been widely used to evaluate climate models (AchutaRao and Sperber 2006; Gleckler *et al.* 2008). In the Taylor diagram, the distance

between the simulated rainfall and observations reflects the model simulation skills (Taylor 2001).

Figure 5.3 indicates that the WRF simulation skill in SE US summer rainfall (Aug. 01~Aug.15, 2009) does not change significantly in response to the different microphysics schemes, as shown in Figure 5.3a where the PCC clusters around 0.50 and the ratio of the spatial standard deviation is within a range of 0.63 ~ 1.02. These results imply that the microphysics parameterizations embedded in WRF may be sufficient to represent the microphysical processes in SE US summer rainfall systems.

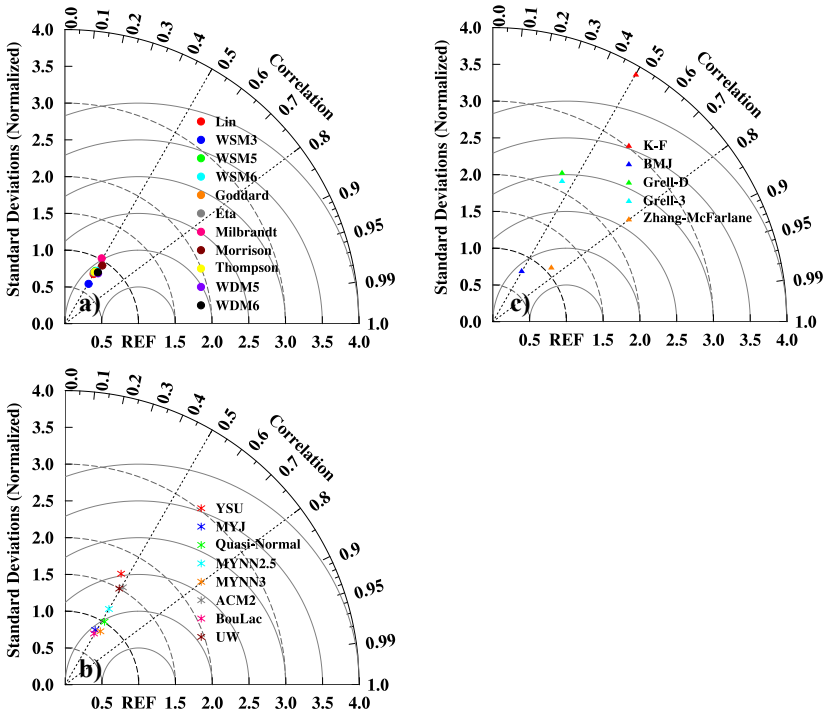

Figure 5. 3: Taylor diagrams evaluating WRF simulation skill of SE US summer precipitation by using different a) microphysics (dots); b) planetary boundary layer (asterisks); and c) cumulus (upward triangles) schemes. The radius represents the ratio between the WRF-simulated and the observed spatial standard deviation of rainfall. The cosine of the angle equals the rainfall pattern correlation coefficients between the WRF simulations and observations.

In the following experiments, we use the Lin microphysics scheme (Lin *et al.* 1983), which demands the least computing resources and has the relatively high PCC and close to unity standard deviation ratio. At the same time, the BMJ cumulus scheme is used for the iterations of planetary boundary layer experiments. The set of experiments with different planetary boundary layer schemes shows a larger spread in the simulation results than that for microphysics (Figure 5.3a and b). This spread comes mainly from the increased range in spatial standard deviations, whereas the PCC is concentrated at around 0.50 (Figure 5.3b). Among the tested schemes, the simulation with the MYNN-3 planetary boundary layer physics scheme (Nakanishi and Niino 2006) generates a PCC of 0.55 and the ratio of the spatial standard deviation is 0.87 (Figure 5.3b). Synthetically, the simulation by MYNN-3 scheme is the closest to observations (Figure 5.3b). Thus, MYNN-3[4] is adopted in the following sensitivity experiments in which only the cumulus scheme changes.

When the cumulus schemes are varied, the simulation results show an even wider spread (Figure 5.3c) than those for the planetary boundary layer physics experiments (Figure 5.3b), suggesting that the WRF simulation of SE US summer rainfall is highly sensitive to the cumulus schemes included in the model. In Figure 5.3c, the ratios of the spatial standard deviation of SE US summer rainfall show a large range among the

[4] The MYNN-3 scheme is not compatible with the Zhang-McFarlane scheme; thus the UW planetary boundary layer physics scheme is used in the simulation with the Zhang-McFarlane scheme.

cumulus schemes. The Kain-Fritsch (K-F) scheme (Kain 2004) produces the largest deviation (3.8 times larger than the observations), while the Zhang-McFarlane scheme (Zhang and McFarlane 1995) produces the deviation value closest to the observations. Overall, the sensitivity experiments reflect the importance of the cumulus schemes in rainfall simulation over the SE US, which has also been emphasized in previous studies (Jankov *et al.* 2005; Bukovsky and Karoly 2009).

The above analysis suggests that the cumulus schemes affect the WRF simulation skills mainly for SE US summer rainfall. Furthermore, observed evidence shows that SE US summer rainfall, especially its spatial heterogeneity, is controlled largely by convective systems (Konrad 1997; Baigorria *et al.* 2007; Kunkel *et al.* 2012), indicating that realistically representing convective processes in cumulus parameterization schemes is important for an accurate simulation of SE US summer rainfall. Thus, an analysis of how cumulus schemes influence SE US summer rainfall simulation is imperative to improving rainfall simulation skills. It can also provide insights into the physical mechanisms of rainfall over the SE US.

The simulated spatial patterns of SE US summer rainfall using different cumulus schemes are compared with observations in Figure 5.4, where the simulated rainfall using the K-F, Grell-Dévényi (Grell and Dévényi 2002), and Grell-3 (Grell and Dévényi 2002) schemes is overestimated over the SE US (Figure 5.4a-c). In particular, all three schemes tend to simulate maximum rainfall over the coast of the Carolinas along with a

southwest-northeast-oriented rain belt sweeping the eastern coast of the SE US (Figire 5.4a-c). Such a rainfall distribution is not seen in the observations (Figure A1.b). Averaged over the terrestrial area of the SE US, the net wet bias is approximately 3 mm day^{-1} in the simulations using the Grell-Dévényi or Grell-3 schemes (Figure 5.4g-h), and 4.8 mm day^{-1} using the K-F scheme (Figure 5.4f). Rainfall simulated using the BMJ (Figure 5.4d) and the Zhang-McFarlane schemes (Figure 5.4e) reasonably captures the observed rainfall pattern although the BMJ scheme results in a net dry bias compared to the observations. The underestimation of rainfall with the BMJ scheme is most evident over Florida and the Gulf Coast (Figure 5.4i), with a domain-averaged dry bias of 0.8 mm/day, exceeding one standard deviation of the interannual variation in SE US summer rainfall (Li *et al.* 2013a). Such a rainfall bias is largely reduced in the Zhang-McFarlane scheme, with a domain-averaged bias of less than 0.1 mm day^{-1} (Figure 5.4j). In addition, the Zhang-McFarlance scheme captures well the magnitude and local maximum of the rainfall distribution when compared to the observations (Figure 5.4f).

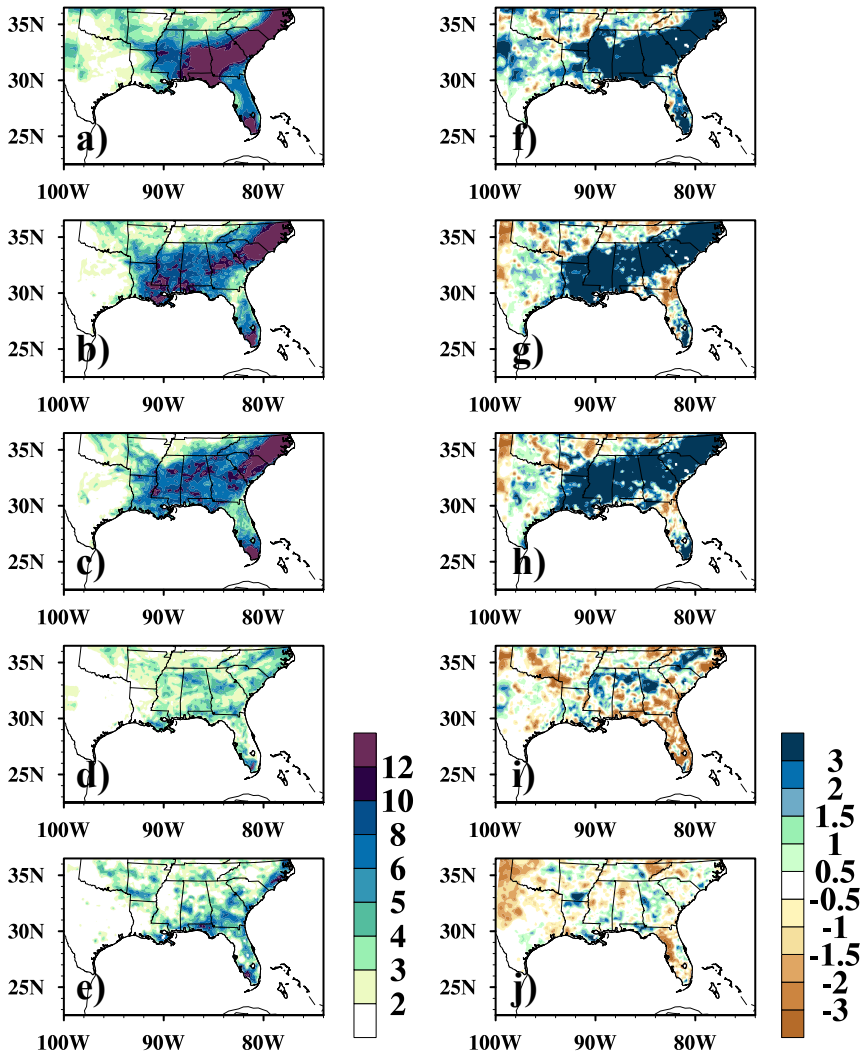

Figure 5. 4: SE US summer precipitation (shaded, unit: mm day^{-1}) during Aug. 1 ~ Aug. 15, 2009, as simulated by WRF with the a) K-F; b) Grell- Dévényi; c) Grell-3; d) BMJ; and e) Zhang-McFarlane schemes. f) – j) are the same as a) – e), but showing the simulated bias in precipitation (shaded, unit: mm day^{-1}) compared with observations as in Figure A1b.

Among the five cumulus schemes tested in this study, the Zhang-McFarlane scheme outperforms the other four in its simulated spatial distribution of rainfall (Figure 5.4e and j), domain-averaged rainfall, and the evaluation metrics that are depicted by the

Taylor diagrams (Figure 5.3c). Thus, the improved WRF simulations of SE US summer rainfall can be generated by applying the Zhang-McFarlane scheme in combination of Lin microphysics and UW planetary boundary layer schemes.

5.2.2 10-yr simulations of SE US summer precipitation

The sensitivity experiments suggest that the WRF simulation of SE US summer rainfall is most sensitive to the choice of cumulus schemes. To validate this result, two 10-yr (2001-2010) simulations are performed. The 10-yr simulation consists of 10 separate summer runs, without applying any nudging skills. Only the Zhang-McFarlane and BMJ schemes[5] are considered and compared, because both schemes simulate rainfall patterns that are relatively closer to the observations based on the above sensitivity experiments (Figure 5.4). Furthermore, the Zhang-McFarlane scheme outperforms all the other schemes, while BMJ is the only scheme that simulates the dry bias over the SE US (Figure 5.4). Thus, the analysis of the rainfall simulations with these two schemes provides us with an understanding of the mechanisms that control the amount of summer rainfall over the SE US.

Figure 5.5 compares the simulated and observed rainfall during the 10-yr period. The observed rainfall shows a sharp spatial gradient along the coastal regions (Figure 5.5a), due mainly to land-sea heating contrasts during the summer (Wu *et al.* 2009), and

[5] The Lin microphysics scheme is used for the 10-yr simulation. For the simulation with Zhang-McFarlane (BMJ) cumulus scheme, UW (MYNN3) planetary boundary layer schemes are used.

the contribution of tropical activities (Kunkel *et al.* 2012). Such a rainfall pattern is generally captured by both schemes (Figure 5.5b-c): the simulated summer rainfall is heavier over the coastal regions and decreases inland.

The BMJ scheme, however, underestimates coastal rainfall by 20%, especially over Florida, where the dry bias is more than 2 mm day^{-1} (Figure 5.5b and d). In contrast, the Zhang-McFarlane scheme not only captures the spatial distribution of the rainfall but also simulates rainfall magnitude that is fairly close to observations (Figure 5.5c and e), especially over the coastal regions (Figure 5.5b-e). The PCC and RMSE are 0.87 and 0.62 mm day^{-1} with the Zhang-McFarlane, respectively, which are better than 0.69 and 1.07 mm day^{-1} with the BMJ.

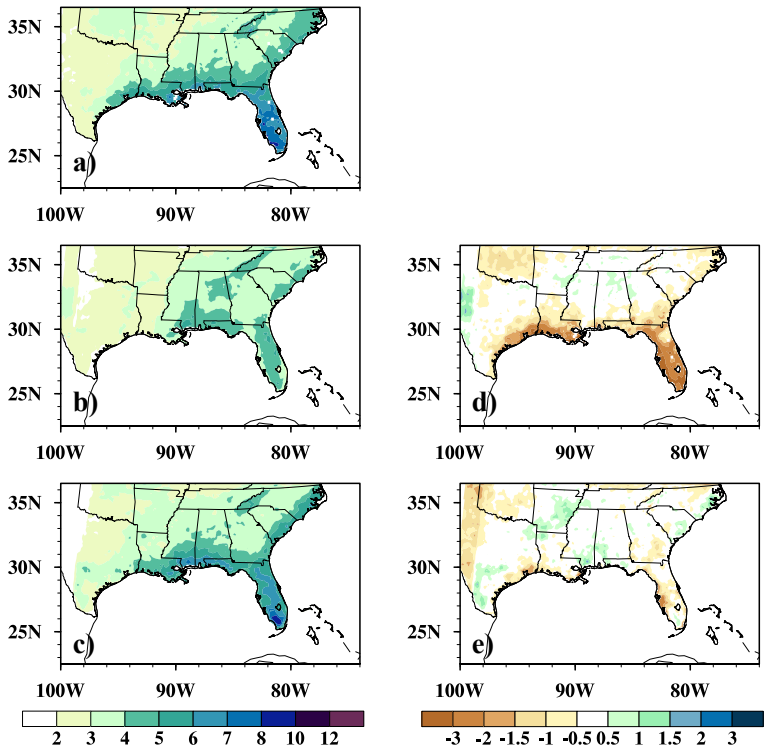

Figure 5. 5: 2001-2010 summer precipitation climatology over the SE US (shaded, unit: mm day^{-1}): a) observations; and WRF simulations with the b) BMJ and c) Zhang-McFarlane schemes; their simulation bias (shaded, unit: mm day^{-1}) is shown in d) and e), respectively.

The time series of the domain-averaged simulated summer rainfall are shown in Figure 5.6. Due to the substantial dry bias over the coastal regions (Figure 5.5e), the BMJ scheme underestimates domain-averaged rainfall by 0.66 mm day^{-1}. However, the bias simulated by the Zhang-McFarlane scheme is reduced to 0.10 mm day^{-1}.

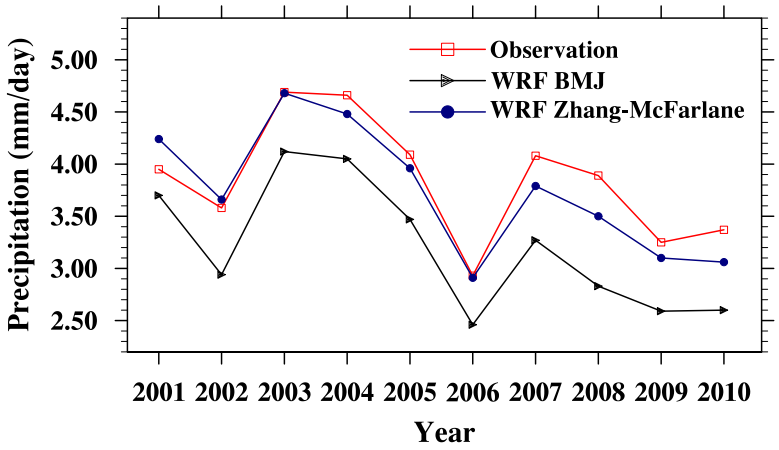

Figure 5. 6: Interannual variation in summer precipitation (curves, unit: mm day^{-1}) averaged over terrestrial SE US (23°N-36.5°N, 91°W-76°W) during 2001-2010. The red curve is the observations, and the black (blue) curve is the WRF simulation with the BMJ (Zhang-McFarlane) scheme.

The skill scores obtained from this additional 10-year simulation agree well with those from the 15-day sensitivity experiments (Section 3.2). This consistency suggests that our statistical method designed to locate a rainfall pattern that resembles its climatology is effective in identifying a representative simulation period for conducting the sensitivity experiments. Such a method should therefore be applicable to regional climate simulations over different regions and temporal periods.

5.2.3 Mechanism of cumulus scheme impact on SE US rainfall simulations

Our analysis pinpoints cumulus schemes as one of the most important elements affecting the ability of WRF to simulate SE US summer precipitation. The influences of cumulus schemes are especially evident over the coastal regions (Figure 5.5), where precipitation is tightly associated with convective systems (Knight and Davis 2007;

Kunkel *et al.* 2012). Understanding how different cumulus schemes generate different spatial patterns and magnitudes of rainfall is thus critical to understanding the WRF simulation skill of SE US summer rainfall.

Here, we focus on the Zhang-McFarlane and BMJ schemes by analyzing their 10-year simulation results (Figures 5.5 and 5.6). In both schemes, convection adjusts local atmosphere toward defined equilibrium states, and convective precipitation onsets only when certain triggering criteria are met (Arakawa 2004; Janjic 1994, 2000; Zhang and McFarlane 1995). Usually, among different parameterization schemes, the triggering functions differ substantially (Table 5.1). Thus, rainfall-triggering processes might cause the discrepancies in their simulated rainfall.

Table 5. 1 Description of the cumulus schemes tested in this study

Cumulus Scheme	Mass-Flux Closure and Convection Triggering	References
Kain-Fritsch (K-F)	a). The scheme uses a simple cloud model with moist updrafts and downdrafts. b). Deep convection is activated if parcel vertical velocity remains positive over a depth that exceeds the minimum cloud depth. c). Activated convection has a given updraft mass flux, based on which downdraft mass flux is estimated according to relative humidity. d). Convective available potential energy (CAPE) is used as mass-flux closure. Convection rearranges mass in the column until at least 90% of the CAPE is removed. e). Originally developed for mesoscale models	Kain and Fritsch (1990, 1993); Kain (2004)
Grell-Devenyi Grell-3	The Grell–Devenyi and Grell-3 schemes consist of an ensemble of cumulus scheme, in which multiple schemes are run within each grid box and the results are averaged.	Grell and Devenyi (2002)
Betts-Miller-Janjic (BMJ)	a). The deep convection profiles depend on the cloud efficiency, which in turn depends on the entropy change, precipitation, and mean temperature of the cloud. b). Deep convection is triggered only when cloud entropy changes pass a threshold value. c). In searching for the cloud top, the ascending particle mixes with the environment, and the work of the buoyancy force on the ascending particle is required to exceed a prescribed positive threshold. d). Originally developed for mesoscale models	Betts (1986); Betts and Miller (1986); Janjic (1994, 2000)
Zhang-McFarlane	a). The scheme is based on plume ensemble. The drafts have the same initial mass flux and entrainment rate depends on the large-scale thermal structure of the atmosphere. b). Convection exists only when CAPE consumption is positive. c). Convection removes CAPE, and the convective precipitation, is proportional to the amount of CAPE in the atmosphere. d). Originally developed for GCMs	Zhang and McFarlane (1995)

To evaluate the rainfall-triggering processes in these two schemes, the number of rainy days during summer seasons was counted. Rainy days are defined as those days when the rain gauge (model grid point) receives more than 0.4 mm precipitation within 24 hours in observations (WRF simulation). A larger number of rainy days indicate more frequent triggering of rainfall events in the summer. In addition, average storm intensity is defined as the rainfall amount averaged over the rainy days.

The observed number of rainy days shows a spatial pattern that closely resembles the seasonal mean rainfall pattern (Figures. 5.5a and 5.7a). A high frequency of rainfall events (more than 70% of the summer seasons) is observed along the coastal regions (Figure 5.7a). In contrast, the average storm intensity does not show a pattern coherent with observations. The observed local maximum of storm intensity is in Oklahoma instead of over the coastal regions where rainfall occurs more frequently (Figure 5.7d). Synthetically, on a seasonal scale, SE US summer precipitation, especially the convective precipitation over the coastal regions, is related more to the frequency of rainfall events than to storm intensity (Figure 5.7a and d). Such a feature indicates that the parameterization of rainfall-triggering processes is critical to WRF's ability to simulate SE US summer precipitation.

Compared with observations, the better performance of the Zhang-McFarlane scheme is reflected in its simulation accuracy in the number of rainy days. Specifically, the BMJ scheme substantially underestimates the number of rainy days over the coastal

regions by about 10 days per summer season, resulting in its dry bias in the seasonal rainfall simulation (Figure 5.7b). In contrast, the number of rainy days over the coastal regions is reasonably simulated with the Zhang-McFarlane scheme, with only slight underestimation over Florida (~2 days) (Figure 5.7c). Thus, the more realistic performance of the Zhang-McFarlane scheme in simulating SE US summer rainfall relies on its better representation of rainfall-triggering processes.

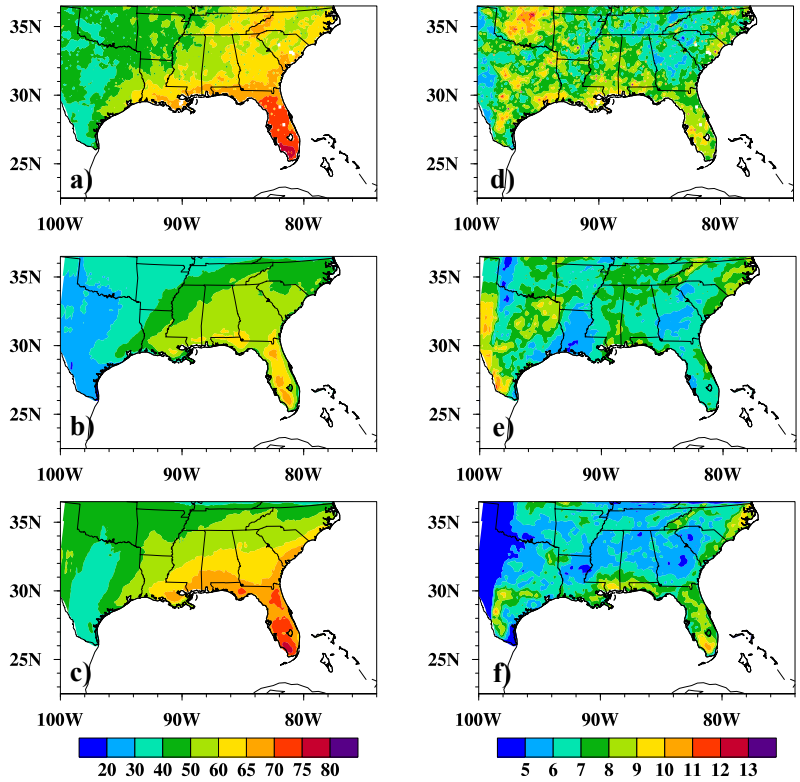

Figure 5. 7: 10-yr (2001-2010) average number of rainy days (shaded, unit: days) during summer: a) observations, and WRF simulations with the c) BMJ, and e) Zhang-McFarlane schemes; and the average storm intensity (shaded, unit: mm day^{-1}) in b) observations, and WRF simulations with the d) BMJ, and f) Zhang-McFarlane schemes.

The reasonable triggering of rainfall events in the Zhang-McFarlane scheme might be due to the assumptions it uses to parameterize cumulus convection (Table 5.1). The parameterization of the Zhang-McFarlane scheme uses the convective available potential energy (CAPE) (Zhang and McFarlane 1995). CAPE is calculated as the vertically integrated parcel buoyant energy (Moncrieff and Miller 1976) and is usually used to diagnose convection-related activities (Adams and Souza 2009; Emanuel 1994; Li and Fu 2004; Stevens 2005; Tompkins 2001).

Over the SE US, summer rainfall shows a positive relationship with CAPE (Figure 5.8c). The distribution of CAPE almost mirrors the rainfall distribution except in the Appalachian Mountains, where rainfall is mainly forced by orographic lifting (Figure 5.8a and c). The correlation between CAPE and summer rainfall is clear over the coastal regions, with a high CAPE corresponding with high rainfall amount and rainy day numbers (Figures 5.5a, 5.7a, and 5.8a and c).

In the Zhang-McFarlane scheme, the CAPE criterion is used to trigger convection in addition to the mass-flux closure for convection (Table 5.1; Zhang and McFarlane 1995). Constrained by mass-flux closure, the cumulus convection removes CAPE accumulated by large-scale forcing, which acts to stabilize the local atmospheric column (Zhang and McFarlane 1995). Thus, the Zhang-McFarlane scheme implies a positive "CAPE-precipitation" relationship [Figure 5.8b and d; (Arakawa 2004; Adams and Souza 2009)], similar to that observed over the SE US (Figure 5.8a and c). As a result, the observed

summer rainfall pattern (Figure 5.5a) and rainy day number (Figure 5.7a) over the SE US are likely to be reproduced by the Zhang-McFarlane scheme, with a more frequent onset of convection leading to stronger seasonal precipitation over the coastal regions [Figures 5.5c and 5.7c; (Liu *et al.* 2010)], where CAPE is the highest within the SE US domain (Figure 5.8b).

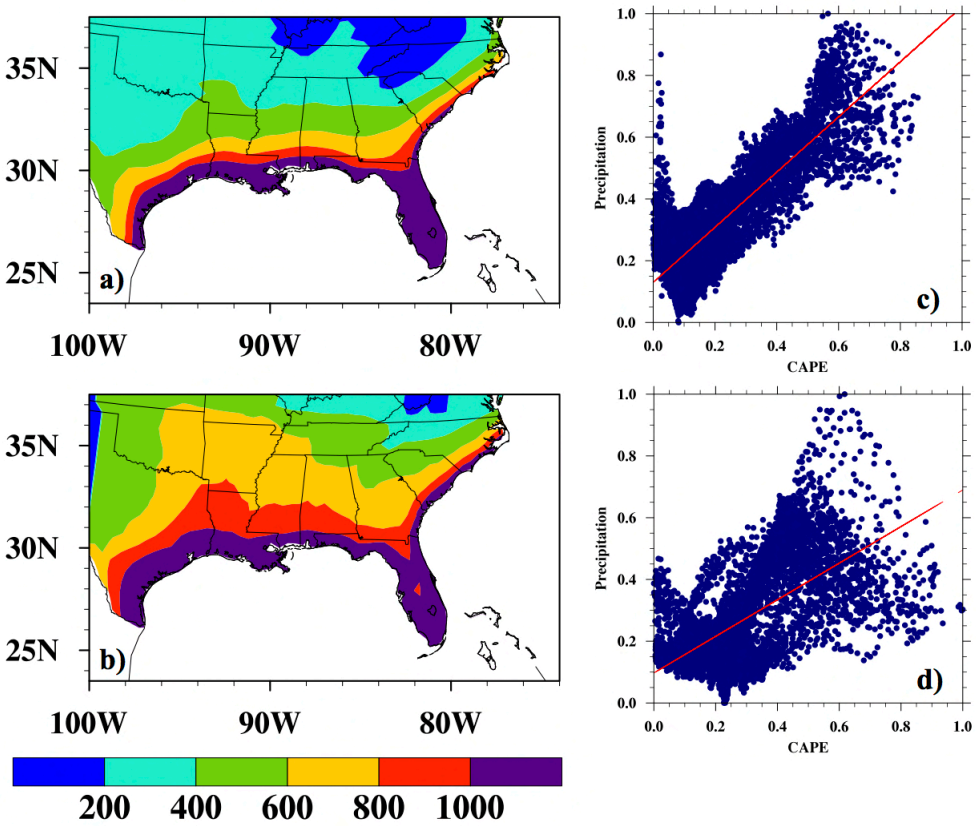

Figure 5. 8: 2001-2010 JJA climatology of convective available potential energy (CAPE) over the SE US (shaded, unit: J Kg^{-1}): a) observations; b) WRF simulation with the Zhang-McFarlane scheme. c) and d) are the CAPE (normalized) versus summer precipitation (normalized) over the SE US in observations and the WRF simulation with the Zhang-McFarlane scheme, respectively. The red lines in c) and d) are the best least squares fitting lines.

In contrast to the Zhang-McFarlane scheme, the other 4 cumulus schemes fail to capture the observed "CAPE-precipitation" relationship, thus lowering their skills in simulating SE US summer rainfall. Figure 10 illustrates the relationship between CAPE and precipitation as simulated by the other 4 cumulus schemes in the sensitivity experiment. The K-F, Grell-Dévényi, and Grell-3 schemes tend to simulate strong precipitation over regions with low CAPE values (Figure 5.9a~c), resulting in an overestimate of precipitation across the SE US (Figure 5.4). On the other hand, the BMJ scheme simulates a negative "CAPE-precipitation" relationship over the SE US (Figure 5.9d), which might explain its dry bias over the coastal regions along with its wet bias in the interior domain (Figure 5.4i).

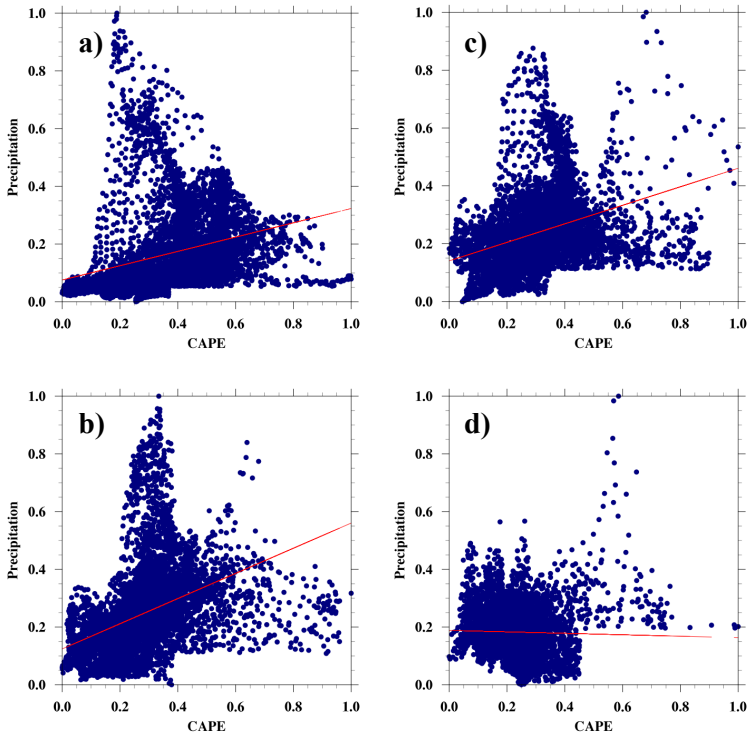

Figure 5. 9: CAPE (normalized) versus summer precipitation (normalized) over the SE US in the WRF simulation (blue dots) with the a) K-F, b) Grell-Dévényi, c) Grell-3, and d) BMJ schemes, respectively. The red lines are the best least squares fitting lines.

The analysis of the relationship between CAPE and precipitation suggests that the representation of this relationship is a key to the high-quality simulations of SE US summer precipitation, whereas the effects of the resolutions on the effectiveness of using the cumulus schemes is less significant. The Zhang-McFarlane scheme was originally developed for GCMs (Zhang and McFarlane 1995), whose grid points are usually of 10^2 km (Taylor *et al.* 2012). In contrast, the other schemes are designed mainly for mesoscale model, indicating that they are supposed to be more skillful in regional climate simulations than the Zhang-McFarlane scheme (Table 5.1). The better performance of

Zhang-McFarlane scheme thus indicates the importance of the representation of physical processes responsible for rainfall generation over the SE US. Overall, the lower skills of these four schemes might be attributed to their inability to capture the observed "CAPE-precipitation" relationship.

5.3 Choices between a very-high-resolution convection-permitting simulation and a low-resolution Zhang-McFarlane simulation

Our analysis indicates that cumulus schemes cause the greatest uncertainty in WRF-simulated SE US summer rainfall, compared with microphysics and planetary boundary layer schemes (Figures 5.3 and 5.4). Theoretically, the uncertainty from cumulus schemes in rainfall simulations can be eliminated by increasing the WRF resolution to explicitly resolve convective systems (Arakawa 2004; Weisman *et al.* 1997). Next, we will examine whether using a convection-permitting resolution with WRF improves the simulations of precipitation over the SE US.

In order to explicitly resolve convective systems, the WRF model is configured over the SE US (Figure 5.1) with a 3-km horizontal resolution. The simulation period is Aug. 1 ~ Aug. 15, 2009 (Appendix A). The cumulus scheme option is turned off, while the other physical parameterization schemes are the same as in the cumulus scheme sensitivity experiment (see Section 5.2.2). To evaluate the performance of WRF at the 3-km

resolution, the Zhang-McFarlane simulations at the 15-km resolution and observations are used for comparison.

Figure 5.10 shows the rainfall simulated by the 3-km experiment. Generally, with a finer resolution, more local details in rainfall are reflected in the 3-km simulation (Figure 5.10) compared to the 15-km simulation (Figure 5.4). When compared to the observations, the 3-km simulation captures the high precipitation rate over the coastal regions, although it underestimates the rainfall over Florida and the inland SE US (Figure 5.10). Generally, the 3-km simulation outperforms the simulations with the majority of cumulus schemes (Figure 5.4a-c), indicating that the convection-permitting approach can improve SE US summer rainfall simulations to some extent. However, the 3-km simulation fails to outperform the 15-km Zhang-McFarlane scheme[12]: the PCC of the 3-km simulation is only 0.43 (0.77 in Zhang-McFarlane), and its RMSE reaches 2.38 mm day^{-1} (1.28 mm day^{-1} in Zhang-McFarlane). To avoid the artificially high skill scores of 15-km Zhang-McFarlane scheme due to the usage of relatively coarse resolution observation data (~25km), we also calculate the PCC and RMSE using the 4-km Parameter-elevation Regression on Independent Slope Model (PRISM) data (Daly *et al.* 2008). The change to higher resolution observations does change the PCC and RMSE

[12] The influence of data interpolation methods on the calculation of PCC and RMSE is noticed. Thus, multiple interpolation methods, including the nearest neighbor, kriging, bi-linear interpolation, and cubic spline, are compared. The specific PCC and RMSE values do vary among different methods. However, the conclusion does not change based on qualitative comparison of the 3-km simulation and the Zhang-McFarlane 15-km simulation.

values, however, the overall skill scores of the Zhang-McFarlane scheme are still higher than that of the 3-km simulation. Specifically, the PCC is higher, and the RMSE is lower in the 15-km Zhang-McFarlane simulation (PCC=0.66; RMSE=1.86) than in the 3-km simulation (PCC=0.45; RMSE=2.64). Thus, the 15-km Zhang-McFarlane simulation generally outperforms the 3-km simulation. Considering that the 3-km simulation requires 125 times more computational time on our local computing facilities than the 15-km simulation, our results indicate that choosing an optimal cumulus scheme can more effectively improve the simulations of SE US summer rainfall than using a convection-permitting resolution.

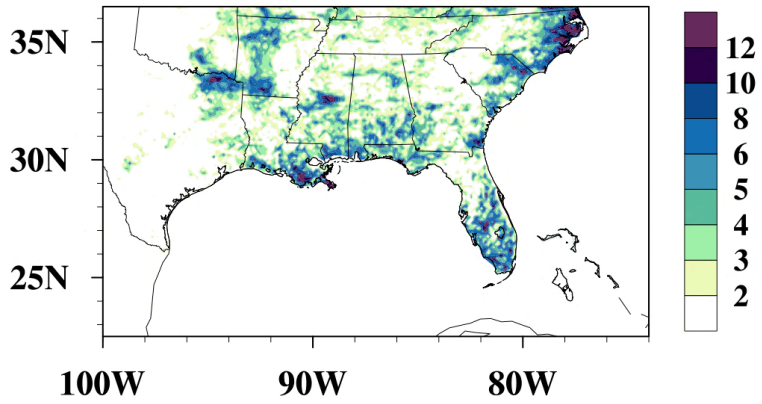

Figure 5. 10: Aug. 01 ~ Aug. 15, 2009, summer precipitation (shaded, unit: mm day^{-1}) as simulated by 3-km WRF convection-permitting configurations; in the simulation, cumulus scheme is turned off and the rainfall is generated only by microphysics.

The inferior performance of the 3-km simulation compared to the 15-km Zhang-McFarlane simulation might be caused by multiple factors. First, SE US summer rainfall systems are mainly tropical convective systems, which usually require a resolution finer

than 3 km to fully resolve them (Weisman *et al.* 1997). Second, it might indicate that SE US summer rainfall is fairly stochastic at spatial scales less than 60 km (Figure 5.2). Thus, the physical models cannot provide further improvement in simulation skills even with a fivefold increase in resolution. In addition, the location of the lateral boundaries may also influence to some different extent the skill of high and low resolution RCM simulations. All these hypotheses about WRF simulation skill of SE US summer precipitation need further investigation.

5.4 Summary and Conclusions

RCMs provide "added-value" to GCMs in simulating SE US summer climate, due to their higher horizontal resolution and more sophisticated physics. However, satisfactory regional climate simulation skills have not yet been achieved over this region, especially for summer precipitation (Lo *et al.* 2008; Mearns *et al.* 2012; Bowden *et al.* 2013). Some previous studies have pointed out the influences of lateral boundary conditions on SE US rainfall simulation (Castro *et al.* 2005; Xue *et al.* 2007). By performing WRF simulations driven by CFSR data, this study addresses two other important aspects associated with WRF's simulation skills, that is, physical parameterization scheme and model resolution (Castro *et al.* 2005; Christensen *et al.* 2007; Bukovsky and Karoly 2009; Foley 2010; Rummukainen 2010).

Sensitivity experiments are performed to test the WRF simulation skills of SE US summer precipitation in response to various physical parameterization schemes. The period of Aug. 01 ~ Aug. 15, 2009, is chosen as a simulation period because the rainfall pattern averaged over this time span "best" resembles SE US summer rainfall climatology (Figure A1). The WRF model is configured over the SE US (Figure 5.1) with a 15-km resolution according to the DCT analysis (Figure 5.2). The sensitivity experiments show that the WRF simulation of SE US summer precipitation is most sensitive to the cumulus schemes in WRF, moderately sensitive to the planetary boundary layer schemes, and least sensitive to the microphysics schemes.

The sensitivity of the rainfall simulation to cumulus schemes indicates the importance of convective systems in the formation of SE US warm-season precipitation patterns (Konrad 1997; Kunkel *et al.* 2012), consistent with previous studies (Bukovsky and Karoly 2009). Among five of the cumulus schemes analyzed in this study, three of them (K-F, Grell-Dévényi, and Grell-3) simulate a strong wet bias, especially over the coast of the Carolinas, causing significant overestimation of precipitation over the region (Figure 5.4b-d). In contrast, the BMJ scheme underestimates summer precipitation, resulting in a dry bias, especially over the coastal regions. The Zhang-McFarlane scheme realistically reproduces the observed spatial pattern of precipitation, the domain-averaged precipitation amount, and all the designed evaluation metrics. Thus, based on our simulations, Zhang-McFarlane scheme seems an effective approach to the

improvement of SE US summer precipitation simulations by WRF. However, we should make clear that the Zhang-McFarlane scheme might not be the only method to improve SE US summer precipitation simulations. Previous studies have shown that the application of interior grid nudging (Lo *et al.* 2008; Bowden *et al.* 2013), adjustment of parameters in cumulus schemes (Yang *et al.* 2012), and the consideration of "cumulus cloud – radiation" feedback in WRF (Alapaty *et al.* 2012) can also improve SE US summer precipitation simulation to some extent.

Further analysis suggests that the superior rainfall simulation skills by the Zhang-McFarlane scheme are attributable to its reasonable representation of rainfall-triggering processes over the SE US. The observed number of rainy days over the SE US is accurately simulated by the Zhang-McFarlane scheme, with less than 5% error. The cumulus parameterization in the Zhang-McFarlane scheme implicitly assumes a positive relationship between rainfall and CAPE (Zhang and McFarlane 1995). Such a relationship realistically reflects the summer precipitation pattern over the SE US (except for the Appalachian Mountains) (Figure 5.8) and thus improves the WRF simulation skills in SE US summer precipitation using the Zhang-McFarlane scheme.

WRF rainfall simulation with the Zhang-McFarlane scheme at the 15-km resolution is also compared with that produced using a 3-km convection-permitting resolution where cumulus scheme is turn off. The PCC and RMSE indicate that the 3-km simulation does not outperform the 15-km Zhang-McFarlane simulation (Figure 5.10).

On top of that, the 3-km simulation takes 125 times more computational time on our local computing platform. Thus, our analysis suggests that selecting an optimal cumulus parameterization scheme is an effective way to obtain a satisfactory simulation of SE US summer precipitation. This study provides an important tool for reliable future climate forecasts and informed water resource management over the region.

6. Future changes in SE US summer precipitation

There is a broad consensus among observations and model simulations that the continuously increasing GHGs could moisten the troposphere (Dai 2006; Ross and Elloitt 2001; Sherwood *et al.* 2010), accelerate the global hydrological cycles (Held and Soden 2006; Huntington 2006; Stocker and Raibe 2005; Yang *et al.* 2003), and result in the shift of global and regional precipitation patterns (Groisman *et al.* 2004; Huntington 2006; Trenberth 2011).

Over the US, the increase in GHG concentrations tends to cause drying over the Southwest (Seager *et al.* 2007) and summertime Northeast (Hayhoe *et al.* 2007), wetting over the Midwest and Great Lakes during winter and spring (Cook *et al.* 2008; Patricola and Cook 2013). Over the SE US, no significant trend of summer precipitation is observed in recent decades. However, summer precipitation variability has significantly intensified (Li *et al.* 2011; Wang *et al.* 2010).

Projections of future precipitation changes are made mainly through the simulations using GCMs and RCMs (Chen *et al.* 2003; Christensen *et al.* 2007; Liang *et al.* 2006; Mearns *et al.* 2003). Over the SE US, high uncertainty exists in terms of projecting the response of summer precipitation to GHGs forcing, because the simulations of rainfall is sensitive to model dynamic cores as well as physical parameterizations over this region (Chen *et al.* 2003; Liang *et al.* 2006; Mearns *et al.* 2003). Generally, these studies focus on the changes in mean precipitation. However, future changes in precipitation

variability have not been fully addressed and the controlling mechanism has not been studied, although many critical impacts of climate are controlled by rainfall variability rather than the mean (Katz and Brown 1992).

This study aims to examine the projected changes in SE US summer precipitation variability and elucidate their working mechanisms. Assessing the causes of variability change is difficult, since variability is linked to sample variance, which is the second moment of statistical samples. Thus, it is intrinsically more complicated than the sample mean. In order to study the mechanisms responsible for precipitation variability change, regional moisture budget processes are analyzed. A novel variance partition algorithm is formulated and applied to quantify thermodynamic and dynamic contributions to precipitation variability change, whereby the mechanisms are studied (Appendix B).

We adopt the simulations under the Representative Concentration Pathway 4.5 (RCP4.5) scenario to represent future climate. The RCP4.5 is a midrange mitigation emission scenario, in which CO_2 concentrations gradually increase to 650ppm in 2100 and are stabilized afterward. Meanwhile, radiative forcing steadily increases to 4.5 W m^{-2} till 2100 and is then stabilized (Moss *et al.* 2010; Taylor *et al.* 2012). The simulated precipitation, 850hPa geopotential height, and the variables involved in the quantification of large-scale seasonal mean moisture transport (Section 2) are analyzed and compared with their counterparts in Historical runs to assess future changes in SE US summer precipitation due to anthropogenic forcing.

Quantile-normalization method (Bolstad *et al.* 2003) is applied to SE US summer precipitation and moisture transport as simulated by CMIP5 models to avoid artificial sample variance caused by model spread in simulating regional climate. Let $\mathrm{Pr}_k = \left(\mathrm{Pr}_{k1},...,\mathrm{Pr}_{k50}\right)$ denote a 50-yr precipitation sample simulated by the k-th model[1]. The quantile normalization process is as follows: a) precipitation time series from the k-th model is sorted from low to high as: $q_k = \left(q_{1k},...,q_{k50}\right)$; b) calculate the ensemble mean of the i-th quantile precipitation simulated by each model: $\overline{q}_i = \frac{\sum_{k=1}^{n} q_{ki}}{n}$, where bar is the ensemble mean of model simulated i-th quantile precipitation and q_{ki} is the i-th quantile precipitation simulated by the k-th model; c) construct PDFs using the $\overline{q} = \left(\overline{q}_1,...,\overline{q}_{50}\right)$.

6.1 CMIP5 model projections of SE US summer precipitation in the future

Future changes in SE US summer precipitation are projected base on the multi-model ensemble. In this study, both unweighted ensemble and weighted ensemble projections are considered. In the unweighted ensemble, the projection by each model is given the same weight regardless of their performance in simulating SE US summer precipitation in the current climate. By contrast, model quality is taken into account in weighted ensemble projections. The models that better simulate SE US summer

[1] Same quantile-normalization process is applied to moisture transport time series as simulated by CMIP5 models.

precipitation in the current climate are assumed to be more reliable in projecting future climate change, and are thus assigned higher weight (see details below).

6.1.1 Unweighted ensemble projections

The ensemble of CMIP5 models suggests that the recently intensified summer precipitation variability would further intensify in a warming climate. Under the RCP4.5 scenario, the ensemble of CMIP5 models shows an increase in the standard deviation of summer precipitation over a large majority of the SE US domains, especially the eastern coasts (Figure 6.1a). The further intensification of the summer precipitation variability can also be inferred from PDFs[2] of SE US precipitation constructed upon the ensemble of 24 CMIP5 models (Figure 6.1d). The future climatology of SE US summer precipitation shows insignificant changes because no apparent shift in the modes of Historical (1950-1999) and RCP4.5 (2050-2099) PDFs is found (Figure 6.1d). In contrast, the scale parameter[3] of RCP4.5 PDF increases significantly at $\alpha = 0.01$ level (χ^2 test) with both wet and dry tails of the PDF extend further (Figure 6.1d). Overall, the ensemble of CMIP5 models suggest that the increase in GHG concentrations will likely enhance SE

[2] The Log-Normal, Log-Pearson Type III, and Generalized extreme value – Type II distribution kernels have also been tested. For SE US summer precipitation, these distribution kernels do not show obvious advantage over the Gamma kernel, although they imply higher complexity. Most importantly, the precipitation PDFs constructed using these different kernels suggest the same changes in future precipitation over the SE US. Thus, only the results based on Gamma distribution kernel are discussed and presented here.

[3] The value of scale parameter determines the "statistical dispersion" of a PDF and thus reflects the tail behavior of the PDF. The large value of scale parameter indicates the sample distribution tends to be more spread, whereas the small value indicates the distribution is more concentrated.

US summer precipitation variability and result in more frequent occurrence of both dry and wet extremes in the future (Figure 6.1d).

Beside the ensemble of all CMIP5 models, we analyzed SE US summer precipitation simulated by G1 and G2 models (Section 4), separately. Increase in the summer precipitation variability shows a higher magnitude over the SE US by G1 models (Figure 6.1b) than the ensemble of all CMIP5 models (Figure 6.1a). Over large areas of the SE US, the increase in the standard deviation of summer precipitation exceeds 0.1 mm day^{-1} (Figure 6.1b). Furthermore, the G1 model ensemble suggests an increase in precipitation variability over the SE US and the feature is highly consistent among G1 models (Figure 6.1b). In contrast, there is no apparent shift of SE US summer precipitation variability as projected by G2 models. The scale parameters of the PDFs and thus the tail behavior of the summer precipitation remain almost unchanged from Historical to RCP4.5 scenarios (Figure 6.1f). G2 models show an east-west dipole pattern in the variability change, with the variability increase over the eastern coast but decrease in the west of the domain (Figure 6.1c).

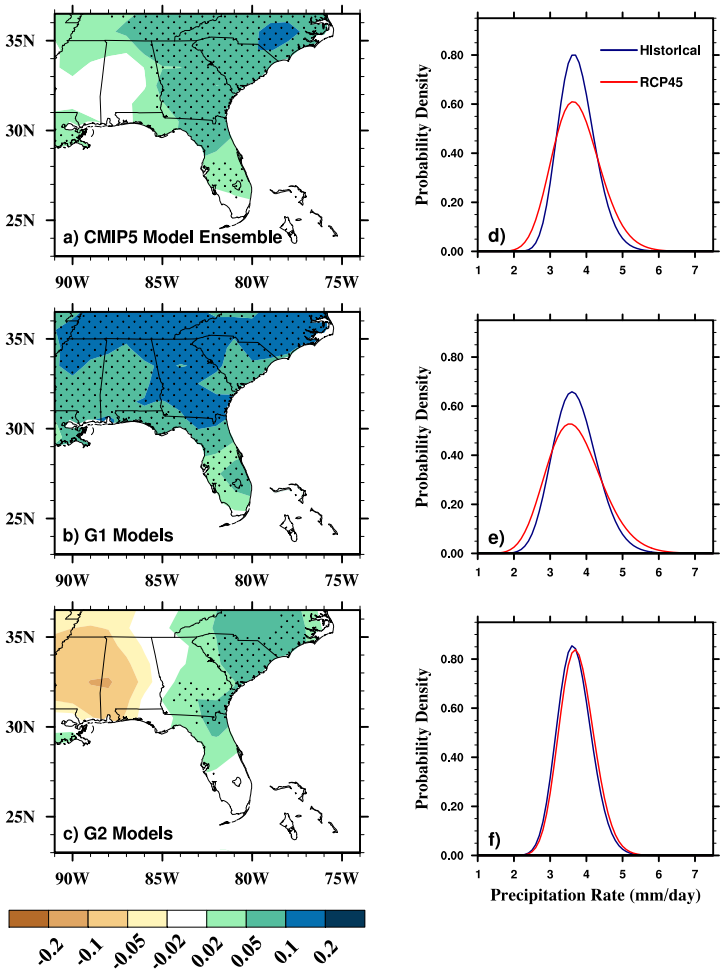

Figure 6. 1: Changes of the standard deviation in SE US summer precipitation from Historical to RCP4.5 scenarios (shaded, unit: mm day^{-1}) according to a) CMIP5 model ensemble; b) G1 models; and c) G2 models. Stippled are the areas with more than 70% models from each group suggesting the increase in precipitation standard deviation. The PDF curves constructed based on the quantile normalized SE US summer precipitation under Historical (blue) and RCP4.5 (red) scenarios are show as d) CMIP5 model ensemble; e) G1 models and f) G2 models.

6.1.2 Weighted ensemble projections

The projections of future precipitation over the SE US differ between G1 and G2 models (Figure 6.1). It suggests that the quality of GCMs in simulating current precipitation variability influences their projection of future climate in the SE US. Such a

dependence of model quality in projecting future climate has also been noticed in other regions (Li *et al.* 2008). Thus, a projection of future precipitation is made by applying weight function to CMIP5 models: models simulating precipitation variability closer to observations in the current climate are given higher weight in projecting future precipitation. The assumption is that "models simulating the current climate accurately will likely make a more reliable future projection". Such an assumption is physically sound, because the models' good simulations of SE US summer precipitation are related to their reasonable simulations of the underlying physical mechanism: the "NASH western ridge position – SE US summer precipitation" relationship (Figures 3.4 and 4.6).

In this study, a weight function, using *Normal* distribution kernel $\sim N\left(\mu,\sigma^2\right)$, is constructed based on model bias in simulating precipitation variability in the current climate. Here, the model bias is defined as the difference in the standard deviation of SE US summer precipitation between a model's simulation and observations. We adjusted the model bias to relative bias as follows:

$$bias_i = \frac{std_i - std_{obs}}{\left(\left|std_i - std_{obs}\right|\right)} \qquad (6.1),$$

where std_i is the standard deviation of the summer precipitation simulated by the i-th model and std_{obs} is the observed standard deviation of the summer precipitation. The denominator $\left(\overline{\left|std_i - std_{obs}\right|}\right)$ is the average of the absolute bias among 24 CMIP5 models.

In our analysis, μ is set to 0, meaning that the models with the same standard deviation as observations are treated as "perfect models" and are thus assigned the highest weight. The σ determines the strength of the weight function. Weight functions with small σ assigns disproportionally high weight to one or two "best" models, thus tends to over-emphasize certain individual models and not representative of the ensemble set. In contrast, the large σ tends to disperse the probability density. As σ increases to infinity, the Normal distribution approximates the Uniform distribution, and the weighted ensemble converges to equal-weighted ensemble results.

In our analysis, the determination of σ comes from a Monte-Carlo simulation. We draw 10000 σ samples evenly distributed between [0.1 10]. The model weight is calculated with each of the 10000 σ :

$$w_i = \frac{1}{\sqrt{2\pi}\sigma}\exp\left(-\frac{bias_i^2}{2\sigma^2}\right) \quad (6.2).$$

Optimal σ for the weight function is selected using the following criteria: 1) the weight assigned to the "best" model should not exceeds 20 times that assigned to the "worst" model; 2) after applying the weight function, the standard deviation of the Historical samples is closest to observations. According to the Monte-Carlo simulation, a weight function $w_i \sim N\left(0,1.22^2\right)$ is constructed.

The weight function is converted to be the sample size of each individual model. We assign 50 model samples to the "worst" model. The number of samples from the i-th model can then be calculated from:

$$\frac{w_i}{\min(w)} = \frac{n_i}{50} \quad (6.3).$$

We constructed a new precipitation sample set with n_i samples drawn from the i-th model. After applying the weight function (Equation 6.3), the standard deviation from the weighted Historical sample becomes 0.61 mm day^{-1} compared to 0.65 mm day^{-1} in observations. This weight function is also applied to future precipitation projection under RCP 4.5 scenario (Figure 6.2).

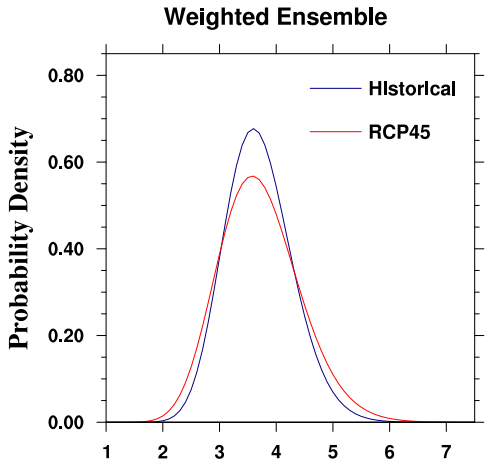

Figure 6. 2: PDF curves constructed based on SE US summer precipitation by taking into account qualities of CMIP5 models in simulating SE US summer precipitation variability. The weight function is $w_i \sim N(0,1.22^2)$. The blue (red) curve represents Historical (RCP4.5) scenarios.

The summer precipitation PDFs constructed while taking into account model quality weight are shown in Figure 6.2. Compared with equal-weighed ensemble PDFs

(Figure 6.1d), the RCP4.5 PDF tails extend further as suggested by the weighed ensemble (Figure 6.2). As the G1 models are assigned higher weight in the ensemble, the PDFs resemble those from G1 models (Figure 6.1e).

Overall, both the unweighted and weighted ensemble of CMIP5 models suggest that SE US summer precipitation variability would further intensify as GHG concentrations increase (Figures 6.1 and 6.2). The enhancement in the summer precipitation variability will likely drive the SE US towards a more "extreme" climate in the future. That is, as warming continues, more frequent occurrences of dry and wet summers are expected, leading to increased climate extremes over the SE US.

6.2 Causes of the intensified SE US summer precipitation variability

The analysis of observed atmospheric hydrological cycle over the Southeast suggests that the moisture transport (MT) process, especially that caused by seasonal mean circulation (MTM, $\nabla \cdot \int_0^{p_s} \overline{q}\overline{\vec{V}}\, dp$), is essential to SE US summer precipitation and its variability (Section 2). Furthermore, our study also shows that the MTM is also determines the skills of the "state-of-the-art" GCMs in representing the SE US summer precipitation variability (Li and Li 2014, submitted to Climate Dynamics). Here, we analyze the changes of MTM in the RCP4.5 scenario compared to the Historical run.

6.2.1 SE US summertime hydroclimate and its contribution to precipitation variance change in the future

Figure 6.3 shows the projection of future changes in SE US summer precipitation and MTM[4]. Changes in precipitation and MTM climatology show a dipole pattern, with precipitation and moisture convergence increasing over the eastern coasts, but decreasing westward (Figure 6.3a-b). Over the SE US, the projected changes in mean precipitation and MTM are too weak to pass the student t-test (Figure 6.3a-b). In contrast, the models consistently project a significant increase in summer precipitation variance ($\alpha = 0.05$ level by F-test) throughout the entire domain (Figure 6.3c). The increases in precipitation variance are most apparent along the eastern coast and are slightly weaker inland. The increase in precipitation variance and its spatial pattern are largely consistent with the projected MTM variance throughout the entire domain (Figure 6.3d). Such a consistency suggests that the changes in MTM processes might be responsible for the intensified precipitation variance over the SE US in a warming climate.

[4] The models used in Figure 6.3 are slightly different from those in Figure 6.1, because some models do not provide variables required by moisture budget analysis.

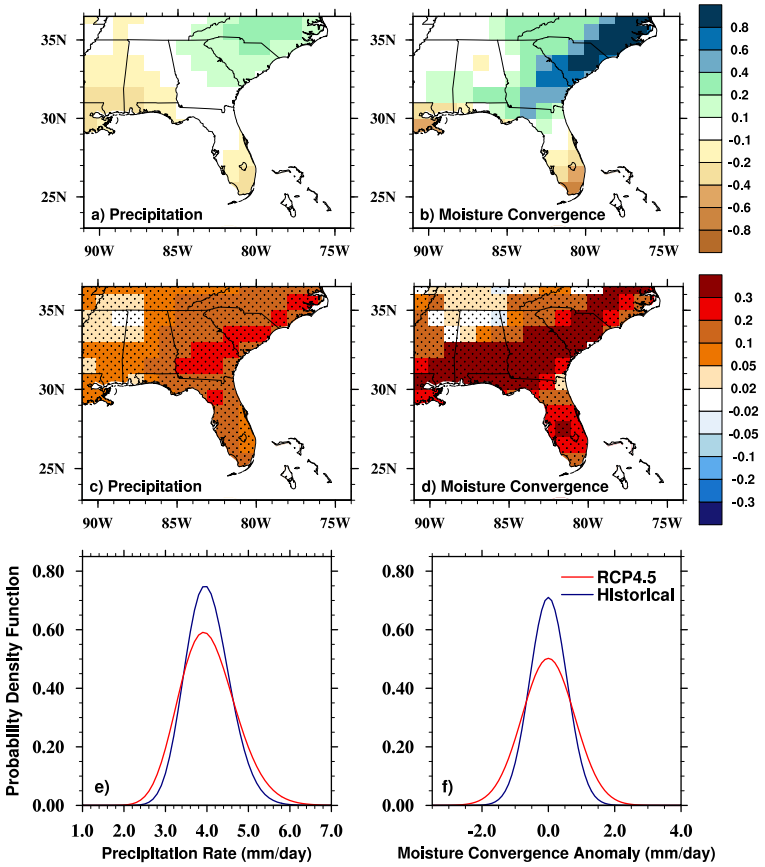

Figure 6. 3: Changes in the SE US summer of a) precipitation and b) MTM; and the variance of c) precipitation and d) MTM from Historical run (1950-1999) to RCP4.5 scenarios (2050-2099) (shaded, units: $mm^2\ day^{-2}$). The PDF curves constructed based on areal-averaged SE US summer precipitation and moisture convergence anomalies are shown in e) and f) respectively. In a) and b) (c) and d)), the grid points with changes significant at 0.05 level by t-test (F-test) are stippled.

Future changes in SE US summer precipitation and MTM can also be illustrated by the probability density functions (PDFs) of the areal-averaged precipitation and MTM. The Normal distribution is used to fit the moisture transport, while the Gamma distribution is used to fit the summer precipitation considering the non-negative constraint and the skewness of precipitation distribution.

The precipitation PDFs show no apparent shift in the mean under the RCP4.5 scenarios, whereas the variance increases significantly (Figure 6.3e), since the scale parameters increase at $\alpha = 0.01$ level. Both the dry and wet tails of the RCP4.5 PDF extend further, suggesting an intensification of precipitation variance in a warming climate (Figure 6.3e), consistent with Li *et al.* (2011) and Li *et al.* (2013a). The increases in SE US summer precipitation variance can be explained by the intensified variance in MTM (Figure 6.3f). Compared to the Historical simulations, increases in GHGs do not shift the modes of MTM PDFs at all, indicating the climatology of MTM likely remain the same in the future in the region (Figure 6.3f). In contrast, the tails of the RCP4.5 PDF extend, suggesting both the divergence and convergence of moisture flux will be enhanced in the future (Figure 6.3f). The intensified moisture divergence (convergence) over the SE US could lead to a deficit (excessive) in SE US summer precipitation, exacerbating drought (fluvial) conditions in a warming climate.

The similarities in the precipitation and MTM PDFs further emphasize the importance of MTM in regulating SE US summer precipitation variance in current and future climate. Overall, Figure 6.3 suggests that the variability of SE US summer precipitation would further intensify in the future (Figure 6.3c and 6.3e), which can be largely explained by the changes in MTM (Figure 6.3d and 6.3f).

6.2.2 Thermodynamic and dynamic contribution to the intensification of SE US summer precipitation variance in the future

The projections by CMIP5 models suggest that SE US summertime hydrological cycle will become more variable under the RCP4.5 scenarios. The variance of precipitation will significantly increase in a warming climate, which is tightly associated with an increased MTM variance. Previous studies suggest that both thermodynamics and dynamics can cause changes in hydrological cycle under warming scenarios (Held and Soden 2006; Huntington 2006; Li *et al.* 2012b; O'Gorman and Schneiderb 2009; Seager *et al.* 2010; Seager *et al.* 2012; Trenberth 2011). The contributions of atmospheric thermodynamics and dynamics to the intensified variance in SE US summer precipitation are assessed by applying the variance partition algorithm (Appendix B) to the MTM. The algorithm is based on the exchangeability theory (Hoff 2009) and is able to explicitly separate the thermodynamic and dynamic contributions to MTM variance change from one climate state to another (Li and Li 2014, submitted to Climate Dynamics). Generally, the algorithm can be summarized as the following (See detail in Appendix B):

$$\begin{aligned}
&\mathrm{var}\left(Y_{2\pi}\right)-\mathrm{var}\left(Y_{1\pi}\right)\\
&=\underbrace{\mathrm{var}\left(\nabla\cdot\int_0^{p_s}\Delta q_\pi\vec{V}_{1\pi}\,dp\right)}_{A}+\underbrace{2\,\mathrm{cov}\left(\nabla\cdot\int_0^{p_s}q_{1\pi}\vec{V}_{1\pi}\,dp,\nabla\cdot\int_0^{p_s}\Delta q_\pi\vec{V}_{1\pi}\,dp\right)}_{B}\\
&+\underbrace{\mathrm{var}\left(\nabla\cdot\int_0^{p_s}q_{1\pi}\Delta\vec{V}_{\pi}\,dp\right)}_{C}+\underbrace{2\,\mathrm{cov}\left(\nabla\cdot\int_0^{p_s}q_{1\pi}\vec{V}_{1\pi}\,dp,\nabla\cdot\int_0^{p_s}q_{1\pi}\Delta\vec{V}_{\pi}\,dp\right)}_{D}\\
&+\underbrace{2\,\mathrm{cov}\left(\nabla\cdot\int_0^{p_s}\Delta q_\pi\vec{V}_{1\pi}\,dp,\nabla\cdot\int_0^{p_s}q_{1\pi}\Delta\vec{V}_{\pi}\,dp\right)}_{E}
\end{aligned}\qquad (6.4).$$

Here, $Y_{1\pi}$ and $Y_{2\pi}$ are model simulated MTM in Historical run and RCP4.5 scenario, respectively. $q_{2\pi}$ ($q_{1\pi}$) and $\vec{V}_{2\pi}$ ($\vec{V}_{1\pi}$) are the model simulated specific humidity and wind fields under the RCP 4.5 scenarios (Historical runs) at each MTM quantile. $\Delta q_\pi = q_{2\pi} - q_{1\pi}$ and $\Delta \vec{V}_\pi = \vec{V}_{2\pi} - \vec{V}_{1\pi}$ represent the quantile-based thermodynamic and dynamic differences between RCP 4.5 scenarios and Historical runs, respectively. The left hand side of Equation (6.4) is the differences of MTM variance between Historical run and RCP4.5 scenario. On the right hand side, the thermodynamic and dynamic contributions to variance changes are quantified explicitly. Specifically, terms A and B (terms C and D) only involve the differences in specific humidity (wind), and thus reflect the thermodynamic (dynamic) contributions to variance changes. Term E involves both specific humidity and wind, and thus denotes the coupling between thermodynamic and dynamic processes.

By fixing $\Delta \vec{V}_\pi = 0$ (i.e., the dynamic components are kept at Historical level), the MTM variance change can only be introduced by thermodynamic terms (Terms A and B in Equation 6.4). Thus, the right hand side of Equation (6.4) can be simplified and the thermodynamically determined MTM variance can be expressed as:

$$\begin{aligned} \mathrm{var}\left(Y_{thm}\right) &\approx \mathrm{var}\left(Y_{1\pi}\right) + \mathrm{var}\left(\nabla \cdot \int_0^{p_s} \Delta q_\pi \vec{V}_{1\pi}\, dp\right) + 2\,\mathrm{cov}\left(Y_{1\pi}, \nabla \cdot \int_0^{p_s} \Delta q_\pi \vec{V}_{1\pi}\, dp\right) \\ &= \mathrm{var}\left(\nabla \cdot \int_0^{p_s} q_{2\pi} \vec{V}_{1\pi}\, dp\right) \end{aligned} \quad (6.5).$$

Similarly, by fixing $\Delta q_\pi = 0$, Terms C, D, and E in Equation (6.4) vanish, and the dynamic contributions to moisture transport variance can be expressed as:

$$\begin{aligned}\mathrm{var}\left(Y_{dyn}\right) &\approx \mathrm{var}\left(Y_{1\pi}\right)+\mathrm{var}\left(\nabla\cdot\int_0^{p_s} q_{1\pi}\Delta\vec{V}_{\pi}\,dp\right)+2\,\mathrm{cov}\left(Y_{1\pi},\nabla\cdot\int_0^{p_s} q_{1\pi}\Delta\vec{V}_{\pi}\,dp\right)\\ &=\mathrm{var}\left(\nabla\cdot\int_0^{p_s} q_{1\pi}\vec{V}_{2\pi}\,dp\right)\end{aligned} \quad (6.6).$$

Thermodynamic (Equation 6.5) and dynamic (Equation 6.6) contributions to the changes of MTM under RCP4.5 scenarios are compared by constructing PDFs using Y_{thm} and Y_{dyn}. The emphasis will be on the tail behavior of the thermodynamic and dynamic PDFs, since the variance of statistical samples is mainly reflected in the width of a distribution curve.

Figure 6.4 shows the PDFs constructed using Y_{thm} and Y_{dyn}. Compared to the MTM PDF in Historical experiment, both thermodynamic and dynamic PDFs show substantial extension of the distribution tails (Figure 6.4); this result suggests that both thermodynamics and dynamics contribute to the increased MTM variance over the SE US under the RCP 4.5 scenarios. Thus, unlike other regions, the changes in SE US summer precipitation variance are not purely thermodynamic responses of regional hydrological cycle to GHGs forcing.

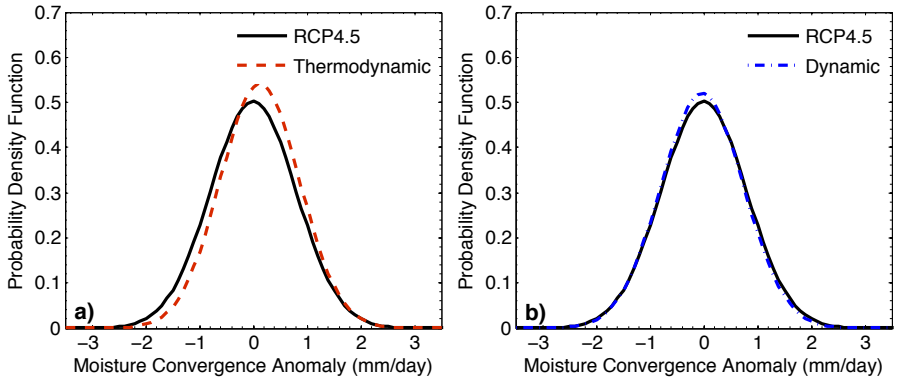

Figure 6. 4: The PDF curves of a) thermodynamic (red dashed curve) and b) dynamic components (blue dashed curve) of MTM over the SE US and their comparison with the RCP 4.5 PDF.

Specifically, the thermodynamics mainly contribute to the extension of the wet tails. Meanwhile, the mode of the thermodynamic PDF slightly shifts (although insignificant) towards increased convergence of moisture over the SE US (Figure 6.4a). The shift in the PDF is consistent with the thermodynamically driven changes in hydrological cycle, with the wet regions generally getting wetter in a warming climate (Allen and Ingram 2002; Chou *et al.* 2009; Held and Soden 2006). Over the SE US, the thermodynamic contributions can explain the more frequent and intensified wet summers as projected by CMIP5 models (Figures 6.1d-e, 6.2, and 6.3e), but fail to explain the extension of the divergence tails in the MTM PDFs and the enhancement of dry summers (Figures 6.3f and 6.4a).

In contrast, atmospheric dynamics explains the enhancement of both dry and wet summers in a warming climate, via its modulation of regional hydrological cycle (Figure

6.4b). Under the RCP4.5 scenarios, the tails of the dynamic PDFs extend towards stronger convergence and divergence of moisture in the Southeast, which closely resembles the PDF of the RCP4.5 MTM (Figure 6.4b). Compared to the thermodynamic PDFs, the dynamic contributions are particularly important in explaining future changes in summertime drought over this region (Figure 6.4). Synthetically, the changes in atmospheric dynamics exert a broader impact on the variance change of SE US regional hydrological cycle during summer seasons, which tend to result in both extremely dry and wet summers in the future.

6.3 Pattern shift of the NASH and its role in the intensified SE US summer precipitation variance

CMIP5 models collectively suggest that SE US summer precipitation will become more variable in the future as atmospheric GHG concentrations increase (Figures 6.1, 6.2, and 6.3). The intensified rainfall variability is tightly associated with the increased variance in MTM (Figure 6.3d and f). Furthermore, the MTM variance change is mainly caused by the changes in the large-scale circulation patterns, while the increases in atmospheric moisture content is secondary (Figure 6.4).

Previous studies have identified the NASH western ridge circulation as a primary dynamic regulator of SE US summer precipitation (Chapters 2 and 3). In recent decades, the intensified SE US summer precipitation variability has been attributed to the westward extension of the NASH western ridge and the increased occurrence of NW-

and SW-type ridge patterns (Figure 6.5a and Chapter 3). Thus, it is likely that the projected intensification of summer precipitation variance is due to changes in the NASH western ridge circulation, which dynamically intensifies the variance in MTM.

Future changes of the NASH are analyzed by comparing the 850hPa geopotential height under Historical and RCP4.5 scenarios. Simulations by G1 models are considered due to their capability to represent the observed "NASH western ridge – SE US summer precipitation" relationship (Chapter 3). As tropospheric temperature increases under the RCP4.5 scenario, the atmospheric layer at the 850hPa level tends to expand vertically and thus increases the geopotential height of the NASH system. However, the spatially uniform thermal expansion component does not contribute to wind (i.e. atmospheric dynamics) changes. In this study, the uniform thermal expansion of the high system has been removed from the 850hPa geopotential height (Appendix C). Thus, the results have mainly dynamical implications for future climate.

In a warming climate, G1 models suggest that the western ridge would extend westward into the US continent, dynamically (Figure 6.5b). From Historical to RCP4.5 scenarios, the western ridge extends westward by about 5° (Figure 6.5b) and the westward extension is highly consistent among G1 models. The westward movement of the NASH western ridge could alter the prevailing wind and moisture transport over the SE US, indicating a more important influence of NASH on SE US summer precipitation in the future (Li *et al.* 2012a; Li *et al.* 2011).

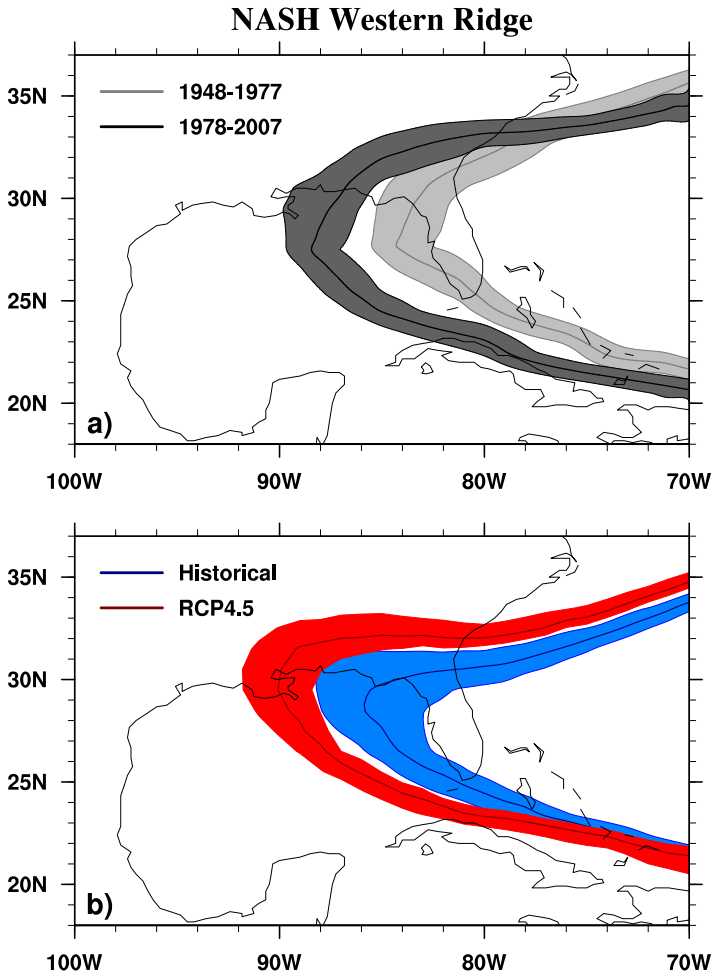

Figure 6. 5: Climatolgy of NASH western ridge a) calculated from NCEP/NCAR reanalysis, with dark (light) gray curve represents the 1948-1977 (1978-2007) period; b) simulated by the G1 models under Historical (blue curve, 1950-1999) and RCP4.5 (red curve, 2050-2099) scenarios. The geopotential height isoline straddling 86°W under the Historical scenario is chosen to represent the NASH western ridge in each model. Shaded areas represent the 95% confidence interval of the western ridge climatology.

Accompanying the westward movement of the NASH western ridge, the frequencies of both NW and SW-type ridges would increase. According to the simulations by G1 models, the NW-type ridges are projected to increase by 10% and the

SW-type ridges triple under the RCP4.5 scenario compared to Historical scenario (Figure 6.6). The northwestward movement of the NASH western ridge could further suppress upward motion over the SE US due to the prevailing descending motion south of the western ridge (Li *et al.* 2012a; Liu and Wu 2004). In contrast, as the ridge extends further southwestward, the moisture flux would more likely converge into the SE US and favor heavier summer precipitation (Li *et al.* 2012a). Thus, the intensity of abnormally dry and wet summers could increase over the SE US.

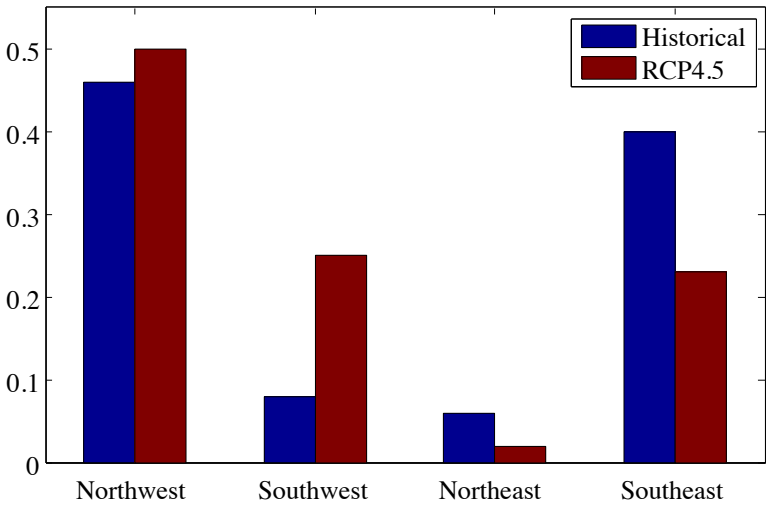

Figure 6. 6: Occurrence rate of the 4 ridge types under Historical (blue bar) and RCP4.5 (red bar) scenarios as suggested by G1 models.

Collectively, the NASH western ridge pattern changes could lead to the projected increase in SE US summer precipitation variability. In the future, as the NASH western ridge moves westward (Figure 6.5b) and its occurrence in the NW and SW position

increases more frequently (Figure 6.6), more summers with enhanced flood/drought intensity would likely occur over this region.

6.4 Summary and Conclusions

The frequency and severity of extreme events, such as drought and floods, are tightly associated with the variance of regional precipitation (Katz and Brown 1992). This study analyzes the future changes in summer precipitation variance over the SE US using CMIP5 GCMs. The model ensembles consistently project an intensification of SE US summer precipitation variance in the future as GHG concentrations continue to increase. Specifically, the intensification of summer precipitation variance is statistically significant over the entire domain, and is highly consistent among projections using unweighted ensemble, weighted ensemble, and G1 model ensemble. Thus, the future intensification of summer precipitation variance is a robust regional climate change feature over the SE US. As a result, more frequent and severe extreme events tend to be experience in the future (Wuebbles *et al.* 2013).

The projected increase in SE US summer precipitation variance might be caused by a higher variance of MTM in a warming climate. Furthermore, according to the variance partition algorithm, the increased MTM and precipitation variance might result from a combined thermodynamic and dynamic effect, with the latter being more important. Specifically, the thermodynamic contributions are manifested in the enhancement of

moisture convergence and the intensification of wet summers. However, thermodynamics alone cannot explain the projected enhancement in summer drought, suggesting that the variance changes in SE US summertime hydrological cycle is not a purely thermodynamic response to GHG forcing. In contrast, changes in atmospheric dynamics, i.e., the future changes in large-scale circulation, result in the intensification of both wet and dry summers, indicating that the dynamics explains a more complete spectrum of future changes in SE US summertime hydrological cycle. Thus, the dynamic processes should be emphasized in order to better understand the changes in SE US summertime hydrological cycle, especially the intensification of summer drought.

The projected precipitation changes are linked to the pattern shifts of the NASH western ridge in a warming climate. In the future, the western ridge is expected to extend further westward, when both the frequency and magnitude of NW and SW ridges are expected to increase. According to the "NASH western ridge – SE US summer precipitation" relationship, the SE US will likely experience more floods and droughts during future summers.

7. Conclusions

Warm-season precipitation plays an increasingly more important role in hydrology, ecology, and agriculture over the SE US (Manuel 2008; Martinez *et al.* 2009; Riha *et al.* 1996). In recent decades, summer rainfall extremes have become more frequent and severe over this region (Douglas and Barros 2002), due mainly to the increased rainfall precipitation variability (Katz and Brown 1992; Li *et al.* 2011; Wang *et al.* 2010). Therefore, there is a pressing need to understand the causes of the intensification of summer precipitation variability over this region.

This dissertation investigates the mechanisms responsible for the variability of SE US summer precipitation. First, physical processes in relation to SE US summer precipitation variability is analyzed by performing the regional moisture budget (Chapter 2). Using multiple reanalysis datasets, the analysis show that moisture transport (MT), especially the MT by seasonal mean circulation (MTM), is the primary driver of summer precipitation variability over the SE US. Furthermore, most MTM variance (90%) is explained by the atmospheric dynamics, i.e., the large-scale circulation.

In the summer, the North Atlantic Subtropical High (NASH) is the predominant large-scale circulation systems governing the climate over the North America. By dynamically modulating moisture transport into the SE US, the spatial movement of the NASH western ridge significantly influences SE US summer precipitation (Chapter 3). It is shown that when the ridge is located in a Northwestward (NW) position, the moisture

tends to be deviated from the SE US and the downward motion dominates. Thus, dry summers tend to occur over this region. In contrast, when the ridge is located in a Southwestward (SW) position, more moisture tends to converge over the SE US, resulting in wet summers. However, as the ridge is located in a relatively eastward, its influence on SE US summer precipitation weakens. In recent decades, the NASH western ridge has extended westward towards the US continent (Li *et al.* 2011). Consequently, both NW- and SW-type ridges have increased, leading to increases in both dry and wet summers and thus enhanced summer precipitation variability over this region (Wang *et al.* 2010). Further analysis of circulation dynamics show that the SW-type ridge is mainly caused by the intensification of the NASH center and its formation involves air-sea coupling over the tropical oceans. Whereas, the NW-type is more likely caused by the propagation of stationary waves induced by PDO SSTA forcing (Li *et al.* 2012a).

The observational-based studies in Chapter 3 establish a "NASH western ridge – SE US summer precipitation" relationship, which depict the first-order dynamics control on regional precipitation in the Southeast (Li *et al.* 2012a; Wuebbles *et al.* 2013). Furthermore, such a relationship provides a process-level control on the simulation skill of SE US summer precipitation by both general circulation models (GCMs) and regional climate models (RCMs). In Chapter 4, the performance of the state-of-the-art GCMs and RCMs in simulating SE US summer precipitation is evaluated. It is shown that the

capability to representing the "NASH western ridge – SE US summer precipitation" relationship largely determines GCM skills in simulating SE US summer precipitation variability (Chapter 4). In addition, the RCM bias in SE US summer precipitation is also attributable to the errors in the simulated NASH western ridge circulation (Chapter 4). In RCM sensitivity experiments using Weather Research and Forecasting (WRF) model, we noticed that without an accurate simulation of the NASH western ridge circulation, switching physical parameterization schemes could not effectively improve the rainfall simulation over the SE US (Chapter 4).

By providing a realistic NASH western ridge circulation in WRF, the model's simulation on SE US summer precipitation becomes sensitive to the choice of physical parameterization schemes (Chapter 5). Specifically, WRF simulations of SE US summer precipitation are most sensitive to the choice of cumulus schemes. Among five of the cumulus schemes provided by WRF, the Zhang-McFarlane (Zhang and McFarlane 1995) generates the highest skill in simulating the summer precipitation. The superior performance of this scheme is attributable to its capability in capture the positive relationship between local convective available potential energy (CAPE) and rainfall. Our study suggests that in order to achieve to satisfactory WRF skill in simulating SE US summer precipitation the Zhang-McFarlane scheme should be applied along with the accurate NASH western ridge circulation.

Based on the analysis of SE US summer precipitation in the current climate, the future precipitation changes is projected using the simulations by phase 5 of the Coupled Model Intercomparison Project (CMIP5) GCMs (Chapter 6). The ensemble of CMIP5 models suggests that future precipitation will be more variable over the SE US, due mainly to the enhanced variance in MTM processes. According to the variance partition algorithm (Appendix B), the enhanced MTM variance results from a combined thermodynamic and dynamic effect. On the one hand, the increases in atmospheric moisture content enhance the MTM variance and mainly causes increased occurrence of wet summers. On the other hand, the changes in atmospheric dynamics explain the projected increase of both dry and wet summers. Synthetically, the dynamics is more important than thermodynamics in enhancing the variability of SE US summer precipitation through the MTM processes. The changes in atmospheric dynamics are consistent with the pattern shifts of the NASH western ridge in a warming climate. In the future, the NASH system tends to intensify and expand and the NASH western ridge will extend further westward into the US continent. As a result, more NW- and SW- type ridges are expected in a warming climate. According to the "NASH western ridge – SE US summer precipitation" relationship, more extremely wet and dry summers will be observed over the SE US in the future.

Appendix A

Pattern identification method to selection WRF simulation periods

The focus of this study is the dynamical downscaling skills of WRF to simulate SE US summer rainfall from a climate perspective. Previous studies have suggested that WRF simulation results vary among weather events (Bukovsky and Karoly 2009). Thus, the simulation period should be determined objectively to avoid the uncertainties introduced by specific weather events.

In this study, our simulations are focused on a one-summer period in which the precipitation pattern for the SE US mimics its climatology during 1948-2010. To identify such a summer period, we calculate the pattern correlation coefficient (PCC) and root mean square error (RMSE) between the precipitation pattern of each summer and its climatology during 1948-2010. An optimization algorithm is then applied to select the sample rainfall case for the WRF simulation. In this algorithm, the PCC (RMSE) calculated for each summer is ranked from high to low (low to high). The final rank for each summer period is calculated by combining the PCC and RMSE ranks. The period with the highest combined rank is then selected as the sample case for the WRF sensitivity experiment.

The averaged rainfall during any specific period with a running window of l days is expressed as x, and the 1948-2010 JJA rainfall climatology is expressed as y. The PCC

and RMSE are defined in Equation A1 and A2, respectively. In both equations, N is the number of grid points over the SE US domain. The PCC and RMSE are calculated with various running window lengths (l): 7-day, 11-day, 15-day, 21-day, and 31-day.

$$PCC(l) = \frac{\sum_{i=1}^{N}\left[\left(x(l)_i - \overline{x(l)}\right)\left(y_i - \overline{y}\right)\right]}{\left[\sum_{i=1}^{N}\left(x(l)_i - \overline{x(l)}\right)^2\right]^{\frac{1}{2}}\left[\sum_{i=1}^{N}\left(y_i - \overline{y}\right)^2\right]^{\frac{1}{2}}} \quad \text{(A1);}$$

$$RMSE(l) = \left[\frac{1}{N}\sum_{i=1}^{N}\left(x(l)_i - y_i\right)^2\right]^{\frac{1}{2}} \quad \text{(A2).}$$

Figure A1a shows the averaged PCC versus the running window length. As the window length increases, the PCC increases, indicating that rainfall with increased temporal scales better resembles the climatological pattern. Statistically, this result suggests that rainfall averaged over a short period (< 10 days) may not well represent a climatological pattern. Thus, good simulation of a specific rainfall event by WRF is not sufficient to ascertain its ability to simulate rainfall climatology, which is consistent with Bukovsky and Karoly (2009). The increased PCC, however, gradually saturates as the running window increases to 15 days (Figure A1a). From the 7-day to the 15-day running windows, the averaged PCC increases from 0.68 to 0.77, whereas as the window continues to increase to 31 days, the PCC increases only slightly, by 0.04 (Figure A1a). The PCC results suggest that the 15-day window should be sufficient to obtain a reasonable climate simulation over the SE US; thus we chose a cut-off window of 15

days. A 15-day rainfall case would be selected for WRF simulation using the aforementioned optimization algorithm.

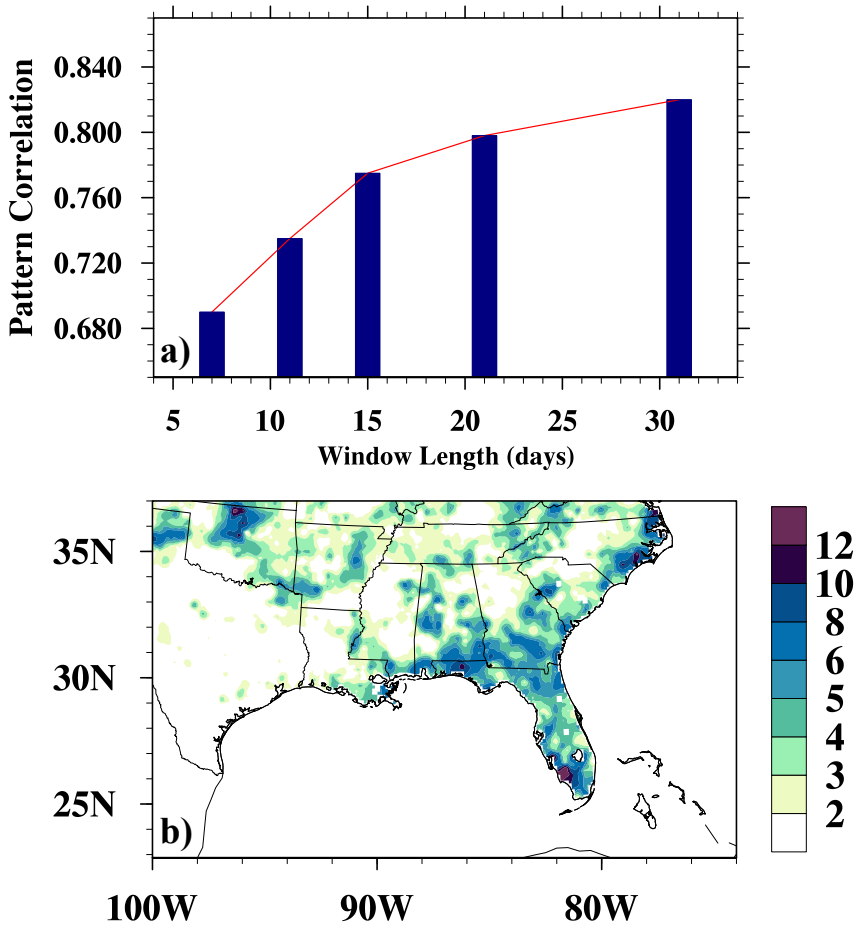

Figure A. 1: a) Maximum likelihood estimation of pattern correlation coefficients between running averaged precipitation and CPC SE US summer precipitation climatology (blue bars). The x-axis is the length of the running window, and the y-axis is the pattern correlation coefficients; b) SE US precipitation averaged over Aug. 01 ~ 15, 2009 (shaded, unit: mm day^{-1}).

Over 1948-2010, we finally select the period of Aug. 01 ~ Aug. 15, 2009 (Figure A1b), for the sensitivity simulation period with the highest combined rank. All sensitivity experiments are performed using this sample period. The robustness of the conclusions

from the sensitivity experiments is confirmed using a 10-summer (2001-2010) simulation. It is noteworthy that the optimization algorithm is designed to select a best representative case of rainfall climatology, rather than that of an extreme event such as a drought or flooding event. Thus, the conclusions in this study apply mainly to the WRF simulation of mean rainfall over the SE US for summer. Different metrics are needed to evaluate extreme rainfall events, which is beyond the scope of this study.

Appendix B

Variance partition algorithm

The analysis of the observed SE US summertime hydrological cycle indicates that the variance of SE US summer precipitation can largely be explained by the seasonal mean component of moisture transport (MTM) (Chapter 2). The MTM variance, in turn, is determined by the combined contributions from thermodynamic (specific humidity) and dynamic (wind) factors. However, quantification of thermodynamic and dynamic contributions to MTM variance is difficult, because sample variance reflects the second moment of the statistical samples, which is intrinsically more complicated than the sample mean. Specifically, the changes of MTM variance are not only caused by the changes in the variance of thermodynamic and dynamic factors, but also by the changes in the mean states of thermodynamics and dynamics, as well as their covariance. The multiple contributing factors make it hard to diagnose the processes/factors key to the variance change. Previous studies on the partition of hydroclimatic variance change are based on strict assumptions, including that ENSO explains the majority of the variance of hydrological cycle (Seager *et al.* 2012). For seasons or regions where ENSO's influence is weak, the assumption will be violated and the variance change mechanism cannot be easily diagnosed.

This study develops a novel algorithm, which requires no prior assumptions, to explicitly quantify the thermodynamic and dynamic contributions to variance changes

of regional hydrological cycle. According to the definition of sample variance: $\mathrm{var}(Y)=\frac{1}{n-1}\sum_{i=1}^{n}\left(y_i-\frac{1}{n}\sum_{i=1}^{n}y_i\right)^2$, no information regarding data alignment is needed to calculate sample variance (DeGroot and Schervish 2011; Hoff 2009). Utilizing such a satistical property, the algorithm is formulated as following.

Let Y_1 denote a n-yr such as 50-yr MTM time series in climate state 1, and Y_2 in climate state 2 (i.e., Y_1 and Y_2 are column vectors).

Step 1) Permute both Y_1 and Y_2 so that $y_{\pi\_1}\le y_{\pi\_2}\le ...\le y_{\pi\_50}$. Here, the subscript π denotes the time series after permutation, while the number $i\in\{1,2,...,50\}$ in the subscript denotes the i-th element of the time series. After the permutation, the year with the strongest moisture convergence is ranked the first, while that with the strongest moisture divergence is ranked the last. The sample variance calculated from the permutated time series remains the same as that from the original time series without permutation. However, the quantification of thermodynamic and dynamic contributions to the variance changes can be simplified.

Step 2) Identify specific humidity (thermodynamics) and wind (dynamics) corresponding to each MTM quantile in climate state 1 and 2: $Y_{1\pi}=\nabla\cdot\int_0^{p_s}q_{1\pi}\vec{V}_{1\pi}\,dp$ and $Y_{2\pi}=\nabla\cdot\int_0^{p_s}q_{2\pi}\vec{V}_{2\pi}\,dp$ are column vectors with 50 elements (i.e. samples from the 50-yr

time series). The i-th element corresponding to the i-th quantile of the MTM are $Y_{1\pi\_i} = \nabla \cdot \int_0^{p_s} q_{1\pi\_i} \vec{V}_{1\pi\_i}\, dp$ and $Y_{2\pi\_i} = \nabla \cdot \int_0^{p_s} q_{2\pi\_i} \vec{V}_{2\pi\_i}\, dp$, respectively.

Step 3) Calculate the quantile differences of specific humidity (thermodynamics) and wind (dynamics) between climate state 1 and state 2: $\Delta q_\pi = q_{2\pi} - q_{1\pi}$; $\Delta \vec{V}_\pi = \vec{V}_{2\pi} - \vec{V}_{1\pi}$, with the changes of the thermodynamic and dynamic components in the i-th quantile being $\Delta q_{\pi\_i} = q_{2\pi\_i} - q_{1\pi\_i}$ and $\Delta \vec{V}_{\pi\_i} = \vec{V}_{2\pi\_i} - \vec{V}_{1\pi\_i}$, respectively.

The variance of MTM in state 2 can be expressed as:

$$\mathrm{var}\left(Y_{2\pi}\right) = \mathrm{var}\left(\nabla \cdot \int_0^{p_s} q_{1\pi} \vec{V}_{1\pi}\, dp + \nabla \cdot \int_0^{p_s} \Delta q_\pi \vec{V}_{1\pi}\, dp + \nabla \cdot \int_0^{p_s} q_{1\pi} \Delta \vec{V}_\pi\, dp + \nabla \cdot \int_0^{p_s} \Delta q_\pi \Delta \vec{V}_\pi\, dp\right) \quad (1)$$

Generally, the Δq_π and $\Delta \vec{V}_\pi$ are small deviations from $q_{1\pi}$ and $\vec{V}_{1\pi}$, after the permutation[17]. Thus the term $\nabla \cdot \int_0^{p_s} \Delta q_\pi \Delta \vec{V}_\pi\, dp$ can be neglected, and Eq. 1 can be simplified as:

$$\mathrm{var}\left(Y_{2\pi}\right) \approx \mathrm{var}\left(\nabla \cdot \int_0^{p_s} q_{1\pi} \vec{V}_{1\pi}\, dp + \nabla \cdot \int_0^{p_s} \Delta q_\pi \vec{V}_{1\pi}\, dp + \nabla \cdot \int_0^{p_s} q_{1\pi} \Delta \vec{V}_\pi\, dp\right) \quad (2)$$

Step 4) Partition Eq. 2 using the statistical relationship that $\mathrm{var}(a+b+c) = \mathrm{var}(a) + \mathrm{var}(b) + \mathrm{var}(c) + 2\,\mathrm{cov}(a,b) + 2\,\mathrm{cov}(a,c) + 2\,\mathrm{cov}(b,c)$, where $\mathrm{cov}(a,b)$ is the covariance operator:

---

[17] Before permutation, $\nabla \cdot \int_0^{p_s} \Delta q \Delta \vec{V}\, dp$ cannot be neglected, because, due to the randomness of climate variability, Δq and $\Delta \vec{V}$ is not necessarily a small deviation from the original climate state. Thus, permutation is needed to separate the thermodynamic and dynamic contributions the covariance terms.

$$
\begin{aligned}
&\mathrm{var}\left(\nabla\cdot\left[\int_0^{p_s} q_{1\pi}\vec{V}_{1\pi}\,dp+\int_0^{p_s}\Delta q_\pi\vec{V}_{1\pi}\,dp+\int_0^{p_s} q_{1\pi}\Delta\vec{V}_\pi\,dp\right]\right)\\
&=\mathrm{var}\left(\nabla\cdot\int_0^{p_s} q_{1\pi}\vec{V}_{1\pi}\,dp\right)+\mathrm{var}\left(\nabla\cdot\int_0^{p_s}\Delta q_\pi\vec{V}_{1\pi}\,dp\right)+\mathrm{var}\left(\nabla\cdot\int_0^{p_s} q_{1\pi}\Delta\vec{V}_\pi\,dp\right)\\
&+2\,\mathrm{cov}\left(\nabla\cdot\int_0^{p_s} q_{1\pi}\vec{V}_{1\pi}\,dp,\nabla\cdot\int_0^{p_s}\Delta q_\pi\vec{V}_{1\pi}\,dp\right)\\
&+2\,\mathrm{cov}\left(\nabla\cdot\int_0^{p_s} q_{1\pi}\vec{V}_{1\pi}\,dp,\nabla\cdot\int_0^{p_s} q_{1\pi}\Delta\vec{V}_\pi\,dp\right)\\
&+2\,\mathrm{cov}\left(\nabla\cdot\int_0^{p_s}\Delta q_\pi\vec{V}_{1\pi}\,dp,\nabla\cdot\int_0^{p_s} q_{1\pi}\Delta\vec{V}_\pi\,dp\right)
\end{aligned}
\tag{3}
$$

In Eq. 3, $\mathrm{var}\left(\nabla\cdot\int_0^{p_s} q_{1\pi}\vec{V}_{1\pi}\,dp\right)=\mathrm{var}\left(Y_{1\pi}\right)$, thus,

$$
\begin{aligned}
&\mathrm{var}\left(Y_{2\pi}\right)-\mathrm{var}\left(Y_{1\pi}\right)\\
&=\underbrace{\mathrm{var}\left(\nabla\cdot\int_0^{p_s}\Delta q_\pi\vec{V}_{1\pi}\,dp\right)}_{A}+\underbrace{2\,\mathrm{cov}\left(\nabla\cdot\int_0^{p_s} q_{1\pi}\vec{V}_{1\pi}\,dp,\nabla\cdot\int_0^{p_s}\Delta q_\pi\vec{V}_{1\pi}\,dp\right)}_{B}\\
&+\underbrace{\mathrm{var}\left(\nabla\cdot\int_0^{p_s} q_{1\pi}\Delta\vec{V}_\pi\,dp\right)}_{C}+\underbrace{2\,\mathrm{cov}\left(\nabla\cdot\int_0^{p_s} q_{1\pi}\vec{V}_{1\pi}\,dp,\nabla\cdot\int_0^{p_s} q_{1\pi}\Delta\vec{V}_\pi\,dp\right)}_{D}\\
&+\underbrace{2\,\mathrm{cov}\left(\nabla\cdot\int_0^{p_s}\Delta q_\pi\vec{V}_{1\pi}\,dp,\nabla\cdot\int_0^{p_s} q_{1\pi}\Delta\vec{V}_\pi\,dp\right)}_{E}
\end{aligned}
\tag{4}.
$$

The left hand side of Eq. 4 is the differences of MTM variance between climate state 1 and state 2. On the right hand side, the thermodynamic and dynamic contributions to variance changes are quantified explicitly. Specifically, terms A and B (terms C and D) only involve the differences in specific humidity (wind), and thus reflect the thermodynamic (dynamic) contributions to variance changes. Term E involves both specific humidity and wind, and thus denotes the coupling between thermodynamic and dynamic processes.

Eq. 4 partitions the difference in MTM variance between two climate states (such as the 20th and 21st century climate) into those resulting from thermodynamic components

(terms A and B), dynamic components (terms C and D), and their coupling processes (term E). Thus, it can be implemented to diagnose thermodynamic and dynamic contributions to the changes in MTM variance in future climate. This algorithm can also be implemented to evaluate GCM simulations of MTM variance by comparing model simulations with the reanalysis ensemble.

It is noteworthy that this algorithm utilizes the general rule of sample variance calculation, and requires no additional assumptions about statistical samples. Thus, the algorithm can be applied to any region and/or any season to diagnose the variance changes in regional hydroclimate. In this study, this algorithm is applied to SE US summertime hydroclimate to 1) provide a process-level evaluation of CMIP5 model skill in simulating the variance of SE US summer precipitation, and 2) quantify the thermodynamic and dynamic contributions to MTM and precipitation variance change in a warming climate in order to understand the mechanisms responsible for future changes in hydroclimatic variance.

Appendix C

Removal of the contribution of thermal expansion to 850hPa geopotential height in a warming climate

Under the approximation of hydrostatic balance, the thickness of an atmospheric layer bounded by two isobaric surfaces is proportional to the mean temperature in the layer, i.e., $Z_2 - Z_1 = -\frac{R}{g}\int_{P_1}^{P_2} T\, d\ln P$, where Z is the geopotential height, T is atmospheric temperature in K, $R = 287 J \cdot kg^{-1} \cdot K^{-1}$ is the gas constant, and $g = 9.8 m \cdot s^{-2}$ is the gravitational acceleration.

At a latitude-longitude location, setting P_2 to 850hPa and P_1 to sea level pressure (SLP), Z_2 corresponds to the geopotential height at 850hPa and $Z_1 = 0$. The pressure-height relationship can be applied to infer the 850hPa geopotential height given the information of SLP and temperature distribution from the sea level to 850hPa:

$$Z_{850} = \frac{R\langle T\rangle}{g}\ln\left(\frac{SLP}{850hPa}\right) \quad \text{(A1)},$$

where $\langle T\rangle \ln\left(\frac{SLP}{850hPa}\right) = \int_{850hPa}^{SLP} T\, d\ln P$.

The pressure-height relationship indicates that the increase of temperature from surface to 850hPa would increase the geopotential height even though SLP remains unchanged. This relationship is applicable to the geopotential height field change in the RCP4.5 scenario where the increase in GHGs warms the lower troposphere, thermally expanding the atmospheric layer beneath 850hPa and thus increases 850hPa

geopotential. The contribution of temperature increase to geopotential height change in RCP4.5 is analyzed as:

$$\delta Z_{850} = \delta\left(\frac{R\langle T\rangle}{g}\ln\left(\frac{SLP}{850hPa}\right)\right) \quad \text{(A2)},$$

where $\delta = RCP4.5 - Historical$, and (A2) can be further partitioned into the thermal direct (temperature change) and thermal indirect (SLP change) components as:

$$\delta Z_{850} \approx \underbrace{\frac{R}{g}\delta\langle T\rangle\ln\left(\frac{SLP}{850hPa}\right)}_{\text{thermal direct}} + \underbrace{\frac{R\langle T\rangle}{g}\frac{\delta SLP}{SLP}}_{\text{thermal indirect}} \quad \text{(A3)}.$$

The warming of the lower troposphere over the North Atlantic and its contribution to the increase in Z_{850} are estimated by calculating the areal-averaged (100°W-20°W, 15°N-45°N) thermal direct term in Eq. A3. This uniform expansion component is subtracted from the RCP4.5 geopotential height field. From our calculation, this uniform expansion term substantially varies among CMIP5 models, ranging from 6-gpm to 21-gpm.

References

AchutaRao, K. M., and K. R. Sperber, 2006: ENSO simulation in coupled ocean-atmosphere models: Are the current models better? *Clim. Dyn.*, 27, 1-15.

Adams, D. K., and A. C. Comrie, 1997: The North American monsoon. *Bull. Amer. Meteor. Soc.*, 78, 2197-2213.

Adams, D. K., and E. P. Souza, 2009: CAPE and convective events in the Southwest during the North American monsoon. *Mon. Wea. Rev.*, 137, 83-98.

Alapaty, K., and Coauthors, 2012: Introducing subgrid-scale cloud feedbacks to radiation for regional meteorological and climate modeling. *Geophys. Res. Lett.*, 39, L24809.

Allen, M. R., and W. J. Ingram, 2002: Constraints on future changes in climate and the hydrologic cycle. *Nature*, 419, 224-232.

Anchukaitis, K. J., M. N. Evans, A. Kaplan, E. A. Vaganov, M. K. Hughes, H. D. Grissino-Mayer, and M. A. Cane, 2006: Forward modeling of regional scale tree-ring patterns in the southeastern United States and the recent influence of summer drought. *Geophys. Res. Lett.*, 33, L04705.

Anderson, B. T., A. C. Ruane, J. O. Roads, and M. Kanamitsu, 2009: Estimating the influence of evaporation and moisture-flux convergence upon seasonal precipitation rates. Part II: analysis for North America based on NCEP-DOE reanalysis II model. *J. Hydrometeor.*, 10, 893-911.

Arakawa, A., 2004: The cumulus parameterization problem: Past, present, and future. *J. Climate*, 17, 2493-2525.

Atallah, E., L. F. Bosart, and A. R. Aiyyer, 2007: Precipitation distribution associated with landfalling tropical cyclones over the Eastern United States. *Mon. Wea. Rev.*, 135, 2185-2206.

Baigorria, G. A., J. W. Jones, and J. J. O'Brien, 2007: Understanding rainfall spatial variability in southeast USA at different timescales. *Int. J. Climatol.*, 27, 749-760.

Barlow, M., 2011: Influence of hurricane-related activity on North American extreme precipitation. *Geophys. Res. Lett.*, 38, L04705.

Barlow, M., S. Nigam, and E. H. Berbery, 2001: ENSO, Pacific Decadal Variability, and U.S. summertime precipitation, drought, and stream flow. *J. Climate*, 14, 2105–2128.

Barros, A. P., and G. J. Bowden, 2008: Toward long-lead operational forecasts of drought: an experimental study in the Murray-Darling River Basin. *J. Hydrol.*, 357, 349-367.

Bielli, S., and R. Roca, 2010: Scale decomposition of atmospheric water budget over West Africa during the monsoon 2006 from NCEP/GFS analyses. *Clim. Dyn.*, 35, 143-157.

Black, R. X., 1997: Deducing anomalous wave source regions during the life cycles of persistent flow anomalies. *J. Atmos. Sci.*, 54, 895-907.

Boberg, F., P. Berg, P. Thejll, W. J. Gutowski, and J. H. Christensen, 2010: Improved confidence in climate change projections of precipitation further evaluated using daily statistics from ENSEMBLES models. *Clim. Dyn.*, 35, 1509-1520.

Bolstad, B. M., R. A. Irizarry, M. Åstrand, and T. P. Speed, 2003: A comparison of normalization methods for high density oligonucleotide array data based on variance and bias. *Bioinformatics*, 19, 185-193.

Booth, R. K., J. E. Kutzbach, S. C. Hotchkiss, and R. A. Bryson, 2006: A reanalysis of the relationship between strong westerlies and precipitation in the Great Plains and Midwest regions of North America. *Climatic Change*, 76, 427-441.

Bougeault, P., and P. LaCarrere, 1989: Parameterization of orography-induced turbulence in a mesobeta-scale model. *Mon. Wea. Rev.*, 117, 1871–1890.

Bowden, J. H., C. G. Nolte, and T. L. Otte, 2013: Simulating the impact of the large-scale circulation on the 2-m temperature and precipitation climatology. *Clim. Dyn.*, 40, 1903-1920.

Brubaker, K. L., D. Entekhabi, and P. S. Eagleson, 1993: Estimation of continental precipitation recycling. *J. Climate*, 6, 1077-1089.

Bukovsky, M. S., and D. J. Karoly, 2009: Precipitation simulations using WRF as a nested regional climate model. *J. Appl. Meteor. Climatol.*, 48, 2152-2159.

Case, J. L., M. M. Wheeler, J. Manobianco, J. W. Weems, and W. P. Roeder, 2005: A 7-yr climatological study of land breezes over the Florida spaceport. *Journal of Applied Meteorology*, 44, 340-356.

Castro, C. L., R. A. P. Sr, and G. Leoncini, 2005: Dynamical downscaling: Assessment of value retained and added using the Regional Atmospheric Modeling System (RAMS). *J. Geophys. Res. Atmos.*, 110, D05108.

Cayan, D. R., 1992: Latent and sensible heat flux anomalies over the Northern Oceans: Driving the sea surface temperature. *Journal of Physical Oceanography*, 22, 859-881.

Chan, S. C., and V. Misra, 2010: A diagnosis of the 1979-2005 extreme rainfall events in the Southeast US with isentropic moisture tracing. *Mon. Wea. Rev.* , 138, 1172–1185.

Changnon, S. A., 1999: Impacts of 1997-98 El Nino-generated weather in the United States. *Bull. Amer. Meteor. Soc.*, 80, 1819-1828.

Chen, F., and J. Dudhia, 2001: Coupling an advanced land-surface/ hydrology model with the Penn State/ NCAR MM5 modeling system. Part I: Model description and implementation. *Mon. Wea. Rev.*, 129, 569-585.

Chen, M., D. Pollard, and E. J. Barron, 2003: Comparison of future climate change over North America simulated by two regional models. *J. Geophys. Res. -Atmos.*, 108, 4348.

Chen, M., P. Xie, J. E. Janowiak, and P. A. Arkin, 2002: Global land precipitation: a 50-yr monthly analysis based on gauge observations. *J. Hydrometeor.*, 3, 249–266.

Chen, P., and M. Newman, 1998: Rossby Wave Propagation and the Rapid Development of Upper-Level Anomalous Anticyclones during the 1988 U.S. Drought. *J. Climate*, 11, 2491-2504.

Chou, C., J. D. Neelin, C.-A. Chen, and J.-Y. Tu, 2009: Evaluating the "rich-get-richer" mechanism in tropical precipitation change under global warming. *J. Climate*, 22, 1982–2005.

Christensen, J. H., and Coauthors, 2007: Regional climate Projection. In: *Climate Change 2007: The Physical Science Basis. Contribution of Working Group I to the Fourth Assessment Report of the Intergovernmental Panel on Climate Change*, [Solomon, S., D. Qin, M. Manning, Z. Chen, M. Marquis, K. B. Averyt, M. Tignor and H. L. Millor (eds)] Cambridge University Press, Cambridge, United Kingdom and New York, NY, USA.

Colbert, A. J., and B. J. Soden, 2012: Climatological variations in North Atlantic tropical cyclone tracks. *J. Climate*, 25, 657-673.

Cook, K. H., E. K. Vizy, Z. S. Launer, and C. M. Patricola, 2008: Springtime intensification of the Great Plains low-level jet and Midwest precipitation in GCM simulations of the twenty-first century. *J. Climate*, 21, 6321-6340.

Curtis, S., 2008: The Atlantic multidecadal oscillation and extreme daily precipitation over the US and Mexico during the hurricane season *Clim. Dyn.*, 30, 343–351.

Dai, A., 2006: Recent climatology, variability, and trends in global surface humidity. *J. Climate*, 19, 3589-3606.

Dairaku, K., and S. Emori, 2006: Dynamic and thermodynamic influences on intensified daily rainfall during the Asian summer monsoon under doubled atmospheric CO_2 conditions *Geophys. Res. Lett.*, 33, L01704.

Daly, C., and Coauthors, 2008: Physiographically-sensitive mapping of temperature and precipitation across the conterminous United States. *Int. J. Climatol.*, 28, 2031-2064.

Davis, R. E., B. P. Hayden, D. A. Gay, W. L. Phillips, and G. V. Jones, 1997: The North Atlantic Subtropical anticyclone. *J. Climate* 10, 728-744.

Dee, D. P., and Coauthors, 2011: The ERA-Interim reanalysis: configuration and performance of the data assimilation system. *Quart. J. R. Meteorol. Soc.*, 137, 553–597.

DeGroot, M. H., and M. J. Schervish, 2011: *Probability and statistics, 839pp.* Addison Wesley Publishing Company Incorporated.

Delworth, T., and S. Manabe, 1989: The influence of soil wetness on near-surface atmospheric variability. *J. Climate*, 2, 1447–1462.

Denis, B., J. Côté, and R. Laprise, 2002: Spectral decomposition of two-dimensional atmospheric fields on limited-area domains using the discrete cosine transform (DCT). *Mon. Wea. Rev.*, 130, 1812–1829.

Diem, J., 2006: Synoptic-scale controls of summer precipitation in the Southeastern United States. *J. Climate*, 19, 613-621.

Douglas, E. M., and A. P. Barros, 2002: Probable maximum precipitation estimation using multifractals: application in the Eastern United States. *J. Hydrometeor.*, 4, 1012-1024.

Drumond, A., R. Nieto, and L. Gimeno, 2011: On the contribution of the Tropical Western Hemisphere Warm Pool source of moisture to the Northen Hemisphere precipitation through a Lagrangian appraoch. *J. Geophys. Res. -Atmos.*, 116, D00Q04.

Dudhia, J., 1989: Numerical study of convection observed during the winter monsoon experiment using a mesoscale two-dimensional model. *J. Atmos. Sci.*, 46, 3077–3107.

Duhamel, P., and M. Vetterli, 1990: Fast Fourier transforms: A tutorial review and a state of the art. *Signal Processing*, 19, 259–299.

Eichler, T., and W. Higgins, 2006: Climatology and ENSO-related variability of North American extratropical cyclone activity. *J. Climate*, 19, 2076–2093.

Ek, M. B., and A. A. M. Holtslag, 2004: Influence of soil moisture on boundary layer cloud development. *J. Hydrometeor.*, 5, 86-99.

Emanuel, K. A., 1994: *Atmospheric Convection. 592 pp.* Oxford University Press.

Feser, F., B. Rockel, H. V. Storch, J. R. G. Winterfeldt, and M. Zahn, 2011: Regional climate models add value to global model data. *Bull. Amer. Meteor. Soc.*, 92, 1181-1192.

Flato, G., and Coauthors, 2013: Evaluation of Climate Models. *Climate Change 2013: The Physical Science Basis. Contribution of Working Group I to the Fifth Assessment Report of the Intergovernmental Panel on Climate Change*, T. F. Stocker, and Coauthors, Eds., Cambridge University Press,.

Foley, A. M., 2010: Uncertainty in regional climate modeling: A review. *Prog. Phys. Geogr.*, 34, 647-670.

Franzke, C., K. Fraedrich, and F. Lunkeit, 2001: Teleconnections and low-frequency variability in idealized experiments with two storm tracks. *Quart. J. Roy. Meteor. Soc.*, 127, 1321-1339.

Gamble, D. W., D. B. Parnell, and S. Curtis, 2008: Spatial variability of the Caribbean mid-summer drought and relation to north Atlantic high circulation. *Int. J. Climatol.*, 28, 343–350.

Gentine, P., A. A. M. Holtslag, F. D'Andrea, and M. Ek, 2013: Surface and atmospheric controls on the onset of moist convection over land *J. Hydrometeor.*, 14, 1443–1462.

Gill, A. E., 1980: Some simple solutions for the heat induced tropical circulation. *Quart. J. Roy. Meteor. Soc.*, 106, 447-462.

Gimeno, L., A. Drumond, R. Nieto, R. M. Trigo, and A. Stohl, 2010: On the origin of continental precipitation. *Geophys. Res. Lett.*, 37, L13804.

Giorgi, F., and L. O. Mearns, 1999: Introduction to special section: Regional climate modeling revisited. *J. Geophys. Res. Atmos.*, 104, 6335–6352.

Gleckler, P. J., K. E. Taylor, and C. Doutriaux, 2008: Performance metrics for climate models. *J. Geophys. Res. -Atmos.*, 113, D06104.

Grell, G. A., and D. Dévényi, 2002: A generalized approach to parameterizing convection combining ensemble and data assimilation techniques. . *Geophys. Res. Lett.*, 29, doi:10.1029/2002GL015311.

Groisman, P. Y., R. W. Knight, T. R. Karl, D. R. Easterling, B. Sun, and J. H. Lawrimore, 2004: Contemporary changes of the hydrological cycle over the contiguous United States: trends derived from in situ observations. *J. Hydrometeor.*, 5, 64-85.

Hayhoe, K., and Coauthors, 2007: Past and future changes in climate and hydrological indicators in the US Northeast. *Clim. Dyn.*, 28, 381-407.

Held, I. M., and B. J. Soden, 2006: Robust responses of the hydrological cycle to global warming. *J. Climate*, 19, 5686-5699.

Henderson, K. G., and P. J. Robinson, 1994: Relationships between the pacific/north american teleconnection patterns and precipitation events in the south-eastern USA. *Int. J. Climatol.*, 14, 307-323.

Henderson, K. G., and A. J. Vega, 1996: Regional precipitation variability in the southeastern United States. *Phys. Geogr.*, 17, 93-112.

Hibbard, K. A., G. A. Meehl, P. Cox, and P. Friedlingstein, 2007: A strategy for climate change stabilization experiments. *Eos, Trans. Amer. Geophys. Union*, 88, 217.

Higgins, R. W., W. Shi, E. Yarosh, and R. Joyce, 2000: Improved United States precipitation quality control system and analysis. NCEP/Climate Prediction Center ATLAS No. 7, 40 pp., Camp Springs, MD 20746, USA.

Higgins, R. W., V. B. S. Silva, W. Shi, and J. Larson, 2007: Relationships between climate variability and fluctuations in daily precipitation over the United States. *J. Climate* 20, 3561–3579.

Hoetlling, H., 1931: The generalization of Student's ratio *Annals of Mathematical Statistics*, 2, 360-378.

Hoff, P. D., 2009: *A first course in Bayesian statistical methods.* Springer.

Honda, M., Y. Kushnir, H. Nakamura, S. Yamane, and S. E. Zebiak, 2005: Formation, Mechanisms, and Predictability of the Aleutian–Icelandic Low Seesaw in Ensemble AGCM Simulations. *J. Climate*, 25, 1423-1434.

Hoskins, B. J., 1991: Towards a PV-theta view of the general circulation. *Tellus. Ser. AB*, 43, 27-35.

Hoskins, B. J., and D. J. Karoly, 1981: The steady linear response of a spherical atmosphere to thermal and orographic forcing. *J. Atmos. Sci.*, 38, 1179-1196.

Hu, Q., and S. Feng, 2012: AMO- and ENSO-driven summertime circulation and precipitation variations in North America. *J. Climate*, 25, 6477-6495.

Hu, Q., S. Feng, and R. J. Oglesby, 2011: Variations in North American summer precipitation driven by the Atlantic multidecadal oscillation. *J. Climate*, In press.

Hu, Z.-Z., and B. Huang, 2006: Air–sea coupling in the North Atlantic during summer. *Clim. Dyn.*, 26, 441-457.

Huffman, G. J., and Coauthors, 1997: The Global Precipitation Climatology Project (GPCP) Combined Precipitation Dataset. *Bull. Amer. Meteor. Soc.*, 78, 5-20.

Huntington, T. G., 2006: Evidence for intensification of the global water cycle: review and synthesis. *Journal of Hydrology*, 319, 83-95.

Janjic, Z. I., 1994: The step-mountain eta coordinate model: further developments of the con- vection, viscous sublayer and turbulence closure schemes *Mon. Wea. Rev.*, 122, 927–945.

——, 2000: Comments on "Development and Evaluation of a Convection Scheme for Use in Climate Models". *J. Atmos. Sci.*, 57, 3686.

Jankov, I., W. A. Gallus, M. Segal, B. Shaw, and S. E. Koch, 2005: The impact of different WRF Model physical parameterizations and their interactions on warm season MCS rainfall. *Wea. Forecasting*, 20, 1048–1060.

Ji, X., J. D. Neelin, S.-K. Lee, and C. R. Mechoso, 2014: Interhemispheric teleconnections from tropical heat sources in intermediate and simple models. *J. Climate*, 27, 684–697.

Kain, J. S., 2004: The Kain–Fritsch convective parameterization: An update. *J. Appl. Meteor.*, 43, 170-181.

Kalkstein, L. S., G. Tan, and J. A. Skindlov, 1987: An evaluation of three clustering procedures for use in synoptic climatological classification. *J. Climate Appl. Meteor.*, 26, 717-730.

Kalnay, E., and Coauthors, 1996: The NCEP-NCAR 40-year reanalysis project. *Bull. Amer. Meteor. Soc.*, 77, 437-471.

Kanamitsu, M., W. Ebisuzaki, J. Woollen, S.-K. Yang, J. J. Hnilo, M. Fiorino, and G. L. Potter, 2002: NCEP-DOE AMIP-II reanalysis (R-2). *Bull. Amer. Meteor. Soc.*, 83, 1631-1643.

Katz, R. W., and B. G. Brown, 1992: Extreme events in a changing climate: variability is more important than averages. *Clim. Change*, 21, 289-302.

Katz, R. W., M. B. Parlange, and C. Tebaldi, 2003: Stochastic modeling of the effects of large-scale circulation on daily weather in the southeastern US. *Clim. Change*, 60, 189-216.

Kawase, H., M. Abe, Y. Yamada, T. Takemura, T. Yokohata, and T. Nozawa, 2010: Physical mechanism of long-term drying trend over tropical North Africa. *Geophys. Res. Lett.*, 37, L09706.

Keim, B. D., R. A. Muller, and G. W. Stone, 2007: Spatiotemporal patterns and return periods of tropical storm and hurricane strikes from Texas to Maine. *J. Climate*, 20, 3498-3509.

Keim, B. D., R. Fontenot, C. Tebaldi, and D. Shankmanc, 2011: Hydroclimatology of the U.S. Gulf Coast under global climate change scenarios. *Physical Geography*, 32, 561-582.

Kelly, P., and B. Mapes, 2011: Zonal mean wind, the Indian monsoon, and July drying in the western Atlantic subtropics. *J. Geophys. Res. -Atmos.*, 116, D00Q07.

Klotzbach, P. J., 2011: El Niño–Southern Oscillation's impact on Atlantic basin hurricanes and U.S. landfalls. *J. Climate*, 24, 1252–1263.

——, 2012: El Niño-Southern Oscillation, the Madden-Julian Oscillation and Atlantic basin tropical cyclone rapid intensification. *J. Geophys. Res. Atmos.*, 117, D14104.

Knight, D. B., and R. E. Davis, 2007: Climatology of tropical cyclone rainfall in the southeastern United States. *Phys. Geogr.*, 28, 126-147.

Knight, D. B., and R. E. Davis, 2009: Contribution of tropical cyclones to extreme rainfall events in the southeastern United States. *J. Geophys. Res. -Atmos.*, 114, D23102.

Konrad, C. E., 1997: Synoptic-scale features associated with warm season heavy rainfall over the interior southeastern United States. *Wea. Forecasting*, 12, 557-571.

Konrad, C. E., and L. B. Perry, 2010: Relationships between tropical cyclones and heavy rainfall in the Carolina region of the USA. *Int. J. Climatol.*, 30, 522-534.

Kosaka, Y., and H. Nakamura, 2010: Mechanisms of meridional teleconnection observed between a summer monsoon system and a subtropical anticyclone. Part II: A global survey. *J. Climate*, 23, 5109-5125.

Kunkel, K. E., D. R. Easterling, D. A. R. Kristovich, B. Gleason, L. Stoecker, and R. Smith, 2010: Recent increases in U.S. heavy precipitation associated with tropical cyclones. *Geophys. Res. Lett.*, 37, L24706.

Kunkel, K. E., D. R. Easterling, D. A. R. Kristovich, B. Gleason, L. Stoecker, and R. Smith, 2012: Meteorological causes of the secular variations in observed extreme precipitation events for the conterminous United States. *J. Hydrometeor.*, 13, 1131-1141.

Kunkel, K. E., K. Andsager, X.-Z. Liang, R. W. Arritt, E. S. Takle, W. J. Gutowski, and Z. Pan, 2002: Observations and regional climate model simulations of heavy precipitation events and seasonal anomalies: A comparison. *J. Hydrometeor.*, 3, 322-334.

Kushnir, Y., R. Seager, M. Ting, N. Naik, and J. Nakamura, 2010: Mechanisms of Tropical Atlantic SST Influence on North American Precipitation Variability. *J. Climate*, 23, 5610-5628.

Kushnir, Y., W. A. Robinson, I. Bladé, N. M. J. Hall, S. Peng, and R. Sutton, 2002: Atmospheric GCM response to extratropical SST anomalies: Synthesis and evaluation. *J. Climate*, 15, 2233–2256.

Leathers, D. J., B. Yarnal, and M. A. Palecki, 1991: The Pacific/North American teleconnection pattern and united states climate. Part I: Regional temperature and precipitation associations. *J. Climate*, 4, 517–528.

Leung, L. R., L. O. Mearns, F. Giorgi, and R. L. Wilby, 2003: Regional climate research: Needs and opportunities. *Bull. Amer. Meteor. Soc.*, 84, 89-95.

Li, L., and W. Li, 2013: Southeastern United States summer rainfall framework and its implication for seasonal prediction. *Environ. Res. Lett.* , 8, 044017

Li, L., W. Li, and Y. Kushnir, 2012a: Variation of North Atlantic Subtropical High western ridge and its implication to the Southeastern US summer precipitation. *Clim. Dyn.*, 39, 1401-1412.

Li, L., W. Li, and Y. Deng, 2013a: Summer rainfall variability over the Southeastern United States in the 21st century as assessed by the CMIP5 Models. *J. Geophys. Res. Atmos.*, 118, 340-354.

Li, L., W. Li, and A. P. Barros, 2013b: Atmospheric moisture budget and its regualtion of the summer precipitation variability over the Southeastern United States. *Clim. Dyn.*, 41, 613-631.

Li, L., W. Li, and J. Jin, 2014: Improvements in WRF simulation skills of Southeastern United States summer rainfall: Physical parameterization and horizontal resolution. *Clim. Dyn.*, In Press, DOI: 10.1007/s00382-00013-02031-00382.

Li, W., and R. Fu, 2004: Transition of the large-scale atmospheric and land surface conditions from dry to wet season over Amazonia as diagnosed by the ECMWF Reanalysis. *J. Climate*, 17, 2637–2651.

Li, W., R. Fu, R. I. N. Juarez, and K. Fernandes, 2008: Observed change of the standardized precipitation index, its potential cause and implications to future climate in the Amazon region. *Philosophical Transaction of the Royal Society: Climate Change and the Fate of the Amazon*, 363, 1767-1772.

Li, W., L. Li, M. Ting, and Y. Liu, 2012b: Intensification of Northern Hemisphere subtropical highs in a warming climate. *Nature Geoscience*, 5, 830–834.

Li, W., L. Li, R. Fu, Y. Deng, and H. Wang, 2011: Changes to the North Atlantic Subtropical High and its role in the intensification of summer rainfall variability in the Southeastern United States. *J. Climate* 24, 1499-1506.

Liang, X.-Z., K. E. Kunkel, and A. N. Samel, 2001: Development of a regional climate model for U.S. Midwest applications. Part I: Sensitivity to buffer zone treatment. *J. Climate*, 14, 4363–4378.

Liang, X. Z., J. Pan, J. Zhu, K. E. Kunkel, J. X. L. Wang, and A. Dai, 2006: Regional climate model downscaling of the U.S. summer climate and future change. *J. Geophys. Res. -Atmos.*, 111, D10108.

Lin, Y.-L., S. Chiao, T.-A. Wang, M. L. Kaplan, and R. P. Weglarz, 2001: Some Common Ingredients for Heavy Orographic Rainfall. *Wea. Forecasting*, 16, 633–660.

Lin, Y. L., R. D. Farley, and H. D. Orville, 1983: Bulk parameterization of the snow field in a cloud model. *J. Climate Appl. Meteor. Climatol.*, 22, 1065-1092.

Liu, Y., and G. Wu, 2004: Progress in the study on the formation of the summertime subtropical anticyclone. *Adv. Atmo. Sci.*, 21, 322-342.

Liu, Y., G. Wu, and R. Ren, 2004: Relationship between the subtropical anticyclone and diabatic heating. *J. Climate*, 17, 682-698.

Liu, Y., L. Guo, G. Wu, and Z. Wang, 2010: Sensitivity of ITCZ configuration to cumulus convective parameterizations on an aqua-planet. *Clim. Dyn.*, 34, 223-240.

Livezey, R. E., and W. Y. Chen, 1983: Statistical field significance and its determination by Monte Carlo techniques. *Mon. Wea. Rev.*, 111, 46-59.

Lo, J. C. F., Z. L. Yang, and R. A. P. Sr., 2008: Assessment of three dynamical climate downscaling methods using the Weather Research and Forecasting (WRF) model. *J. Geophys. Res. Atmos.*, 113, D09112.

Loveland, T. R., T. L. Sohl, S. V. Stehman, A. L. Gallant, K. L. Sayler, and D. E. Napton, 2002: A strategy for estimating the rates of recent United States land-cover changes. *Photogramm. Eng. Remote Sens.*, 68, 1091–1099.

Mantua, N. J., and S. R. Hare, 2002: The Pacific decadal oscillation. *J. Oceanog.*, 58, 35-44.

Mantua, N. J., S. R. Hare, Y. Zhang, J. M. Wallace, and R. C. Francis, 1997: A Pacific interdecadal climate oscillation with impact on salmon production. *Bull. Amer. Meteor. Soc.*, 78, 1069—1079.

Manuel, J., 2008: Drought in the southeast: lessons for water management. *Environ. Health Perspect.*, 116, A168-A171.

Marshall, C. H., R. A. Pielke, L. T. Steyaert, and D. A. Willard, 2004: The Impact of Anthropogenic Land-Cover Change on the Florida Peninsula Sea Breezes and Warm Season Sensible Weather. . *Mon. Wea. Rev.*, 132, 28–52.

Martinez, C. J., G. A. Baigorria, and J. W. Jones, 2009: Use of climate indices to predict corn yields in southeast USA. *Int. J. Climatol*, 29, 1680-1691.

Maxwell, J. T., J. T. Ortegren, P. A. Knapp, and P. T. Soule, 2013: Tropical cyclones and drought amelioration in the Gulf and Southeastern coastal United States. *J. Climate*, 26, 8440-8452.

McCabe, G. J., M. A. Palecki, and J. L. Betancourt, 2004: Pacific and Atlantic Ocean influence on Multidecadal drought frequency in the United States. *Proc. Natl. Acad. Sci.* , 101, 4136—4141.

Mearns, L. O., F. Giorgi, L. McDaniel, and C. Shields, 2003: Climate scenarios for the southeastern U.S. based on GCM and regional model simulations. *Clim. Change*, 60, 7-35.

Mearns, L. O., W. J. Gutowski, R. Jones, L.-Y. Leung, S. McGinnis, A. M. B. Nunes, and Y. Qian, 2009: A regional climate change assessment program for North America. *Eos, Trans. Amer. Geophys. Union*, 90, 311-312.

Mearns, L. O., and Coauthors, 2012: The North American Regional Climate Change Assessment Program: Overview of Phase I Results. *Bull. Amer. Meteor. Soc.*, 93, 1337–1362.

Meehl, G. A., and K. A. Hibbard, 2007: A strategy for climate change stabilization experiments with AOGCMs and ESMs, WCRP Informal Report No. 3/2007, ICPO Publication No. 112, IGBP Report No. 57, World Climate Research Programme: Geneva, 35 pp.

Mesinger, F., and Coauthors, 2006: North American Regional Reanalysis. *Bull. Amer. Meteor. Soc*, 87, 343-360.

Miller, N. L., J. Jin, and C.-F. Tsang, 2005: Local climate sensitivity of the Three Gorges Dam. *Geophys. Res. Lett.*, 32, L16704.

Miller, S. T. K., B. D. Keim, R. W. Talbot, and H. Mao, 2003: Sea breeze: Structure, forecasting, and impacts *Rev. Geophys.*, 41, 1011.

Minobe, S., M. Miyashita, A. Kuwano-Yoshida, H. Tokinaga, and S.-P. Xie, 2010: Atmospheric response to the Gulf Stream: seasonal variations. *J. Climate*, 23, 3699-3719.

Misra, V., L. Moeller, L. Stefanova, S. Chan, J. J. O'Brien, T. J. S. III, and N. Plant, 2011: The influence of the Atlantic Warm Pool on the Florida panhandle sea breeze. *J. Geophys. Res. Atmos.*, 116, D00Q06.

Mlawer, E. J., S. J. Taubman, P. D. Brown, M. J. Iacono, and S. A. Clough, 1997: Radiative transfer for inhomogeneous atmosphere: RRTM, a validated correlated-k model for the long- wave. . *J. Geophys. Res. Atmos.*, 102, 16663–16682.

Mo, K. C., and J. E. Schemm, 2008: Relationship between ENSO and drought over the Southeastern United States. *Geophys. Res. Lett.*, 35, L15701.

Mo, K. C., J.-K. E. Schemm, and S.-H. Yoo, 2009: Influence of ENSO and the Atlantic multidecadal oscillation on drought over the United States. *J. Climate*, 22, 5962-5982.

Moncrieff, M., and M. Miller, 1976: The dynamics and simulation of tropical cumulonimbus and squall lines. *Quart. J. R. Meteorol. Soc.*, 102, 373–394.

Morrison, H., G. Thompson, and V. Tatarskii, 2009: Impact of cloud microphysics on the development of trailing stratiform precipitation in a simulated squall line: Comparison of one- and two-moment schemes. *Mon. Wea. Rev.*, 137, 991–100.

Moss, R. H., and Coauthors, 2010: The next generation of scenarios for climate change research and assessment. *Nature* 463, 747-756.

Mueller, B., and Coauthors, 2011: Evaluation of global observations-based evapotranspiration datasets and IPCC AR4 simulations. *Geophys. Res. Lett.*, 38, L06402.

Nakanishi, M., and H. Niino, 2006: An improved Mellor-Yamada level-3 model: Its numerical stability and application to a regional prediction of advection fog. *Bound. Layer Meteor.*, 119, 397-407.

Nigam, S., and S. C. Chan, 2009: On the summertime strengthening of the Northern hemisphere Pacific sea level pressure anticyclone. *J. Climate* 22, 1174-1192.

Ninomiya, K., and C. Kobayashi, 1999: Precipitation and moisture balance of the Asian summer monsoon in 1991 Part II: moisture transport and moisture balance. *J. Meteor. Soc. Japan*, 77, 77-99.

Noh, Y., W. G. Cheon, S. Y. Hong, and S. Raasch, 2003: Improvement of the K-profile model for the planetary boundary layer based on large eddy simulation data. *Bound. Layer Meteor.*, 107, 421-427.

O'Gorman, P. A., and T. Schneiderb, 2009: The physical basis for increases in precipitation extremes in simulations of 21st-century climate change. *Proc. Natl. Acad. Sci.*, 106, 14773–14777.

Onogi, K., and Coauthors, 2007: The JRA-25 Reanalysis. *J. Meteor. Soc. Japan*, 85, 369-432.

Ortegren, J. T., P. A. Knapp, J. T. Maxwell, W. P. Tyminski, and P. T. Soulé, 2011: Ocean–atmosphere influences on low-frequency warm-season drought variability in the Gulf Coast and Southeastern United States. . *J. Appl. Meteor. Climatol.*, 50, 1177-1186.

Otte, T. L., C. G. Nolte, M. J. Otte, and J. H. Bowden, 2012: Does nudging squelch the extremes in regional climate modeling? . *J. Climate*, 25, 7046–7066.

Patricola, C. M., and K. H. Cook, 2013: Mid-twenty-first century climate change in the Central United States. Part II: Climate change processes. *Clim. Dyn.*, 40, 569-583.

Peters, A., L. Ji, and E. Walter-Shea, 2003: Southeastern US vegetation response to ENSO events (1989–1999). *Clim. Change*, 60, 175-188.

Pielke, R. A. S., 2002: *Mesoscale meteorological modeling, 2nd ed., 676pp.* Elsevier.

Plumb, R. A., 1985: On the three-dimensional propagation of stationary waves. *J. Atmos. Sci.*, 42, 217-229.

Quadrelli, R., and J. M. Wallace, 2002: Dependence of the structure of the Northern Hemisphere annular mode on the polarity of ENSO. *Geophys. Res. Lett.* , 29, 2132.

Rauscher, S. A., E. Coppola, C. Piani, and F. Giorgi, 2010: Resolution effects on regional climate model simulations of seasonal precipitation over Europe. . *Clim. Dyn.*, 35, 685-711.

Rhee, J., J. Im, G. J. Carbone, and J. R. Jensen, 2008: Delineation of climate regions using in-situ and remotely-sensed data for the Carolinas. *Remote Sensing of Environment*, 112, 3099-3111.

Riha, S. J., D. S. Wilks, and P. Simoens, 1996: Impact of temperature and precipitation variability on crop model predictions. *Clim. Change*, 32, 293-311.

Roe, G. H., 2005: Orographic precipitation. *Annu. Rev. Earth Planet. Sci*, 33, 645-671.

Ropelewski, C. F., and M. S. Halpert, 1987: Global and regional scale precipitation patterns associated with the El Niño/Southern oscillation. *Mon. Wea. Rev.*, 115, 1606-1626.

Ross, R. J., and W. P. Elloitt, 2001: Radiosonde-based northern hemisphere tropospheric water vapor trends. *J. Climate*, 14, 1602-1611.

Ruane, A. C., 2010: NARR'S atmospheric water cycle components. Part II: summertime mean and diurnal interactions. *J. Hydrometeor.*, 11, 1220-1233.

Rudolf, B., A. Becker, U. Schneider, A. Meyer-Christoffer, and M. Ziese, 2010: GPCC status report december 2010 (On the most recent gridded global data set issued in fall 2010 by the Global Precipitation Climatology Centre (GPCC)).

Rummukainen, M., 2010: State-of-the-art with regional climate models. *WIREs Clim. Change*, 1, 82–96.

Saha, S., and Coauthors, 2006: The NCEP Climate Forecast System *J. Climate* 19, 3483-3517.

Seager, R., A. Tzanova, and J. Nakamura, 2009: Drought in the Southeastern United States: causes, variability over the last millennium and the potential for future hydroclimate change. *J. Climate*, 22, 5021-5045.

Seager, R., N. Naik, and G. A. Vecchi, 2010: Thermodynamic and dynamic mechanisms for large-scale changes in the hydrological cycle in response to global warming. *J. Climate*, 23, 4651-4668.

Seager, R., N. Naik, and L. Vogel, 2012: Does Global Warming Cause Intensified Interannual Hydroclimate Variability? *J. Climate*, 25.

Seager, R., R. Murtugudde, N. Naik, A. Clement, N. Gordon, and J. Miller, 2003: Air-sea interaction and the seasonal cycle of the subtropical anticyclones. *J. Climate*, 16, 1948-1966.

Seager, R., and Coauthors, 2007: Model projections of an imminent transition to a more arid climate in Southwestern North America. *Science*, 316, 1181-1184.

Seth, A., and F. Giorgi, 1998: The effects of domain choice on summer precipitation simulation and sensitivity in a regional climate model. *J. Climate*, 11, 2698–2712.

Shepherd, J. M., A. Grundstein, and T. L. Mote, 2007: Quantifying the contribution of tropical cyclones to extreme rainfall along the coastal southeastern United States. *Geophys. Res. Lett.*, 34, L23810.

Sherwood, S. C., R. Roca, T. M. Weckwerth, and N. G. Andronova, 2010: Tropospheric water vapor, convection and climate. *Rev. Geophys.*, 48, RG2001.

Simpson, J. E., 1994: *Sea Breeze and Local Wind.* Cambridge Univ. Press, 234 pp.

Skamarock, W. C., and Coauthors, 2008: A description of the advanced research WRF version 3, NCAR Tech. Note NCAR/TN-475+STR. , 125 pp.

Skific, N., J. A. Francis, and J. J. Cassano, 2009: Attribution of seasonal and regional changes in Arctic moisture convergence. *J. Climate*, 22, 5115–5134.

Sobolowski, S., and T. Pavelsky, 2012: Evaluation of present and future North American Regional Climate Change Assessment Program (NARCCAP) regional climate simulations over the southeast United States. *J. Geophys. Res. Atmos.*, 117, D01101.

Soulé, P. T., 1998: Some Spatial Aspects of Southeastern United States Climatology. *Journal of Geography*, 97, 142-150.

Stahle, W. D., and M. K. Cleaveland, 1992: Reconstruction and analysis of spring rainfall over the Southeastern U.S for the past 1000 years *Bull. Amer. Meteor. Soc.*, 73, 1947–1961.

Stauffer, D. R., and N. L. Seaman, 1990: Use of Four-Dimensional Data Assimilation in a limited-area mesoscale model. Part I: Experiments with synoptic-scale data. *Mon. Wea. Rev.*, 118, 1250–1277.

Stevens, B., 2005: Atmospheric moist convection. *Annu. Rev. Earth Planet. Sci*, 33, 605-643.

Stocker, T. F., and C. C. Raibe, 2005: Water cycle shifts gear. *Nature*, 434, 830-833.

Stooksbury, D. E., and P. J. Michaels, 1991: Cluster analysis of southeastern U.S. climate stations. *Theor. Appl. Climatol.*, 44, 143-150.

Stoy, P. C., and Coauthors, 2006: Separating the effects of climate and vegetation on evapotranspiration along a successional chronosequence in the southeastern U.S. *Global Change Biology*, 12, 2115–2135.

Sun, X., and A. P. Barros, 2012: The Impact of Forcing Datasets on the High-Resolution Simulation of Tropical Storm Ivan (2004) in the Southern Appalachians. *Mon. Wea. Rev.*, 140, 3300–3326.

Taylor, K. E., 2001: Summarizing multiple aspects of model performance in a single diagram. *J. Geophys. Res. Atmos.*, 106, 7183-7192.

Taylor, K. E., R. J. Stouffer, and G. A. Meehl, 2012: An overview of CMIP5 and the experiment design. *Bull. Amer. Meteor. Soc.*, 93, 485-498.

Thibeault, J. M., and A. Seth, 2014: A framework for evaluating model credibility for warm-season precipitation in Northeastern North America: A case study of CMIP5 simulations and projections. *J. Climate*, 27, 493-510.

Thompson, G., P. R. Field, R. M. Rasmussen, and W. D. Hall, 2008: Explicit forecasts of winter precipitation using an improved bulk microphysics scheme. Part II: Implementation of a new snow parameterization. *Mon. Wea. Rev.*, 136, 5095–5115.

Ting, M., and H. Wang, 2006: The role of the North American topography on the maintenance of the Great Plains summer low-level jet. *J. Atmos. Sci.*, 63, 1056-1068.

Tompkins, A., 2001: Organization of tropical convection in low vertical wind shears: The role of water vapor. *J. Atmos. Sci.*, 58, 529–545.

Torrence, C., and G. P. Compo, 1998: A practical guide to wavelet analysis. *Bull. Amer. Meteor. Soc.*, 79, 61-78.

Trenberth, K. E., 2011: Changes in precipitation with climate change. *Clim. Res.*, 47, 123-138.

Trenberth, K. E., and C. J. Guillemot, 1995: Evaluation of the global atmospheric moisture budget as seen from analyses. *J. Climate*, 8, 2255-2272.

Uppala, S. M., and Coauthors, 2005: The ERA-40 re-analysis. *Quart. J. Roy. Meteor. Soc.*, 131, 2961-3012.

Walker, M. D., and N. S. Diffenbaugh, 2009: Evaluation of high-resolution simulations of daily-scale temperature and precipitation over the United States. *Clim. Dyn.*, 33, 1131-1147.

Wallace, J. M., and D. S. Gutzler, 1981: Teleconnections in the geopotential height field during the Northern Hemisphere winter. *Mon. Wea. Rev.*, 109, 784-812.

Wang, C., and S.-K. Lee, 2007: Atlantic warm pool, Caribbean low-level jet, and their potential impact on Atlantic hurricanes *Geophys. Res. Lett.*, 34, L02703.

Wang, C., S.-K. Lee, and D. B. Enfield, 2008: Climate response to anomalously large and small Atlantic warm pools during the summer. *J. Climate*, 21, 2437–2450.

Wang, F., Z. Liu, and M. Notaro, 2013: Extracting the dominant SST modes impacting North America's observed climate. *J. Climate*, 26, 5434–5452.

Wang, H., R. Fu, A. Kumar, and W. Li, 2010: Intensification of summer rainfall variability in the Southeastern United States during recent decades. *J. Hydrometeor.* , 11, 1007-1018.

Weisman, M. L., W. C. Skamarock, and J. B. Klemp, 1997: The resolution dependence of explicitly modeled convective systems. *Mon. Wea. Rev.*, 125, 527-548.

Wilks, D. S., 1995: *Statistical methods in the atmospheric sciences.* Academic Press.

Wisse, J. S. P., and J. Vilà-Guerau de Arellano, 2004: Analysis of the role of the planetary boundary layer schemes during a severe convective storm. *Ann. Geophys*, 22, 1861-1874.

Wu, G., and Y. Liu, 2000: Thermal Adaptation, overshooting, dispersion, and subtropical anticyclone Part I: thermal adaptation and overshooting. *Chinese Journal of Atmospheric Sciences (In Chinese)*, 24, 433-446.

——, 2003: Summertime quadruplet heating pattern in the subtropics and the associated atmospheric circulation. *Geophys. Res. Lett.*, 30, 1201.

Wu, G., Y. Liu, and P. Liu, 1999: The effect of spatially nonuniform heating on the formation and variation of subtropical high I. scale analyais. *Acta Meteorologica Sinica*, 57, 257-263.

Wu, G., Y. Liu, X. Zhu, W. Li, R. Ren, A. Duan, and X. Liang, 2009: Multi-scale forcing and the formation of subtropical desert and monsoon. *Annales Geophysicae*, 27, 3631-3644.

Wu, W., R. E. Dickinson, H. Wang, Y. Liu, and M. Shaikh, 2007: Covariabilities of spring soil moisture and summertime United States precipitation in a climate simulation. *Int. J. Climatol.*, 27, 429–438.

Wuebbles, D., and Coauthors, 2013: CMIP5 climate model analyses: Climate extremes in the United States. *Bull. Amer. Meteor. Soc.*, In Press.

Xue, Y., R. Vasic, Z. Janjic, F. Mesinger, and K. E. Mitchell, 2007: Assessment of dynamic downscaling of the Continental U.S. regional climate using the Eta/SSiB regional climate model. *J. Climate*, 20, 4172–4193.

Xue, Y., R. Vasic, Z. Janjic, Y. M. Liu, and P. C. Chu, 2012: The impact of spring subsurface soil temperature anomaly in the western U.S. on North American summer precipitation: A case study using regional climate model downscaling *J. Geophys. Res. Atmos.*, 117, D11103.

Yang, B., Y. Qian, G. Lin, R. Leung, and Y. Zhang, 2012: Some issues in uncertainty quantification and parameter tuning: a case study of convective parameterization scheme in the WRF regional climate model. *Atmos. Chem. Phys.*, 12, 2409-2427.

Yang, F., A. Kumar, M. E. Schlesinger, and W. Wang, 2003: Intensity of hydrological cycles in warming climate. *J. Climate*, 16, 2419-2423.

Zhang, G. J., and N. A. McFarlane, 1995: Sensitivity of climate simulations to the parameterization of cumulus convection in Canadian Climate Center general circulation model. *Atmosphere-Ocean*, 33, 407-446.

Zhang, Y., J. M. Wallace, and D. S. Battisti, 1997: 1997: ENSO-like interdecadal variability: 1900-93. *J. Climate*, 10, 1004-1020.

Biography

Laifang Li was born in Wenzhou, China on October 27, 1984. She graduated from Wenzhou middle school in 2002. In 2006, she graduated with a Bachelor of Science in Physical Oceanography from Ocean University of China. Laifang then entered graduates school at Institute of Atmospheric Physics, Chinese Academy of Sciences, where she earned a Master Degree in Geophysical Fluid Dynamics. She started at Duke University in 2009 and she earned this PhD in Earth and Ocean Sciences in 2014.

During her PhD study, Laifang has published and coauthored 15 research papers. Besides the studies presented in this dissertation, she applied Bayesian statistics to study summer precipitation over the Southeastern United States. The rainfall framework designed by her and her advisor (Li and Li 2013) could improve regional climate predictions, which was highlighted Environmental Research Letters, Science Daily, and National Science Foundation.